

Reconstruction and Selection of Neutrino Interactions in MicroBooNE using Deep Convolutional Neural Networks

MICROBOONE-NOTE-1123-PUB

The MicroBooNE Collaboration*

Fermi National Accelerator Laboratory, Batavia, Illinois

Abstract

In this document, we describe a new reconstruction workflow developed for the MicroBooNE experiment. It features the use of Deep Convolutional Neural Networks trained to recognize key structures within the data sufficient for the 3D reconstruction of neutrino interactions within the detector. As a test of the reconstruction utility, the products of the reconstruction workflow are used to select inclusive charged-current (CC) ν_e and ν_μ interactions in both simulated and real MicroBooNE data. In simulation, our ν_e and ν_μ selections achieve an efficiency of 57% and 68%, respectively, with a purity of 91% and 96%, respectively. We find that these selections are competitive with the inclusive selections used for the most recent MicroBooNE LEE searches. In particular, the CC- ν_e inclusive selection efficiency improves by over 20% while also improving sample purity. As a first step in quantifying potential bias, the data and Monte Carlo expectations are compared for both selections using the MicroBooNE open data. Within statistical and systematic uncertainties, both the electron and muon CC-inclusive event samples agree. A comparison of the real data events chosen by our work and another reconstruction framework shows that the two analyses each identify a sizeable fraction of events the other does not. This suggests that future analyses integrating the strengths of each could lead to combined gains. This work demonstrates, for the first time on real LArTPC data, state-of-the-art neutrino interaction reconstruction centered around deep learning algorithms.

* MICROBOONE.INFO@fnal.gov

CONTENTS

| | |
|---|----|
| I. Introduction | 4 |
| II. A CNN-based Neutrino Reconstruction for LArTPCs | 5 |
| A. Overview of the Reconstruction | 5 |
| 1. Detector coordinate system and Data set terminology | 9 |
| B. LArMatch: 3D spacepoints and keypoints generation | 10 |
| 1. Proposal of 3-wire intersections, or “triplets” | 13 |
| 2. Feature Generating U-Net | 15 |
| 3. Spacepoint real/ghost classifier | 16 |
| 4. Spacepoint Keypoint score | 17 |
| 5. Weighting the Multi-objective Loss | 19 |
| C. 3D Particle Trajectory Reconstruction | 19 |
| D. Keypoint Generation | 20 |
| E. Particle and Interaction Reconstruction with 3D Spacepoints | 21 |
| 1. Forming track candidates | 22 |
| 2. Forming shower candidates | 24 |
| F. Interaction Candidate Formation | 28 |
| G. Reconstruction Validation | 29 |
| 1. Vertex Validation | 30 |
| 2. Prong Validation | 31 |
| H. Energy Reconstruction | 33 |
| I. LArPID: A Prong Classification CNN | 34 |
| 1. Network Inputs and Image Preprocessing | 37 |
| 2. Network Architecture | 39 |
| 3. Training | 40 |
| 4. Network Performance | 44 |
| 5. Interpreting the Model | 46 |
| III. Demonstration: Selection of inclusive ν_e CC and ν_μ CC interactions in MicroBooNE | 49 |
| A. CC nue inclusive selection cuts | 49 |
| B. CC numu inclusive selection cuts | 58 |

| | |
|---|----|
| C. Systematic uncertainty estimates | 60 |
| 1. Detector Systematic Uncertainties | 61 |
| 2. Flux, Cross Section, and Hadron Re-Interaction Uncertainties | 63 |
| D. Results | 65 |
| E. Results of Data and MC comparison using Open Data Sample | 70 |
| IV. Discussion | 71 |
| V. Conclusions | 76 |
| References | 78 |
| A. Additional distributions for data vs expectation comparisons | 82 |

1 I. INTRODUCTION

2 The liquid argon time projection chamber (LArTPC) is the detector technology of choice
3 for several future and current neutrino experiments. Current experiments include Micro-
4 BoONE [1], the Short Baseline Neutrino Detector [2], and ICARUS [3]. Future experiments
5 notably include the Deep Underground Neutrino Experiment (DUNE) [4] an effort towards
6 which several prototype LArTPCs [5] have been constructed. LArTPCs have now found
7 their way into many experiments due to their combination of resolution and scalability.
8 LArTPCs can track charged particle trajectories with millimeter-scale position resolution
9 for detectors with target volumes into the tens of kilotons.

10 The output of LArTPCs can be characterized as very image-like. The waveforms recorded
11 from planes of sense wires can be naturally arranged to produce images of the ionization
12 patterns left behind by charged particles traversing the detector. Image formats are also
13 relevant for alternative readout designs for LArTPCs, such as those that directly measure
14 the 2D location of ionization in order to naturally capture voxelized 3D trajectories [6]. The
15 format of this spatial data has facilitated the application of newly developed machine learning
16 techniques, in particular from the domain of computer vision, to the task of reconstructing
17 the trajectories and particle interactions captured by LArTPCs. Early applications focused
18 on the classification of either entire images cropped from the data or for individual pixels [7].
19 Structures traditionally important in the reconstruction of interactions, such as the location
20 of neutrino vertices have been searched for. High-level, more abstract quantities such as
21 neutrino interaction flavor [8], the energy of electromagnetic (EM) showers [9], and the
22 neutrino energy [10] have been targets of ML algorithms. While these applications were on
23 2D image data, there has been much progress in developing a full reconstruction chain for
24 3D voxelized data.

25 A fully end-to-end machine learning workflow outputs pixel-wise particle classification,
26 the location of key points on particle trajectories, particle clusters, and assembled neutrino
27 interactions into a fully-differentiable workflow [11]. The application of ML to reconstruc-
28 tion has indeed seen rapid progress in the past several years. However, demonstrations of
29 these ML-based tools in the context of analyses of real LArTPC data are only starting to
30 be realized. One such analysis centered around a CNN performing pixel-wise particle-type
31 classification [12, 13] which was used as a central input for the targeted exclusive selection

32 of one-lepton and one-proton final state interactions [14]. This analysis was part of Micro-
33 BooNE’s search for an excess of low-energy electron neutrino interactions [15], conducted to
34 investigate the reported event excess observed by the MiniBooNE experiment [16].

35 This document provides a description of a new “DLGen2” reconstruction and applies it to
36 the selection of inclusive ν_e CC and ν_μ CC interactions in MicroBooNE. Unlike the previous
37 MicroBooNE DL-based analysis, this iteration has aimed for the general reconstruction of
38 all charged particle trajectories coming from neutrino interactions. An overall evaluation
39 and demonstration of the reconstruction is conducted through the execution of the selection
40 on the MicroBooNE open neutrino data set. We find that the efficiencies for this analysis
41 are competitive with the highest-efficiency search previously published by MicroBooNE [17],
42 which utilizes the Wire-Cell reconstruction [17–19]. Furthermore, the inspection of events
43 selected by our reconstruction finds unique events not found by the analysis of Ref. [17].

44 II. A CNN-BASED NEUTRINO RECONSTRUCTION FOR LARTPCS

45 A. Overview of the Reconstruction

46 The reconstruction utilizes convolutional neural networks to enable both 3D energy de-
47 posit reconstruction and perform particle ID on 2D images. The approach taken makes use
48 of the different advantages inherent in the 2D image and 3D point cloud representations.
49 We start the description of the reconstruction chain with a brief overview of the major
50 components of the reconstruction, which are illustrated in figure 1. Later sections then will
51 describe the algorithms used in each component in more detail.

52 The input to the reconstruction is a set of three 2D images, one for each of the wire-
53 planes installed inside the MicroBooNE liquid argon TPC (LArTPC) detector [1]. The
54 waveforms arranged in these images are the output of the first pre-processing stage applied
55 to the raw waveforms. This stage includes the removal of coherent noise seen in sets of
56 neighboring channels [20]. It also reconstructs the original space charge distribution from
57 the measurements on wires by reverting the detector response (e.g., electronic response and
58 field response) and sparsifying the input images. We call this process “Signal Processing.”
59 For more details on the pre-processing stage see Refs. [21, 22].

60 The image set is then provided to two convolutional neural networks (CNN). The first

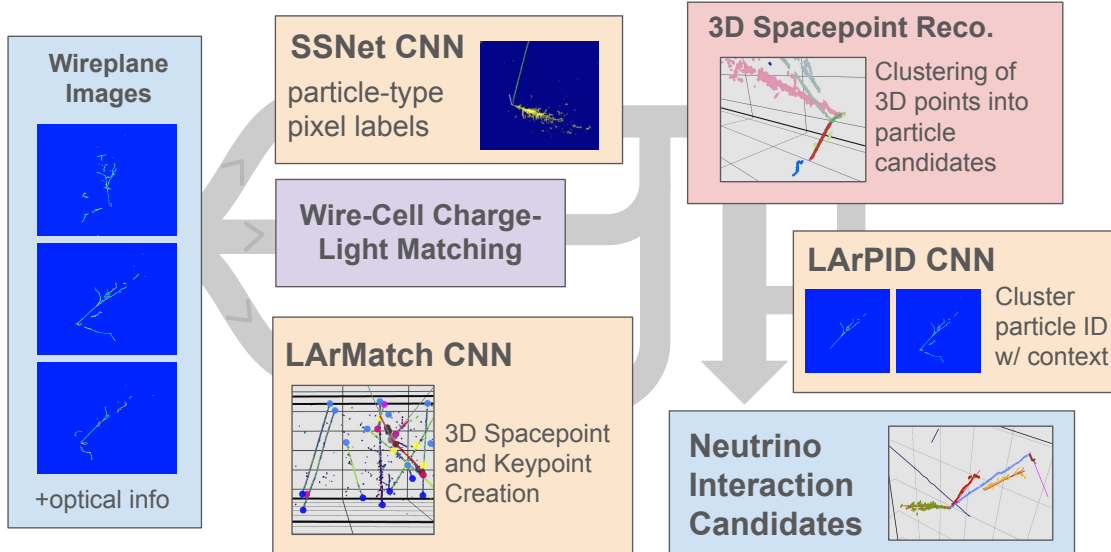


Figure 1: Overview of the reconstruction workflow. The wireplane images and optical information are passed into several components to produce labeled spacepoints reconstructing the location of ionization left behind by charged particles traversing the LArTPC. The labels associated to each spacepoint include particle type and a tag estimating if a given spacepoint is from beam-related or cosmic-ray particles. These points are then clustered into candidate particle trajectories by a set of reconstruction algorithms. A CNN is used to provide a particle-type label for each trajectory. The final output of the workflow are candidate neutrino interactions formed by associating one or more particle clusters to neutrino vertex candidates.

61 CNN acts on each wire plane image separately and is responsible for labeling each pixel
 62 in the image according to two broad particle categories, split by the spatial pattern of
 63 ionization produced. The first type is “track”-like trajectories coming from particles such
 64 as muons, charged pions, and protons. The second type is “shower”-trajectories produced
 65 by electromagnetic cascades initiated by electrons or photons interacting in the detector.
 66 This pixel labeling CNN is referred to as “SSNet” for the semantic-segmentation network
 67 and was used in the first MicroBooNE DL analysis. The details of SSNet can be found in
 68 Ref. [13].

69 A second, new CNN is applied to the set of three 2D images collectively and is referred
 70 to as the “LArMatch” network. The network produces two outputs. The first is a set of
 71 candidate 3D spacepoints which represent the location of energy depositions consistent with
 72 input images. The second product is a set of scores for six different classes of “keypoints.”
 73 Keypoints are useful locations at the start or end of tracks and showers, which, if known, can
 74 greatly simplify the algorithms required to help with clustering and the formation of neutrino

75 interaction candidates. The keypoint classes consist of 1) potential neutrino interaction
76 vertices, 2) the start of track-like particles, 3) the end of track-like particles, 4) start points
77 of EM showers excluding those from delta rays and muon decay, (5) the start points of delta
78 ray showers, and 6) the start point of showers from muon decay.

79 The input images also go through a reconstruction workflow separate from the one de-
80 scribed here. This workflow, referred to as the “Wire-Cell” reconstruction [18], builds space-
81 points, does clustering, and matches clusters of charge to pulses of light seen in the optical
82 detectors [19]. The workflow uses many non-ML approaches and features the application
83 of compressed sensing. What we utilize in our reconstruction workflow is the association of
84 charge clusters to pulses of light either inside or outside the neutrino beam window. This
85 information is used to provide a tag for the spacepoints made by the LArMatch network, as
86 either in-time or out-of-time with the neutrino beam.

87 At this point in the reconstruction, we have a set of spacepoints with various tags deriving
88 from pixel-based labels along with a collection of keypoints. The next step in the workflow is
89 to reconstruct 3D spacepoints, which are then clustered into subclusters covering individual
90 particle trajectories. The purpose of starting with subclusters is to emphasize the purity
91 of the clustering over completeness. Here the purity refers to the largest fraction of points
92 whose ground truth label is associated to the end of the event. A pure cluster would contain
93 spacepoints associated to only one particle. The completeness measures the fraction of
94 possible pixels or spacepoints in the cluster.

95 The 3D clustering algorithm implements the commonly used Density-Based Scan (DB-
96 Scan) algorithm which uses the distances between k-nearest neighbors. What allows for this
97 simple clustering routine is the many tags coming from LArMatch, SSNet, and the Wire-
98 Cell in-time/out-of-time algorithm. These labels are used to partition the spacepoints before
99 clustering, helping to reduce overclustering where spacepoints from two different particle tra-
100 jectories are included into one cluster. For example, the LArMatch track and shower start
101 keypoints are used to temporarily remove nearby spacepoints in order to prevent spacepoints
102 from particles coming out of a common interaction vertex from being grouped together.

103 After the subclustering step, non-ML algorithms are then used to combine the subclusters
104 to form sets of spacepoints intended to represent the ionization produced by a single particle.
105 These algorithms make use of the LArMatch outputs for track endpoints and shower starts
106 to seed the particle-building algorithms.

107 After this clustering stage is complete, the reconstruction has formed candidate particle
108 trajectories. The following stage forms neutrino interaction candidates by associating pri-
109 mary particle trajectories to interaction vertices. Secondary trajectories are also associated
110 to interactions by looking for trajectories that seem to emerge from previously included tra-
111 jectories. Cosmic muon trajectories are also formed by using track start and end keypoints
112 to seed the track-building algorithm applied to only out-of-time subclusters. Neutrino and
113 cosmic muon candidates are the core outputs of the 3D reconstruction workflow.

114 For the individual neutrino interactions, further analyses are performed. Another CNN,
115 referred to as “LArPID”, assigns particle identification scores to individual particle trajecto-
116 ries. This LArPID network acts on two sets of images for a given individual particle cluster.
117 The first set of images are sub-images formed by cropping around the cluster’s projected
118 position on each wire plane image. These images include values for only those pixels at
119 the projected locations of spacepoints. The second set of images provided to LArPID is a
120 set of “context” images which use the same cropped location but include more pixels, only
121 masking out pixels with an out-of-time tag (those likely not produced by interactions asso-
122 ciated with the beam). The purpose is to provide LArPID with both a given cluster’s pixels
123 and information pertaining to the entire interaction. We believe (see section III 5) that the
124 context images are critical in maximizing the particle ID accuracy of LArPID. The context
125 images provide information the network can use to better ID the cluster. The context im-
126 ages also provide the means to overcome clustering errors from the 3D spacepoint algorithms
127 by providing information that might have been lost during clustering but is still present in
128 the images around the location of the clusters. The primary output of LArPID is particle
129 class scores for five particles: muon, charged pion, proton, electron, and photon. Particles
130 and their anti-particles are combined into the same class. LArPID also provides auxiliary
131 outputs in order to provide the option to make data selection cuts based on estimates of
132 the cluster reconstruction quality and as to whether the particle in question is a primary
133 particle emerging from a neutrino interaction vertex or a secondary particle descended from
134 the interactions of the primary particles.

135 The final outputs provided by the reconstruction are collections of candidate neutrino
136 interactions and cosmic muons. For each neutrino candidate, each prong (reconstructed
137 track or shower cluster) is provided a particle ID score from LArPID. Using this network’s
138 ID, the energy and 3-momentum are estimated for each particle. The kinematics estimator

139 for muons, protons, and charged pions is based on the visible tracklength and uses the
140 relationship between particle energy and the estimated length of fully ranged-out particles.¹
141 The energy estimator for the electromagnetic showers uses calorimetry based on charge.
142 Additional network outputs related to keypoint scores and LArPID estimates are also passed
143 along as outputs. The information for candidate neutrino interactions and their constituents
144 can then be used to develop physics analyses.

145 In the rest of this section, we provide more details for a subset of the components dis-
146 cussed above. We do not include discussions of the image pre-processing algorithms, the
147 in-time/out-of-time Wire-Cell tagger, and the SSNet CNN since their details can be found
148 in the indicated references. For each component described, we focus on outlining the core
149 approach of the algorithms, reference previous related work, and document key heuristics in
150 tuning their behaviors.

151 1. *Detector coordinate system and Data set terminology*

152 We will often visualize the outputs of the reconstruction or define performance metrics
153 assuming a specific 3D coordinate system. For the basis vectors, the positive \hat{x} -direction
154 runs in the direction of the anode to the cathode and points in the direction opposite to the
155 drift of ionization electrons towards the anode. The positive \hat{z} -direction runs in the same
156 direction of the neutrino beam. The positive \hat{y} -direction points upward to the sky. The
157 origin of the coordinate system is defined at the boundary of the TPC where $z = 0$ is the
158 side closest to the source of the beam, i.e. upstream, $x = 0$ is at the induction plane closest
159 to the drift volume, and $y = 0$ is located at the midpoint of the vertical TPC dimension.
160 The MicroBooNE TPC is a rectangle whose lengths are (256 cm, 233 cm, and 1036 cm)
161 along the (x, y, z) axes, respectively.

162 Another important definition is what constitutes an “event”. The values specified here
163 are particular to the MicroBooNE experiment. However, the overall data schema will be
164 similar for other LArTPCs utilizing sense-wires. Each event includes a set of waveforms
165 from each of the three wire planes that are arranged in a 2D array to make three wire plane
166 images, which we will refer to as “TPC images” or simple “images.” The three wire planes
167 of the MicroBooNE detector – from closest to the TPC drift region to the furthest – are

¹ This estimate is applied to tracks regardless of whether they range out inside or exit the detector. A more accurate estimate for exiting tracks will be the subject of future work.

168 the first induction plane, the second induction plane, and the collection plane. They are
169 so-named by the process with which ionization produces a current signal within the sense
170 wires. The three wire planes are given a label, 'U', 'V', and 'Y', respectively. Every event
171 will have exactly one TPC image from each of the three planes.

172 Each of the waveforms that makes up the images in an event consists of a time series
173 of 9600 voltage measurements, or samples, recorded every 0.5 microseconds. The primary
174 DAQ system for the MicroBooNE detector must be externally triggered (in other words
175 instructed) to capture a synchronous set of waveforms for all channels. The two trigger
176 types relevant for this work include (1) a signal synchronized with a firing of the neutrino
177 beam, typically referred to as a “spill” (which references the release of a bunch of protons
178 from the accelerator into a carbon target), and (2) a trigger signal produced by a signal
179 generator programmed to fire at regular intervals in a time window between beam spills.
180 The data recorded using the latter, non-beam spill, triggers are referred to as the “externally
181 triggered” or EXT data set. The MicroBooNE detector records waveforms in sync with the
182 Booster Neutrino Beam (BNB) produced by Fermi National Laboratory, and the data set
183 recorded in coincident with the firing of this beam is referred to as the “BNB” data. Later
184 in the sections demonstrating the performance of the reconstruction workflow through its
185 use in a neutrino event selection, only data from the BNB and EXT data sets are used.

186 **B. LArMatch: 3D spacepoints and keypoints generation**

187 The purpose of the LArMatch network, illustrated in figure 2, is to use the TPC wire plane
188 images to infer information related to the 3D location of ionization made by charged particle
189 trajectories. Inferring the true location of such ionization is not trivial as this essentially
190 requires inverting a tomographic projection, which by its nature will be an under-specified
191 problem due to the information lost during the projection operation. To make this difficulty
192 more concrete, we can consider trying to infer the location of energy depositions coming from
193 a uniform line of ionization where the line is parallel to the wire readout planes. Figure 3
194 provides an illustration showing the signal that would be seen in the wire plane images,
195 which is simply a line of uniform intensity across some set of wires all occurring at the same
196 time (i.e. region of TPC samples). A naive approach would be to ask “what is the set
197 of spacepoints that is consistent with producing a wire signal in all three planes?”. This

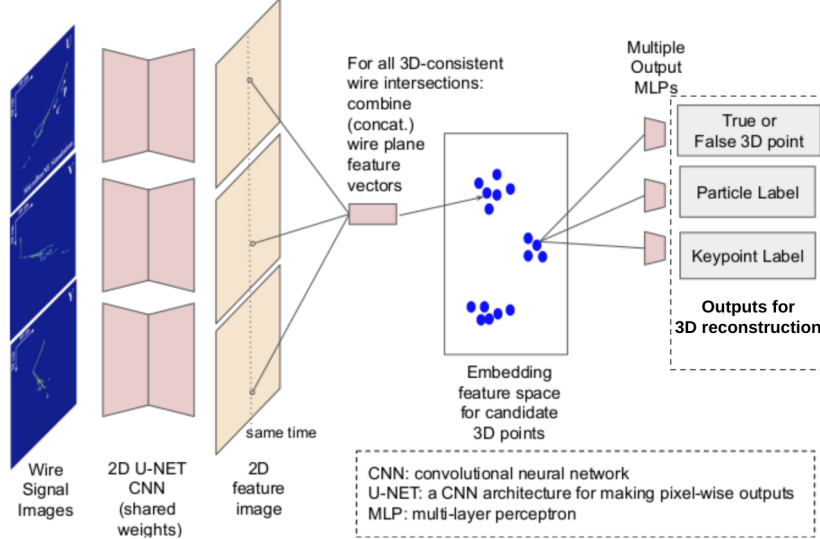


Figure 2: LArMatch network schematic. First, a U-Net CNN with residual convolutions takes as input three TPC images. For each input pixel, the CNN outputs a (16-dimensional) vector whose purpose is to represent the relevant patterns around a given pixel. Next, a non-ML algorithm proposes candidate spacepoints by forming all possible locations consistent with the charge deposition pattern in the images. The location of each proposed spacepoint is projected into the wire plane images in order to associate it a pixel from each wire plane. A (48-dimensional) feature vector for each spacepoint is made by concatenating the feature vectors belonging to the associated pixels. Three sets of multi-layer perceptrons (MLPs) then map the spacepoint vector to three types of outputs. One output is the score determining if a proposed spacepoint is located where a true energy deposition occurred. The second is a score for five particle types. The other output is a score indicating the location of several types of keypoints.

198 defines a 2D region of possible spacepoints, indicated by the purple region in the bottom
 199 illustration of Figure 3. The true locations of ionization would occur along a line within this
 200 region, indicated by the dashed line in the figure. One can select a subset of spacepoints in
 201 this region by utilizing some physical priors. If one assumes prior knowledge that (1) the
 202 true trajectory comes from a line segment and (2) the ends of the line must be consistent
 203 across the planes, then the set of possible spacepoints reduces to the correct region around
 204 the true path of ionization, as indicated by the yellow regions in the illustration of Figure 3.
 205 Another important refinement is to enforce some consistency in the signal intensity between
 206 the planes. In our example, one can use what in principle should be differences between the
 207 planes for the intensity per wire due to the different projected lengths of the ionization path
 208 onto the region around each wire. One can also impose a regularizing constraint such as
 209 biasing towards solutions that minimizes the number of spacepoints, which in this example

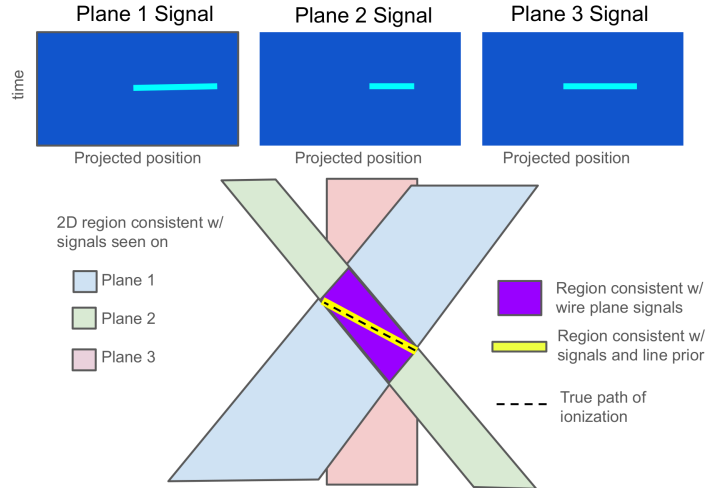


Figure 3: Example illustration of how inferring the 3D location of ionization can be an under-specified problem. We assume a line of uniformly distributed ionization occurs within the TPC and that the line is parallel to the wire planes. In this case, the wire plane images (top row) will contain a line of signal (cyan) occurring at the same time. Using only the knowledge of which wires on the planes see a signal, there is a 2D region in the TPC of possible spacepoints that are consistent with the wire plane signals (shown in purple). Only by also assuming a line shape and testing for consistency of the line length across planes can one determine the true region of ionization (shown in yellow) that corresponds to the true path.

210 can be seen to have a similar effect to having a line-like prior. These two latter approaches
 211 are a core part of the approach employed by the Wire-Cell reconstruction framework [18].
 212 What this example is meant to illustrate is the type of prior information or strategies needed
 213 to pick out the true points of ionization. While this example is the worst-case scenario for
 214 simple line trajectories, for LArTPC wire planes on the surface or in regions with many
 215 particles emerging from a neutrino interaction other degeneracies will arise.

217 The motivation for the LArMatch network is to complement charge consistency and reg-
 218 ularization by using machine learning to find additional features to match across the planes
 219 which improves the identification of true ionization points. One can imagine separating true
 220 3D energy depositions from false ones by learning to “match” local energy deposition pat-
 221 terns in one plane to another. These patterns must follow coherently from the underlying
 222 3D patterns of ionization. The algorithm thus proceeds in two steps. The first is to use a
 223 simple, deterministic algorithm to propose a large set of possible 3-wire intersections that
 224 might correspond to the location of real energy depositions in the detector. Next, a convo-
 225 lutional neural network (CNN) is trained to identify which 3-wire intersections are real or

226 false. We use what is known as a ‘U-Net’ for the CNN architecture. A U-Net maps the input
227 images to a set of latent vectors at each pixel whose purpose is to summarize the relevant
228 information in the neighborhood of the pixel. For a given 3D spacepoint, we project its
229 location onto each wire plane and associate a pixel from each. We then concatenate the
230 feature vectors from each pixel and pass them to a multi-layer perceptron which outputs a
231 score indicating if the spacepoint is real or false. The feature vectors are also used by other
232 MLP heads to produce additional information. In total, each feature vector is mapped to
233 three outputs: (1) a score indicating if the spacepoint is true or false, (2) a set of scores
234 classifying the spacepoint as one of five particle types, and (3) a set of scores related to how
235 far away the point is from five types of keypoints. In the following sections, we first describe
236 the algorithm that produces the spacepoint proposals from the wire plane images. We then
237 provide details on the image-to-feature vector U-Net. Finally, we discuss the three different
238 output heads.

239 1. *Proposal of 3-wire intersections, or “triplets”*

240 The first step to the LArMatch approach is to generate spacepoint candidates simply
241 based on minimal geometric plausibility. Initial spacepoints represent the location of 3-wire
242 intersections for wires with an above threshold signal coincident in time. We represent these
243 wire combinations as a “triplet” of integers whose components contain the index associated
244 with wires from each of the three wire planes. When the wire plane data is represented as
245 an image, the triplet refers to the tuple of column indices for the three wire plane images. In
246 order to not miss spacepoints that project onto non-responsive wires, the wire combinations
247 can include one wire which has been tagged as non-responsive. About 10% of the sense wires
248 in the MicroBooNE detector are classified as non-responsive. We do not try to make up for
249 missing spacepoints due to below threshold wire signals caused by ionization patterns that
250 cause destructive interference on the induction wires. These are associated with ionization
251 patterns where local segments are perpendicular to the wire planes. False positive and false
252 negative errors can also be induced by the presence of noise features on the wires.

253 We form a set of candidate triplets for each time tick (represented by a row in the 2D
254 wire-plane images) in the wire plane signals. The three column indices and row index specify
255 the projected pixel locations in the three wire planes. This information also specifies a 3D

256 location determined by (1) the location of the 3-wire intersection and (2) knowledge of
257 which image row represents the time coincident with the beam trigger combined with a drift
258 velocity assuming a perfectly uniform drift field.

259 The proposed spacepoints for an example simulated MicroBooNE event are shown in
260 Figure 4. Metadata, which captures the “truth” about the particle trajectories present in
261 each event, is saved during the simulation and used to create the ground truth labels for the
262 LArMatch network. This includes both a list of charged particle trajectories passing through
263 the TPC and the location of energy deposited by the particles. To save disk space, much of
264 this information is projected into an 2D array with the same dimensions as the wire plane
265 images, thereby facilitating the ability to determine the particle type or individual trajectory
266 ID that deposited the most ionization observed at a given 2D pixel. In the simulation, the
267 locations where energy was deposited by a particle is stored. For each pixel in the wire plane
268 image, we assign to it the largest energy deposition that contributed to the value in the pixel.
269 We then project this position into the other wire planes. The pixels on the other wire planes
270 then are used to calculate the shift in the number of columns between the pixels on the
271 two wire planes. In order to recover the YZ location of the largest energy deposit cluster
272 that contributed to the pixel in the starting plane, one calculates the 2D intersection of the
273 two wires from the different planes. The distance of the energy deposit from the wire plane
274 can be calculated from the time relative to the event trigger and the drift velocity. Given
275 that the wire planes are a tomographic projection of the 3D space points, this method of
276 saving the 3D locations does not allow for perfect inference. However, we find the accuracy
277 is sufficient to construct the ground truth for the LArMatch network, while reducing the
278 amount of data to be saved. For future work, it would be worth exploring a better method
279 of compressing the 3D energy deposition information that is not inherently lossy.

280 In figure 4, the proposed spacepoints for one event are shown along with the ground
281 truth ‘true’ or ‘ghost’ labels built from the simulation metadata. Spacepoints near a true
282 location of ionization are given the “true” ground truth label shown in red. The rest of the
283 spacepoint proposals are given the “false” ground truth label shown in blue. We highlight
284 two regions of this figure. The first is the volume between $z=[600\text{ cm},800\text{ cm}]$. Here, many
285 short line-like regions of false spacepoints are seen. This is due to a fairly large region of
286 unresponsive wires on one of the wire planes (the “Y” collection plane). In these regions, the
287 requirement to propose a spacepoint is relaxed from requiring ionization to be observed on

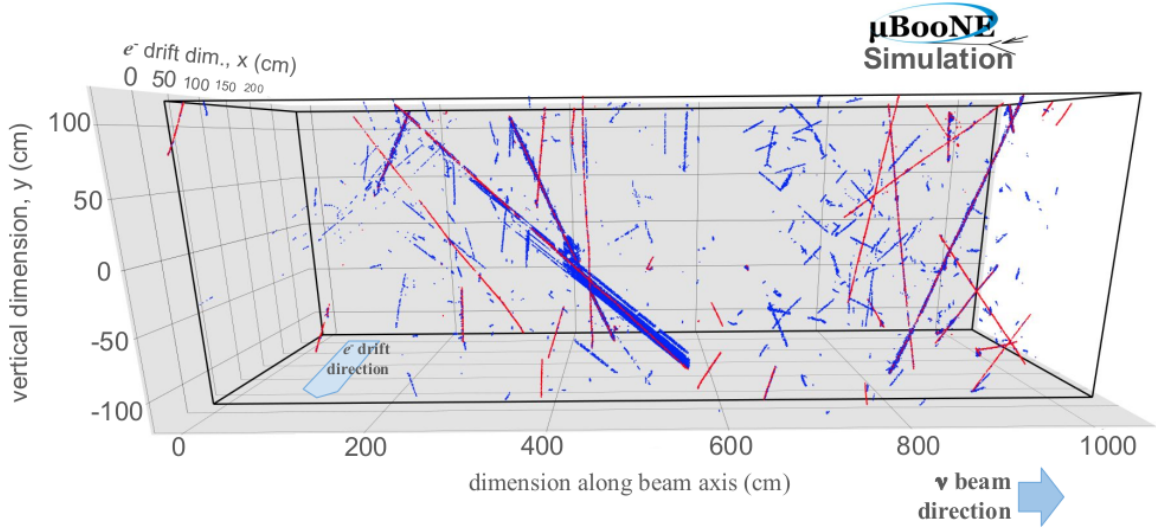


Figure 4: Initial spacepoint candidates for an example simulated MicroBooNE event. The “true” spacepoints located near regions of ionization are colored in red. The “false” or “ghost” spacepoints that are not near ionization are colored in blue.

288 only two (as opposed to all three) wire plane images. We make this accommodation with the
 289 aim of minimizing the amount of missing ionization at the cost of potentially accepting more
 290 false positives. The idea will be to use a downstream algorithm, specifically a particle-level
 291 CNN, to correct for false spacepoints or clustering mistake. The other region to point out in
 292 Figure 4 is the relatively large region of false (i.e. blue points) surrounding one muon track
 293 between $z=[400 \text{ cm}, 600 \text{ cm}]$. This is where a portion of a cosmic muon is parallel to the
 294 wire planes, similar to the illustration discussed earlier.

295 2. Feature Generating U-Net

296 The core part of the LArMatch network is the U-Net [23] CNN mapping images to pixel-
 297 wise feature vectors. We use residual convolutions [24] over standard convolutions. There are
 298 a total of six convolutional layers including five downsampling layers, each time with stride
 299 two. When normalization layers are used, we use instance normalization [25]. We upsample
 300 on the decoder part of the network with convolution-transpose operations. Because the wire
 301 plane images are sparse, i.e. most pixels have a value very nearly zero, the network uses
 302 sparse-submanifold convolutions [26] as implemented by the MinkowskiEngine library [27].
 303 The U-Net takes in a sparse tensor representation of a single wire plane image at a time

304 and is applied to each wire plane, separately. In other words, the input of the U-Net is a
 305 sparse tensor, \mathbf{s} , which consists of a list of N pixels, which is a subset of all the pixels in the
 306 image. To be included into the sparse tensor, a pixel had to pass two criteria. One was that
 307 the pixel had a value above some threshold value. We used a threshold of ≥ 10.0 , or what
 308 is about a quarter of the average pixel value for minimum ionization sections from cosmic
 309 muon tracks. The second criterion is that a pixel, with a below threshold value, was from a
 310 non-responsive wire while also being the projected location of a proposed spacepoint. The
 311 sparse image tensor, \mathbf{s} , is represented through a pair of tensors. The first is a coordinate
 312 tensor, $\mathbf{c} \in \mathbb{W}^{N \times 2}$, which contains the indices of the above threshold pixels. The second is
 313 a feature tensor, $\mathbf{f} \in \mathbb{R}^{N \times 1}$, containing the associated pixel values. The U-Net, therefore,
 314 maps $\mathbf{s} = (\mathbf{c}, \mathbf{f})$ to N 16-dimensional feature vectors, $\mathbf{v} \in \mathbb{R}^{N \times 16}$.

315 3. Spacepoint real/ghost classifier

316 A 2-layer MLP is used to classify each proposed spacepoint as either real or ghost. This
 317 classifier takes in the concatenated 48-dim feature vector, \vec{v} , formed from the individual 16-d
 318 feature vectors from the project pixels from each plane. The MLP has two hidden layers,
 319 each with 32-features, and outputs both a real and ghost class score. A softmax function
 320 normalizes the sum of these scores to 1.0. We use the normalized score for being a true
 321 spacepoint, $p(\vec{v})$, for classifying proposed spacepoints.

322 We train the network to optimize this prediction using a focal loss [28] objective. We also
 323 weight each spacepoint based on the relative total number of ground truth-labeled real and
 324 ghost points. This weighting is used to mitigate bias that might favor true negative predic-
 325 tions coming from the higher frequency of ghost spacepoints compared to real spacepoints.
 326 Our training objective is

$$\min_{\theta} \mathcal{L}_{ghost} = \min_{\theta} \left[\sum_b^{N_b} \left[\sum_{i_t}^{N_{i_t,b}} w_{b,t} \log(p_{\theta}(v_{i,t}))(1 - p_{\theta}(v_{i,t}))^{\gamma} + \right. \right. \tag{1} \\
 \left. \left. \sum_{i_f}^{N_{i_f,b}} w_{b,f} \log(1 - p_{\theta}(v_{i,f}))(p_{\theta}(v_{i,f}))^{\gamma} \right] \right].$$

327 We optimize the objective using AdamW, an implementation of stochastic gradient descent

328 with features such as adaptive gradient normalization and momentum. We train our models
 329 with randomly sampled batches of data. The parameters of both the UNet and the MLP
 330 heads producing the LArMatch outputs are learned simultaneously in one combined training
 331 procedure. Within a batch of N_b training samples, the b -th sample consists of N_b feature
 332 vectors, v_i produced by the UNet for all N_b candidate spacepoints. We use the simulation
 333 meta-data to produce ground truth labels for the set of vectors, v_i . The subset of $N_{b,t}$
 334 'real' or 'true' ground truth-labeled vectors is $v_{i,t}$; the subset of $N_{b,f}$ 'ghost' or 'false' labeled
 335 vectors is $v_{i,f}$ (with $N_b = N_{b,t} + N_{b,f}$). The likelihood estimate for being a real point is
 336 $p_\theta(v_i)$ and is approximated by the output of the true/ghost MLP, parameterized by θ . The
 337 $(1 - p_\theta(v_{i,t}))^\gamma$ and $(p_\theta(v_{i,f}))^\gamma$ are the focal-loss factors. As $p_\theta(v)$ approaches the ground truth
 338 value (1.0 for real points, 0.0 for ghost points), the focal loss factors increasingly down-weight
 339 these examples with the γ meta-parameter controlling how quickly the downweighting occurs
 340 with increased confidence. Conversely, the spacepoints whose classification is incorrect will
 341 contribute more to the update of the model parameters. In effect, the focal loss is intended to
 342 nudge the optimization towards improving "harder" examples over increasing the confidence
 343 for easy examples.

344 4. *Spacepoint Keypoint score*

345 The LArMatch network also is tasked with providing the outputs to identify locations of
 346 ionization that can be useful for later 3D trajectory reconstruction. We defined six classes
 347 of "keypoints": (1) a neutrino interaction vertex, (2) the start of a track-like trajectory
 348 (defined as belonging to a muon, proton, charged pion, and other heavy mesons), (3) the
 349 end of a track-like trajectory, (4) the start of EM shower not produced by processes in the
 350 following types, (5) the start of EM showers produced by the decay of a muon, and (6) the
 351 start of EM showers from delta rays (typically radiating from energetic muon tracks).

352 The way the location of possible keypoints is represented in the output of the network
 353 is through a score made for each spacepoint. The score ranges from 0 to 1.0, with scores
 354 inversely proportional to the distance to a keypoint. The network is trained to reproduce a
 355 score distribution that follows a Gaussian with a uniform, uncorrelated variance. In other
 356 words, the network is asked to produce a heat map near keypoints with the hotspots having
 357 a set shape. A post-processing step can then be used to identify hotspots and use the

358 spatial score distribution to fit to the precise keypoint location. The ground truth-score is
 359 calculated using meta-data from the simulation which retains the creation point of charged
 360 track-like particles and the earliest location of ionization within the TPC of an EM shower.
 361 All particles whose meta-data information was used to define EM shower keypoints were
 362 required to have at least one wireplane image with 20 or more pixels whose signal was
 363 attributed to its ionization.

364 A 2-layer MLP, s_θ is used to map each spacepoint’s feature vector, \vec{v} , to a vector, $\vec{k} \in \mathcal{R}^6$,
 365 whose components are the scores of each keypoint class. The value of each component is
 366 independently kept within the range of $[0, 1]$ by applying a sigmoid-function element-wise.
 367 This bounded output is then compared to the ground truth scores for each keypoint class.

368 Both the dedicated keypoint MLP and the UNet parameters are optimized to minimize
 369 the keypoint training objective, $\mathcal{L}_{keypoint}$, given by

$$\mathcal{L}_{keypoint} = \frac{1}{N_b} \sum_b \left[\frac{1}{N_c} \sum_c \left[\sum_i^{N_{b,t}} w_{b,c,t} (\hat{s}_{i,c,b,t} - s_\theta(\vec{v}_{i,b,t}))^2 + \sum_j^{N_{b,f}} w_{b,c,f} (\hat{s}_{j,c,b,f} - s_\theta(\vec{v}_{j,b,f}))^2 \right] \right]. \quad (2)$$

370 For the above equation, the sum over N_b is over the number of examples in each training
 371 batch. Each example consists of proposals from one set of wire plane images from one TPC
 372 readout event. The sum over N_c is over the six different keypoint classes. Because most
 373 spacepoint proposals are unlikely to be near a true keypoint, to aid training, we use weights
 374 to balance the contribution of examples near true keypoints, for which the MLP needs to
 375 output a score, and those far away from true keypoints, for which the MLP only needs to
 376 output zero. Therefore, for each class we split the total number of spacepoint proposals in
 377 the b -th example, N_b , into “true example” points within 10 cm of a true keypoint and “false
 378 example” points which are not. Thus, in the above equation, the sum over $N_{b,c,t}$ is for the
 379 true example spacepoints for class c , while the sum over $N_{b,c,f}$ for the false examples for
 380 class c within the b -th example of the batch. Regardless of the class, the number of true and
 381 false examples total to the same number of spacepoint proposals, i.e. $N_{b,c,t} + N_{b,c,f}$. The
 382 true example weight for class c , $w_{b,c,t}$, is set to the ratio of the total number of spacepoints,
 383 $N_{b,c,t} + N_{b,c,f}$, over the number of true examples in the b -th training example. Similarly,

384 the weight, $w_{b,c,t}$, is the ratio of the total number of spacepoints over the number of false
 385 examples in the b -th training example. For each true (false) spacepoint, the contribution
 386 to the loss is the weighted squared-difference between the keypoint MLP output, $s_\theta(\vec{v}_{i,b,t})$
 387 ($s_\theta(\vec{v}_{j,b,f})$), which is a function of the feature vector, $\vec{v}_{i,b,t}$ ($\vec{v}_{j,b,f}$), of the i -th (j -th) spacepoint
 388 in the b -th training example. The ground truth score for a given spacepoint is labeled by
 389 $\hat{s}_{i,c,b,t}$ and $\hat{s}_{i,c,b,f}$.

390 5. *Weighting the Multi-objective Loss*

391 We use a dynamic weighting of the different task objectives when forming the final, overall
 392 loss function. This technique changes the relative weights of the tasks based on an estimate
 393 of the uncertainty. This method in effect aims to encourage parity in the contribution of the
 394 terms to the total loss throughout the training period. In our application, the total loss is

$$\mathcal{L}_{larmatch} = e^{-s_{ghost}} \mathcal{L}_{ghost} + e^{-s_{keypoint}} \mathcal{L}_{keypoint} + s_{ghost} + s_{keypoint}. \quad (3)$$

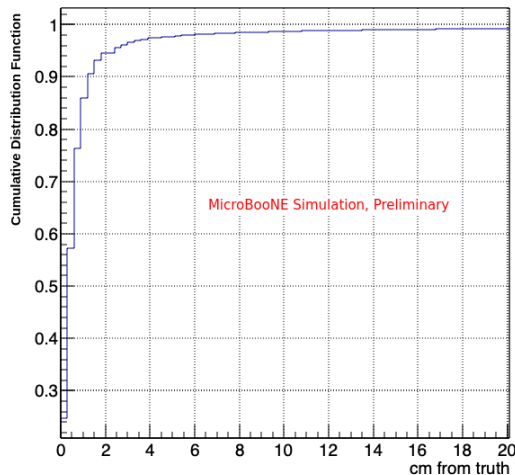
395 C. 3D Particle Trajectory Reconstruction

396 The 3D reconstruction of individual particle trajectories is designed around the outputs
 397 produced by the LArMatch CNN, the SSNet CNN, and the Wire-Cell out-of-time tagger.
 398 The fundamental input to the reconstruction is the set of spacepoints produced by the
 399 LArMatch stage. The algorithms described below first create clusters belonging to individual
 400 particles. This is followed by building a representation of the trajectory. A line segment, fit
 401 to a cluster’s spacepoints, is used to represent track-like particles. A cone, whose axis is fit
 402 along an initial path of spacepoints, represents shower-inducing particles. These outputs are
 403 more easily achieved by the pattern recognition performed by the previous CNNs, alleviating
 404 the need to find the necessary patterns within the set of spacepoints, directly.

405 The upstream outputs are first used to refine and partition the candidate spacepoints.
 406 First, the LArMatch real/ghost score is used to filter ghost points. A ‘real’ spacepoint score
 407 threshold of 0.8 is applied to remove ghost points. This score value removes approximately
 408 90% of ghost points and keeps approximately 75% of true points. The cut value chosen favors
 409 background rejection in order to keep the typical run time of downstream algorithms between

410 10-20 seconds per event. Next, the Wire-Cell out-of-time/in-time label splits the spacepoints
 411 into two sets: ‘in-time’ and ‘cosmic’. Both of these sets are subdivided into track and shower
 412 hits using the scores from the 2D SSNet CNN. At this stage of the reconstruction, we have
 413 four buckets of spacepoints: in-time-track, in-time-shower, cosmic-track, and cosmic-shower.

414 Because of spacepoint proposal’s very forgiving criteria, the density of points around the
 415 true trajectory can be high with many spacepoints providing redundant information. We
 416 apply a heuristic to remove points away from the core of the trajectory. For each plane, we
 417 only tag one spacepoint to keep per pixel, choosing the spacepoint with the largest LArMatch
 418 real/ghost score. The final set of spacepoints we keep are the union of all the spacepoints
 419 associated with pixels from each plane. This heuristic is applied to the in-time-track, in-time-
 420 shower, and cosmic-track spacepoint partitions. Figure 5 shows the fraction of space points
 421 that are within some distance of a true muon, charged pion, or proton trajectory within the
 422 TPC. The simulated data used to make the plot in this figure contained simulated cosmic
 423 particles (mostly muons) and neutrino interactions. About 90% of spacepoints are within 1
 424 cm of track-like trajectories.



425 Figure 5: Fraction of spacepoints vs. distance from the ground truth trajectory of a true
 426 muon, charged pion, or proton trajectory within the TPC.

427 D. Keypoint Generation

428 The output of the LArMatch keypoint proposal CNN are pixel-wise scores. This infor-
 429 mation needs to be distilled into individual keypoint candidates. Ideally, the scores from

430 the network should be arranged spatially as spherical hotspots. We separate the hotspots
431 by first retaining keypoints with a minimum score and then using density-based clustering
432 algorithm, DBSCAN, to identify individual candidates. The location of a keypoint is taken
433 to be the spacepoint within a cluster with the highest keypoint score. Spacepoints part of a
434 reconstructed keypoint are tagged and removed from the original pool. The scores of points
435 within the remaining pool are modified by using the set of newly created keypoint locations
436 to subtract the expected score contributions (defined by a Gaussian function). The modified
437 score is clamped to be zero or greater. This keypoint-finding procedure is applied twice, first
438 with a high keypoint score threshold and again with a lower score threshold. This procedure
439 is applied separately for each type of keypoint. As a result, a spacepoint can be a part
440 of keypoint clusters for multiple classes. However, a spacepoint can only be part of one
441 keypoint cluster within the same class.

442 Keypoints from all six classes are searched for within the 'in-time' spacepoint partition.
443 Only track-start and track-end types are constructed from the 'out-of-time' spacepoint par-
444 tition. All of the above keypoints will be used by the next set of algorithms to seed the
445 creation of particle clusters.

446 In the future, keypoints with the remaining classes can be built using the out-of-time
447 spacepoints. This could be used to reconstruct cosmogenic particle clusters, beyond those
448 for cosmic muons, with the intended use of creating side-band datasets. For example, it
449 might be useful to reconstruct out-of-time neutron-induced interactions. These could be
450 identified by track-start keypoints or regions with high neutrino-like scores as they often
451 mimic NC-like final states.

452 **E. Particle and Interaction Reconstruction with 3D Spacepoints**

453 Two different sets of algorithms are used to form track-like and shower-like clusters.
454 However, both take the approach of trying to form pure sub-clusters and then using heuristics
455 to stitch together the subclusters belonging to individual particles.

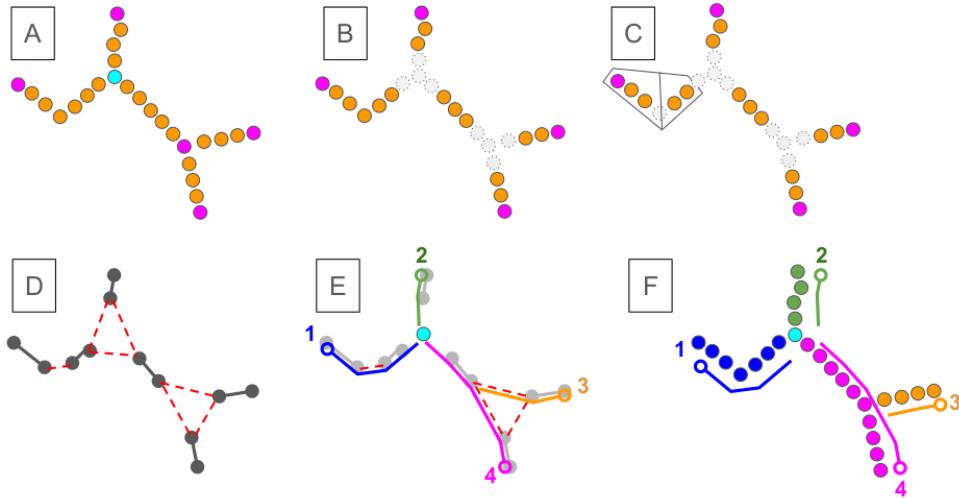


Figure 6: Schematics of the steps of the track reconstruction. (A) Spacepoints with track-like and in-time labels are collected along with start and end keypoints (here a start keypoint is shown in cyan; end keypoints are in magenta). (B) Spacepoints around certain keypoints are removed from clustering. (C) Spacepoints are clustered and then broken into straight pieces based on the convex hull around the points. (D) Clusters are represented as a line segment with two ends. Line segments between end points within a certain distance are formed. A graph is defined with nodes defined by the cluster end points and two types of edges defined by the line segments within charge clusters (black solid lines) and those between clusters (red dashed lines). (E) Track-start keypoints are used to seed a depth-first graph traversal algorithm that proposes possible tracks. (F) Spacepoints are assigned to nearby line-segments and together define a candidate particle track. In this schematic, four candidates are proposed.

456 1. *Forming track candidates*

457 For track-like particles, we form subclusters by looking for neighboring spacepoints ar-
458 ranged in a straight line. We start by using DBScan to form clusters of neighboring space-
459 points. To avoid clustering spacepoints from multiple particles, we apply several heuristics.
460 The first is that we remove spacepoints within a 3 cm radius of reconstructed keypoints. This
461 length is three times the DBScan maximum distance parameter of 1 cm in order to ensure
462 points from different particles emerging from a vertex or secondary interaction point will not
463 be clustered together. (A cartoon of this step is shown in Figure 6B). This is done to separate
464 spacepoints coming from the locations of neutrino interactions, secondary interactions, or
465 decay. The other heuristic aims to find locations of intersecting trajectories. The approach
466 is to recognize 'vee' patterns using the convex hull around the set of pixels corresponding
467 to the projected spacepoint location on the wire planes. This reuses algorithms built for

468 the one 1-lepton-1-proton exclusive analysis in the previous MicroBooNE low-energy excess
469 search [29]. We use convex hull defect points to identify intersecting trajectories and the
470 location to split the clusters assuming either an 'X'- or 'V'-shaped 3D spatial pattern. (A
471 cartoon of this step is shown in Figure 6C).

472 We build individual particle tracks by chaining, end-to-end, the straight-line subclusters.
473 We use a recursive depth-first graph traversal algorithm to build chains of subcluster seg-
474 ments. This algorithm begins by defining a graph whose nodes are the collection of line
475 segment endpoints. Two types of edges are defined between the nodes. The first edge type
476 (A) connects endpoint nodes belonging to the same subcluster. The second edge type (B)
477 connects endpoint nodes below some max distance. (A cartoon of this step is shown in
478 Figure 6D with the A-type edges represented as solid black line segments and B-type edges
479 as dashed red line segments.) Multiple B-type edges between the endpoints of two line
480 segments can be formed.

481 Once the graph is formed using all the subcluster line segments, a recursive graph traversal
482 algorithm is used to build chains of line segments representing candidate track trajectories.
483 The sub-set of endpoint nodes sufficiently close to designated keypoints serve as starting
484 points. (A cartoon of this step is shown in Figure 6E.) Using depth-first recursion, a tree-
485 structured subgraph for each seed node is built by traversing edges of alternating type,
486 starting with A-type edges. Heuristics based on angles and distances between edges and
487 segments were used to choose and prioritize B-type edges to include in the tree. For potential
488 B-type edges less than 3 cm, the cosine between the track segments that this B-edge would
489 connect is required to be greater than zero. For edge lengths between 3 to 10 cm, the cosine
490 between track segments must be greater than 0.7. For lengths longer than 10 cm, the cosine
491 must be greater than 0.9. We allow for such fairly large distances between track segments
492 in order to cross regions of unresponsive wires that occur within the detector. These values
493 were optimized to maximize the completeness of simulated cosmic muon tracks. To prevent
494 loops, nodes can only be visited once.

495 Paths within a tree subgraph that connect the root node to the leaf nodes represent
496 candidate trajectories. Possible paths are selected using the heuristic that true trajectories
497 run along regions of ionization. This is quantified by the fraction of the trajectory length
498 that projects onto locations within the wire plane images that are near pixels with sufficient
499 ionization. Paths satisfying this criterion are scored based on weighted sum of the total path

500 length, the trajectory fraction near ionization, whether the end of the path coincides with
501 a track-end keypoint, and a measure of the overall trajectory straightness. Valid paths are
502 then sorted by descending score.

503 Candidate track particles are created from the set of paths, starting with the highest
504 scoring. The ordered collection of line segments define the trajectory of the track. Track-
505 like spacepoints close to the line segments form a cluster associated with the trajectory. Any
506 remaining paths that fork from the current highest-scoring path are used to define secondary
507 tracks that begin at the last common node. Once a track trajectory is created, any segments
508 included in the path are forbidden to be reused. Any remaining path is removed if it includes
509 any A-type edges corresponding to segments included in a track. Track creation continues
510 with the remaining highest-scoring path and completes once the set of valid paths is empty.

511 Candidate tracks are created in this way for all starting nodes. An individual subcluster
512 line segment can be a part of multiple track candidates, as long as the tracks were created
513 using different starting nodes. Once all candidate tracks have been formed for a given pool
514 of track subclusters, refinements to the line segment trajectory are made for each track can-
515 didate. The refinements consist of creating new points along the segmented line such that
516 a chosen maximum distance occurs between points. The locations of the expanded set of
517 points are iteratively perturbed using gradient descent in order to minimize squared-distance
518 between projected wireplane positions and pixels with ionization. Once refinements of the
519 line-segment trajectories are completed, 3D spacepoints are associated with each trajectory.
520 First, spacepoints in the sub-clusters used to make the trajectory are added. Second, space-
521 points close to keypoints, which were vetoed initially, are added to the trajectory. The
522 collection of spacepoints along with the line segment trajectory represent the candidate par-
523 ticle tracks. (The final track candidates in the diagram of Figure 6, defined with both a line
524 segment trajectory and associated spacepoints, are shown in sub-figure F.)

525 2. *Forming shower candidates*

526 The approach taken for forming shower candidates is to assume that shower keypoints are
527 located at the start of a shower and then to collect 3D spacepoints, tagged as shower-like by
528 SSNet, belonging to the shower. Points are added to a candidate shower if they fall within
529 a cylindrical region around the shower's reconstructed direction. To determine the shower

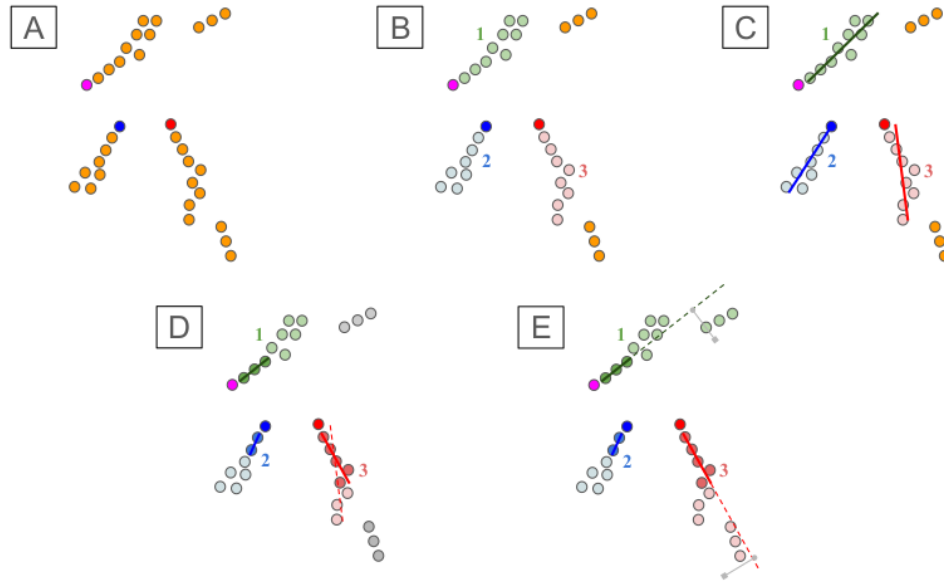


Figure 7: Schematic illustrating steps of the shower reconstruction. (A) Spacepoints with shower-like and in-time labels are collected along with shower keypoints. The shower points are colored orange. Shower keypoints are given random colors. (B) DBscan is used to cluster the points based on neighbor distances. Found clusters are assigned a random color and index. There are some points shown which did not have enough points to form a cluster. (C) The first principal component direction and keypoint define the initial direction of the shower. (D) A subset of points within each cluster near the keypoint is used to define a shower trunk. (E) The trunk direction and keypoint defines a line. Clusters close to this line are added to the shower candidate, defined by a keypoint, shower trunk, and cluster of shower spacepoints.

530 direction, a shower “trunk” is defined as a line that running along the first 3-10 centimeters
 531 of ionization at the start of the shower.

532 The shower reconstruction begins by gathering, as input, spacepoints that have been
 533 filtered to have (1) an SSNet shower score greater than 0.5, (2) a LArMatch ‘true’ score of
 534 0.8 (the same threshold for accepting spacepoint candidates), and (3) to be associated with
 535 pixels that have not been tagged as being out-of-time with the beam, (in other words does
 536 not have a cosmic tag). The algorithm also requires a set of shower keypoints. In figure 7a,
 537 spacepoints satisfying the conditions are shown as orange circles. Different candidate shower
 538 keypoints are also shown in figure 7a in random colors, here blue, red, and magenta.

539 Next, DBscan is used to build shower subclusters and is run with the following parameters:
 540 a maximum distance of 5.0 cm, minimum cluster size of 20, and max nearest neighbors of
 541 20. The somewhat higher minimum points to form a cluster is meant to reduce the number

542 of small disconnected shower fragments. In the illustration in figure 7b, three clusters are
543 found are given a random color and index. Note the smaller fragments which do not form a
544 cluster. The first principal component (PC) is then calculated for each cluster. To remove
545 very short clusters, any cluster whose first PC length – measured by the maximum distance
546 between pairs of points projected onto the first PC line – is shorter than 1 cm is rejected.
547 In the illustration in figure 7c, examples of PC axes for each cluster is shown.

548 Next, the shower keypoints are used to find a good shower “trunk.” For all keypoints
549 within 10 cm of the axis-aligned bounding box of each shower cluster, a subset of cluster
550 points within a certain radius of the keypoint are collected. For each subset of points, a
551 first PC axis is found and defines the axis of the shower trunk. A subset of points is made
552 three times for each keypoint and cluster pair, using a radius of 3 cm, 5 cm, and 10 cm. In
553 all cases, the keypoint is required to be at most 1 cm from the nearest cluster spacepoint in
554 order to be able to define a valid shower trunk. In studies of the dE/dx along the true initial
555 direction of simulated electron showers, the energy loss per unit length was most separable
556 between electrons and photons between 1 cm to 3 cm. The upper bound was interpreted
557 to be approximately the length scale where some aspect of the shower’s cascade has begun,
558 causing a widely varying dE/dx that differs from just ionization. Of the three candidate
559 trunks, we choose the one to represent the cluster’s trunk based on which is the most line-
560 like. This is quantified using the ratio between the second-to-first principal component of
561 the cluster’s spacepoints.

562 At this point in the shower reconstruction, each shower candidate includes the cluster
563 points, a shower trunk, and the seeding shower keypoint. Figure 7d provides an example
564 where a shower trunk has been found for each of the three clusters in the illustration. Note
565 that a subset of points, marked with a darker color, are tagged as being part of the shower
566 trunk, can fall within different radii of their respective keypoints.

567 Finally, we attempt to add additional shower points to each candidate shower cluster.
568 We do not add individual points, but instead test to see if we should add an entire cluster’s
569 points to a shower candidate. For each shower candidate, we loop through all shower clusters
570 and ask which fraction of the cluster’s points are within a volume around the line defined
571 by the shower trunk’s direction and the position of the keypoint. The acceptance volume
572 is split into two regions. The first volume is for points in the “forward direction” of the
573 shower, which must be (1) within 5 cm of the trunk axis while (2) it’s projected distance

574 along the axis is less than 50 cm from the keypoint. The second volume is for points in the
575 “backward direction” of the shower. These points must have as projected distance within
576 3 cm of the keypoint and be within 3 cm of the trunk axis. This second volume is meant
577 to help with cases where the shower keypoint is reconstructed a few centimeters into the
578 trunk. If half of the points within the cluster falls within the volume defined by the shower
579 candidate trunk, all of the spacepoints are added to the shower candidate. In our illustrative
580 examples, figure 7e depicts successful tests to add a cluster of points to shower candidates
581 1 and 3 as each have a cluster whose points are within some distance of the trunk’s line.

582 Note that the shower cluster merging condition at this point of the reconstruction is rel-
583 atively restrictive. We later use the neutrino vertex to help merge shower cluster candidates
584 into bigger, more complete shower clusters. This cluster merging occurs when neutrino in-
585 teraction candidates are being constructed. We start the process of building showers by
586 tagging a subset of shower candidates found from the procedure above as “shower prong”
587 candidates. These are intended to represent the beginning of a possibly larger shower emerg-
588 ing from a neutrino interaction. Prongs are first identified based on how well they point
589 back to the neutrino vertex. To qualify as a prong, the shortest distance between the line
590 defined by a shower cluster’s trunk direction and the neutrino vertex (often described as
591 the impact distance in other scattering contexts) is below 20 cm. The shower prongs that
592 qualify are then sorted by those with the smallest distance to those with the largest. Then,
593 beginning with the prong with the smallest distance, we then loop over all shower clusters
594 and decide on merging each into the prong if a cluster falls within a cone defined by the
595 prong. The cone is defined by an axis whose starting point and direction are defined by the
596 prong’s trunk. Because the trunk is a line segment, the endpoint of the trunk closest to the
597 neutrino vertex is designated as the tip of the cone. The trunk line segment is used to define
598 the ray of the cone such that the direction of the ray is away from the neutrino vertex. The
599 opening angle of the prong cone is 30 degrees. This is the angle of a right triangle whose
600 height is approximately 2 Moliere radii (9.04 cm in liquid argon) and whose base is 50 cm
601 (or about 3.5 radiation lengths) [30]. We add other ‘test’ shower clusters to the prong by
602 determining if the test cluster falls within the prong’s cone. To determine this, we ask if the
603 test cluster’s trunk endpoint closest to the neutrino vertex is within the 30-degree opening
604 angle. We iteratively define a new prong and associate available shower clusters to it, all the
605 while tagging clusters as unavailable and skipping them if they were used to define a prong

606 or were merged into a prong. In this way, we use the neutrino vertex to help sort the order
607 of shower candidates and thus bias which ones should serve as the starting prongs on which
608 to build.

609 **F. Interaction Candidate Formation**

610 The formation of neutrino interaction candidates begins with associating neutrino key-
611 point candidates with track subcluster segments and shower-trunk candidates. The track
612 subclusters derive from the in-time-track spacepoints. The shower subclusters and trunks are
613 made from the in-time-shower spacepoints. Both types of subclusters are added as 'primary
614 prongs' based on the distance between (1) the vertex and the closest segment endpoint and
615 (2) the neutrino keypoint and the prongs first principal component axis. The graph-based
616 algorithm described above is used to build candidate tracks using only the neutrino keypoint
617 as a seed. The cone-based procedure described above is used to construct shower candidates
618 using the associated shower prongs. For any shower subclusters assigned to multiple shower
619 candidates, we prevent over-counting of visible energy by forbidding subclusters from being
620 added to multiple shower prongs in this context. The track and shower candidates created
621 at this stage of interaction reconstruction are tagged as primary prongs. At this stage, we
622 also correct for potential reconstruction errors due to small clusters of spacepoints being
623 mislabeled as track-like by the SSNet CNN. One algorithm checks for such track-like clus-
624 ters that might occur at the beginning of a shower. For each shower prong, a line between
625 its start point and the vertex is defined. We then check for any track clusters with over 90%
626 of its spacepoints within 3.5 cm of this line or within 2 cm of the shower's trunk, for which
627 the latter is defined by a line segment up to 10 cm long. We also check for short track-like
628 subclusters that lie deeper within a shower, beyond the trunk. When such track clusters
629 are detected, the track cluster is removed and its spacepoints are added to the shower's
630 spacepoint container.

631 With the set of primary particles defined, the next step of the reconstruction is to add
632 secondary particles to the candidate neutrino interaction. The search for secondaries starts
633 by finding track and shower subclusters whose starting points are within 2 cm of any of the
634 associated primary tracks or whose first principal component forms a line that approaches
635 within 2 cm. For each secondary track prong, the graph-based track builder is used to

636 create track particles. Likewise, for each secondary shower prong, the cone-based shower
637 building algorithm is used to construct a secondary shower particle. This secondary particle
638 reconstruction continues to iterate until no additional track-like or shower-like subclusters
639 are associated with the interaction.

640 The construction of neutrino candidates concludes with routines to estimate the energy
641 of tracks using range under the assumption of a few particle species. The initial direction
642 of the track is also estimated. Calorimetric estimates of the total ionization are made by
643 summing the pixel values of individual wire plane images. This leads to three plane-specific
644 estimates for each shower. An initial integral-to-energy conversion is applied. Details for
645 these energy estimates are in Section II H.

646 In addition to neutrino interactions, the reconstruction also builds cosmic muon tracks
647 using the graph algorithm seeded by track-start and track-end keypoints. The tracks are
648 made using clusters coming from the cosmic-track spacepoints.

649 This interaction-building stage is the final step of the 3D spacepoint-based reconstruction.
650 The neutrino interactions and their candidate primary and secondary particles are saved for
651 analysis. The spacepoints and their associated scores are saved only for those assigned to a
652 particle that is part of a neutrino candidate. These products will be used by the CNN-based
653 particle ID to be described in later sections. The scores of the keypoints are also stored for
654 selection and analysis purposes.

655 **G. Reconstruction Validation**

656 The algorithms described in the previous sections are able to efficiently reconstruct neu-
657 trino interactions and final state particles. This section presents validation plots exploring
658 vertex and prong reconstruction quality using a sample of MC neutrino interactions (overlaid
659 over cosmic-ray background data) occurring inside the MicroBooNE fiducial volume (defined
660 as 3cm from the edge of the space-charge-corrected TPC boundary as in [17]). The ability
661 of our reconstruction outputs to select CC ν_μ and CC ν_e events with high efficiency and
662 purity is explored in sections III A and III B. These metrics are defined by the fraction of
663 selected events relative to all charged-current events whose vertex occurs within the fiducial
664 volume.

666 Figure 8a shows the efficiency of our neutrino vertex reconstruction as a function of
 667 simulated neutrino energy for CC ν_μ and CC ν_e interactions. Vertex efficiency is higher for
 668 CC ν_e events, but is high in both cases, rising above 80% by 0.5 - 0.6 GeV in neutrino energy
 669 and leveling off at around 85% - 90% above 1 GeV. Below 0.5 GeV, vertex reconstruction
 670 efficiency drops steeply (as expected), falling below 60% around 0.2 - 0.3 GeV. Figure 8b
 671 shows how accurate the vertex reconstruction is in cases where a candidate neutrino vertex
 672 is found. From this area normalized distribution of the distance between the reconstructed
 673 and true neutrino interaction vertex (for all MC neutrino interactions), we can see that the
 674 vast majority of reconstructed vertices are within 1cm of the true position. More specifically,
 675 68% of reconstructed vertices are within 9.2mm of the simulated interaction position. The
 676 spacing between wires is 3mm, so we can reconstruct vertices within within about three
 677 wires, which is quite close to the one-wire-limit on the accuracy of a perfect reconstruction.

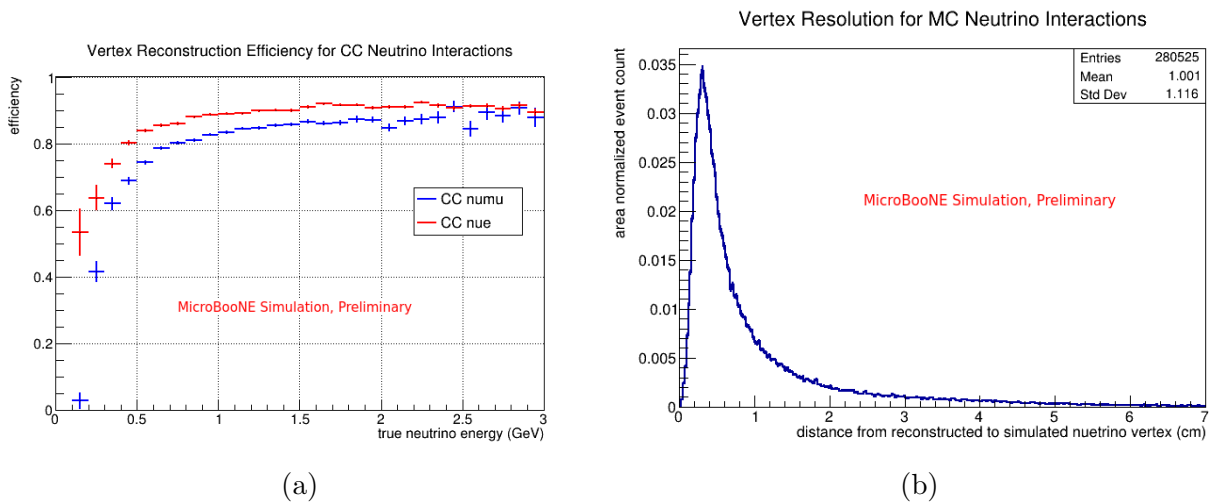


Figure 8: (a): The fraction of MC ν_μ CC and ν_e CC interactions occurring inside the MicroBooNE fiducial volume in which a neutrino candidate vertex was reconstructed (as a function of simulated neutrino energy). (b): The distance between the true and reconstructed neutrino vertex for all MC neutrino interactions inside the MicroBooNE fiducial volume.

679 To determine the quality of reconstructed prongs, we select a sample of tracks and showers
680 attached to reconstructed neutrino vertices from MC neutrino interactions. Prongs are truth-
681 matched to simulated particles from the interaction by projecting all of their spacepoints
682 back into the 2D wire plane images and finding the simulated particle that deposits the
683 most charge in associated 2D pixels. To allow for accurate truth-matching, we require
684 that no more than 20% of the prong's 2D pixel charge come from the overlaid cosmic-ray
685 background data. For each prong, we calculate the reconstruction quality metrics of purity
686 and completeness, where purity is defined as the fraction of the prong's total 2D pixel charge
687 that was produced by the truth-matched simulated particle, and completeness is defined as
688 the fraction of the total 2D pixel charge deposited by the simulated particle that is included
689 in the reconstructed prong.

690 Figure 9 shows plots of purity vs. completeness for prongs that are truth-matched to
691 simulated muons, charged pions, protons, electrons, and photons. The vast majority of
692 reconstructed prongs occupy the high-purity, high-completeness upper-right corner of these
693 plots, indicating a quality reconstruction. However, for protons and, to a greater extent,
694 charged pions, there is a non-trivial population of prongs with high completeness but rela-
695 tively low (roughly 40 - 70%) purity. This is largely due to the difficulty in separating out
696 short tracks from the often dense clusters of charge surrounding the immediate vicinity of
697 interaction vertices. Additionally, charged pions often decay, producing (through an inter-
698 mediate muon) a small electron shower. In these cases, the electron shower and charged
699 pion track are sometimes reconstructed as part of the same prong, contributing to the popu-
700 lation of lower-purity pion prongs. There is also a non-trivial population of electron prongs
701 with high purity, but low completeness. This is caused by either an early, spatially isolated
702 branch of the electron shower getting reconstructed as a separate shower or by the pixels
703 associated with a small stub of the trunk of the electron shower getting tagged as track
704 pixels, causing that stub to get reconstructed as a separate track. However, in these cases,
705 most of the electron shower is almost always reconstructed in a separate prong, and these
706 occasional reconstruction issues can be overcome by identifying such prong fragments by
707 estimating their purity and completeness with the LArPID network (discussed in section
708 III).

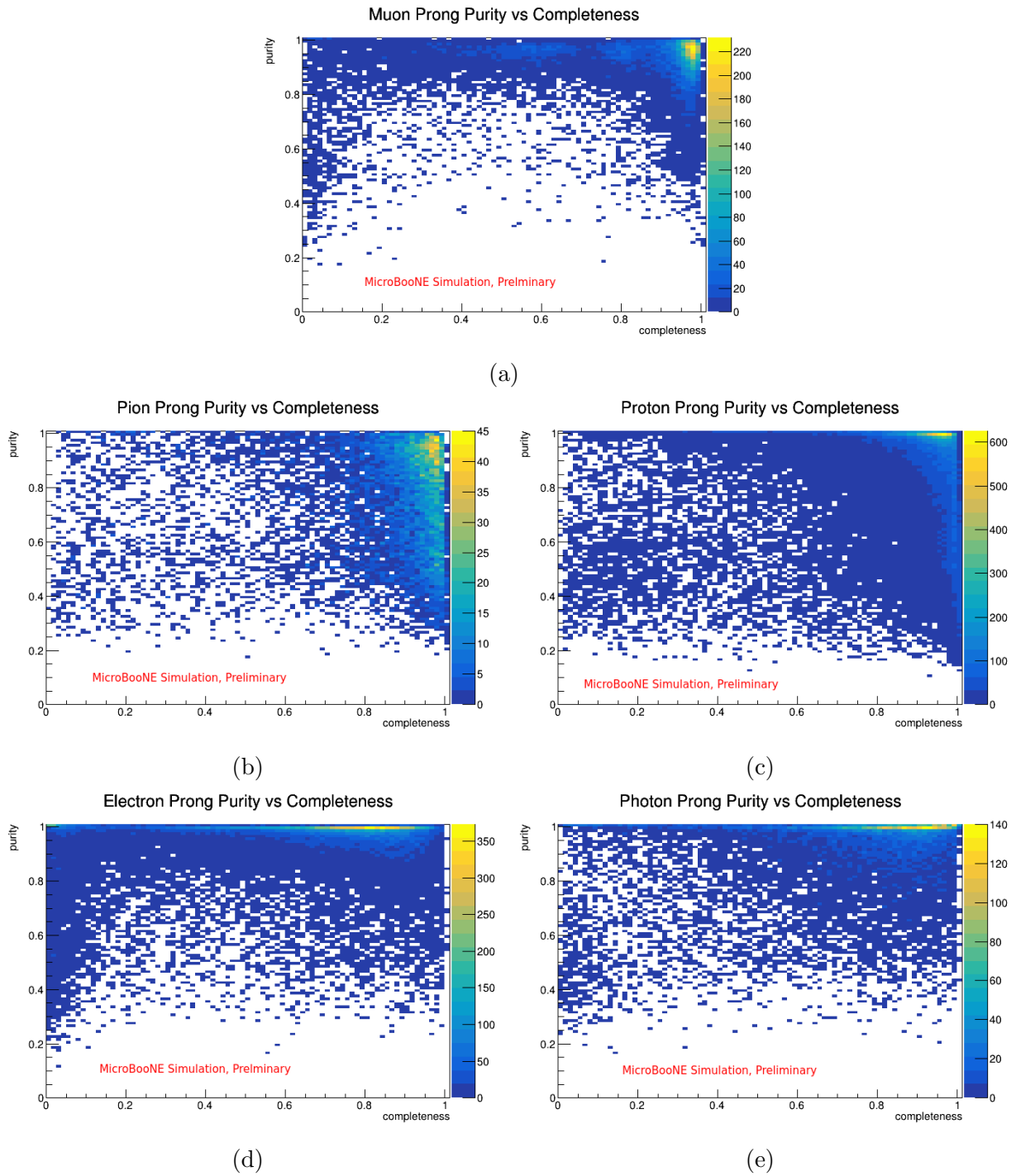


Figure 9: Purity vs. completeness for reconstructed prongs (from MC neutrino interactions occurring inside the MicroBooNE fiducial volume) that are attached to neutrino candidate vertices and truth-matched to simulated muons (a), charged pions (b), protons (c), electrons (d), or photons (e).

709 H. Energy Reconstruction

710 To reconstruct the energy of tracks, we first use the LArPID network discussed in section
711 III to determine the particle type: tracks are classified as either muons, charged pions,
712 or protons based on which of those three LArPID particle scores is highest. Knowing the
713 particle type, we can then use the track length and fits to the kinetic energy vs. range
714 curves of these three particles to determine a kinetic energy for the track. These fits are
715 shown in figure 10 overlaid over a scatter plot of kinetic energy vs. length for simulated
716 muon, charged pion, and proton trajectories (from MicroBooNE MC ν_μ CC interactions)
717 that begin and end at least 10cm from the edge of the MicroBooNE active volume. The fit
718 for muons provides accurate results; however, charged pions and protons often interact before
719 ranging out, causing a spread above the fit line for particles in which our range calculation
720 underestimates energy. This range calculation will also of course underestimate the energy
721 of track-like particles that exit the detector. These shortcomings will be addressed in future
722 studies.

723 Shower energy is reconstructed from the visible charge observed in the collection plane,
724 Q_{sh} , which is linearly related to shower energy. As discussed in more detail in [31], a fit to
725 shower energy vs. Q_{sh} yields the conversion:

$$E[MeV] = (0.0126 \pm 0.0001)Q_{sh}, \quad (4)$$

726 where the error is from statistical uncertainty in simulated events used in the fit.

727 Our neutrino energy estimate is then simply calculated as the sum of the reconstructed
728 track and shower energies for all prongs attached to the reconstructed neutrino interaction
729 vertex. This is a measure of visible energy, not a sophisticated neutrino energy reconstruc-
730 tion. A more accurate energy reconstruction that addresses the limitations of the track
731 energy estimate and includes more sophisticated techniques will be introduced in future
732 works.

733 The accuracy of this visible neutrino energy estimate is illustrated in figure 11, which
734 shows reconstructed vs. true neutrino energy for a sample of MC ν_e CC and ν_μ CC events.
735 Only simulated interactions in which all neutrino final state particles are contained inside
736 the detector and that were reasonably well reconstructed (a neutrino vertex must have been
737 found with an attached prong that contains at least 60% of the primary lepton's deposited

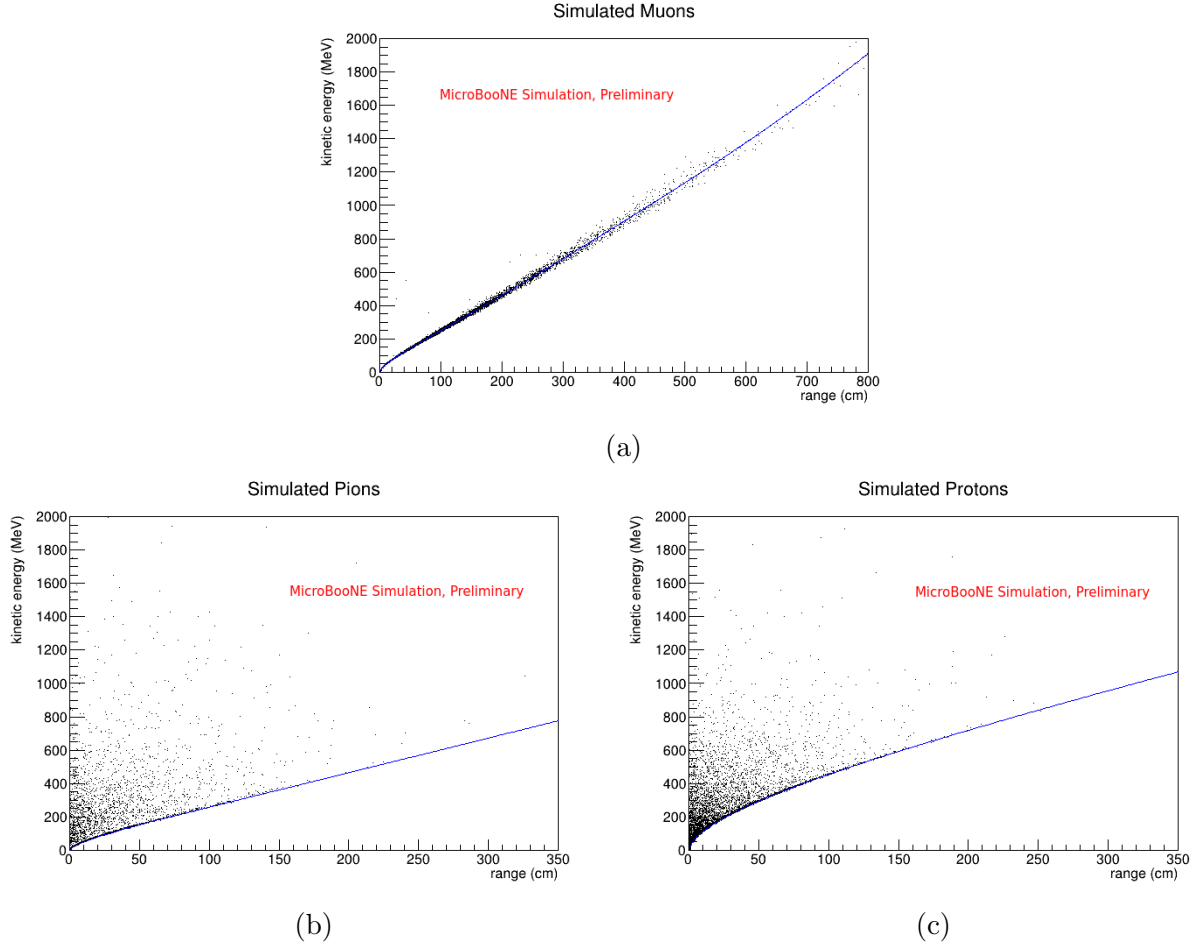


Figure 10: Kinetic energy vs. range for simulated muons (a), charged pions (b), and protons (c) that begin and end in the detector fiducial volume and were produced in MC ν_μ CC interactions. The fits used in track energy reconstruction are shown in blue.

738 charge) are included in these plots². While the majority of events' reconstructed energy falls
 739 below the overlaid one-to-one line and underestimates the true neutrino energy (as expected
 740 for this visible energy calculation), there is a reasonably strong linear relationship.

741 I. LArPID: A Prong Classification CNN

742 To aid in event selections and physics analyses, another CNN, the **L**iquid **A**rgon **P**article
 743 **I**Dentification (LArPID) network, was developed to provide additional information about
 744 reconstructed prongs. CNNs have effectively been used for particle identification in the
 745 past (e.g. in NOvA [32]) and hold particular promise for LArTPCs given their ability to

² Of simulated contained ν_e CC events with a reconstructed vertex, 66% have an attached shower containing at least 60% of the simulated electron's deposited charge. For ν_μ CC events (same conditions), 74% have an attached track with at least 60% of the simulated muon's deposited charge.

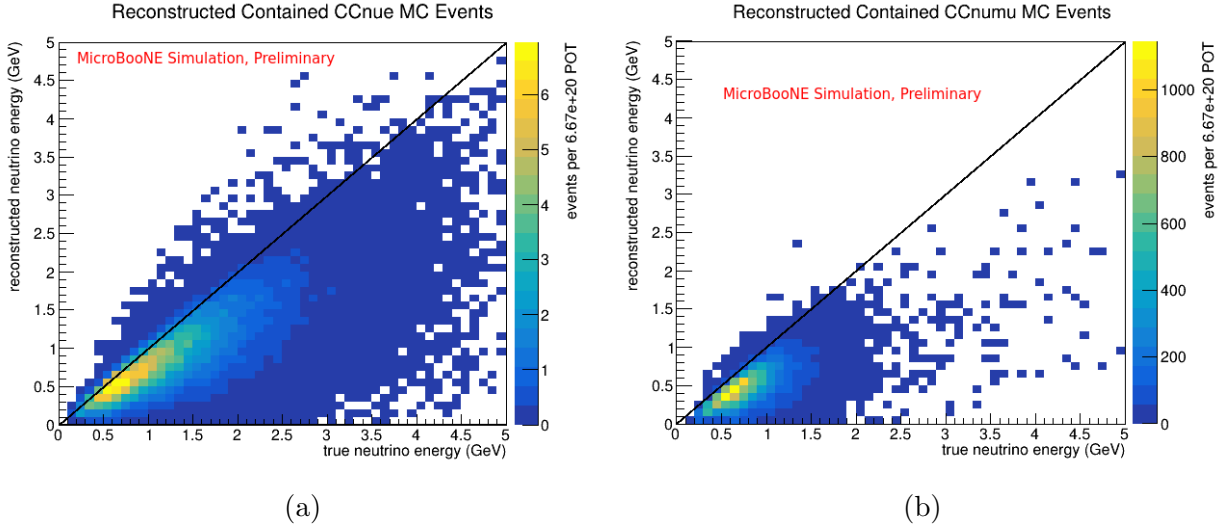


Figure 11: Reconstructed vs. true neutrino energies for MC ν_e CC (a) and ν_μ CC (b) interactions that were successfully reconstructed (a prong from a neutrino candidate vertex was reconstructed with at least 60% of the simulated primary lepton’s deposited charge) and in which all simulated neutrino final state particles are contained (begin and end inside the detector).

746 image neutrino interactions with mm-scale precision. While the primary aim of LArPID is
 747 to perform particle identification, it also predicts the input prong’s production process and
 748 useful reconstruction quality metrics. Specifically, for each input prong, LArPID predicts:

- 749 • Particle type: The network outputs five scores indicating how likely it is that the
 750 prong was produced by a muon, electron, photon, charged pion, or proton. As the
 751 vast majority of charged particles produced in MicroBooNE neutrino interactions are
 752 of one of these types, other very rare particles (e.g. kaon, lambda, or sigma particles)
 753 are ignored. While the prong is assigned the particle type with the highest score,
 754 as we will see in section III A, taking into account all five particle scores is useful in
 755 quantifying how confident we can be with this classification.
- 756 • Production process: The network outputs three scores indicating how likely it is that
 757 the prong represents a primary final state particle produced in the neutrino inter-
 758 action, a secondary particle with a charged parent, or a secondary particle with a
 759 neutral parent. Rather than attempt to classify all common secondary particle pro-
 760 duction processes (Michel decays, delta ray production, pion decay, etc.) these broad
 761 classes were chosen to simplify the prediction while accomplishing its primary aim:
 762 distinguishing primary final state particles from secondaries. The two most general

763 types of observable secondary topology classes - those where the secondary prong does
764 (charged parent) and does not (neutral parent) originate at the end point of another
765 cluster - were chosen to provide additional information about secondaries and aid the
766 network in organizing prongs into general topology classes. This production process
767 prediction provides another valuable tool to aid in interpreting events.

- 768 • Purity: The fraction of visible energy in the prong that was deposited by the true
769 particle. Here, visible energy is calculated as the sum of all pixel values for all 2D
770 wire-plane-image pixels used in the 3D space points that make up the reconstructed
771 prong. As discussed in section III 3, when training the network on Monte Carlo
772 simulation, the labelled truth particle is the simulated particle that deposits the most
773 visible energy in the input reconstructed prong.
- 774 • Completeness: The fraction of all visible energy deposited by the true particle that
775 was reconstructed in the input prong (where visible energy and “true particle” are
776 defined as above for the purity prediction).

777 Analyzing these network outputs for all reconstructed prongs attached to a candidate
778 neutrino interaction vertex provides valuable information about both the prongs and the
779 candidate neutrino interaction. The particle classification outputs not only aid in identi-
780 fying particles and selecting neutrino interactions with desired final states, but could also
781 allow for a more accurate neutrino energy estimate by providing a robust particle hypothesis
782 in e.g. range-based momentum calculations or neural-network based energy estimation tech-
783 niques utilizing high-level reconstruction outputs. In addition to organizing particles into
784 parent/daughter hierarchies for true neutrino interactions, the particle production process
785 can be used to veto mis-reconstructed neutrino interaction vertices placed at the position
786 of e.g. a particle decay. As shown in section III A, it is particularly helpful in CC ν_e event
787 selections as it can veto background events where the candidate primary electron prong is
788 in fact a secondary (for example a charged pion decay product or cosmic Michel electron).
789 And the completeness and purity metrics allow for the identification of poorly reconstructed
790 prongs: prongs reconstructed from energy depositions of a variety of different particles or
791 those representing a fragment of a true particle. These reconstruction quality metrics can be
792 used to better understand reconstructed neutrino interactions and, in the future, to improve

793 the reconstruction as inputs to downstream algorithms or networks that could reorganize
794 clusters into prongs that better represent particle trajectories.

795 The following sections detail this LArPID network’s inputs (section III 1), architecture
796 (section III 2), training details (section III 3), and performance (section III 4). Preliminary
797 studies on interpreting the model are discussed in section III 5.

798 1. *Network Inputs and Image Preprocessing*

799 The LArPID network operates on all three 2D wire-plane images (with tagged cosmic
800 pixels removed) of both the input reconstructed prong and the full event. Going back
801 to the 2D images provides the network with information that may have been lost during
802 reconstruction as a result of dead channels or other errors. For example, in the probable CC
803 ν_e data event shown in figure 12, shower pixels near the interaction vertex are present in the
804 collection plane, but are missing in both the U and V planes. As a result, no 3D space points
805 could be formed near the vertex, and the reconstructed 3D shower prong begins at a distance
806 from the reconstructed neutrino interaction vertex. If considering only the 3D reconstruction
807 outputs, this might indicate that the shower is a photon (which travel a distance from the
808 vertex before pair-converting and depositing energy). However, by operating on the original
809 2D wire-plane inputs, the LArPID network can see the shower extending back to the vertex
810 in the collection plane and classifies this shower as an electron.

811 Including the full-event context images, with all non-cosmic-tagged pixels, provides the
812 network with a wealth of additional information that aids in all the network’s tasks. Seeing
813 the full event improves particle identification accuracy by allowing the network to learn
814 physical features associated with different particle types. For example, photons start at a
815 distance from the interaction vertex, whereas electrons begin depositing energy directly at
816 the vertex. Neutral pions decay into a pair of photons, so the network can learn that when
817 it sees two showers pointing back to the vertex these are likely photons. Preliminary studies
818 indicating that the network indeed picks up on this kind of context information in assigning
819 particles scores are presented in section III 5. The context information is of course also
820 needed to observe parent or fellow neutrino final state particles in distinguishing between
821 primaries and secondaries in the production process classifier. Finally, allowing the network
822 to observe when prong pixels are embedded in a larger cluster or a mix of different clusters

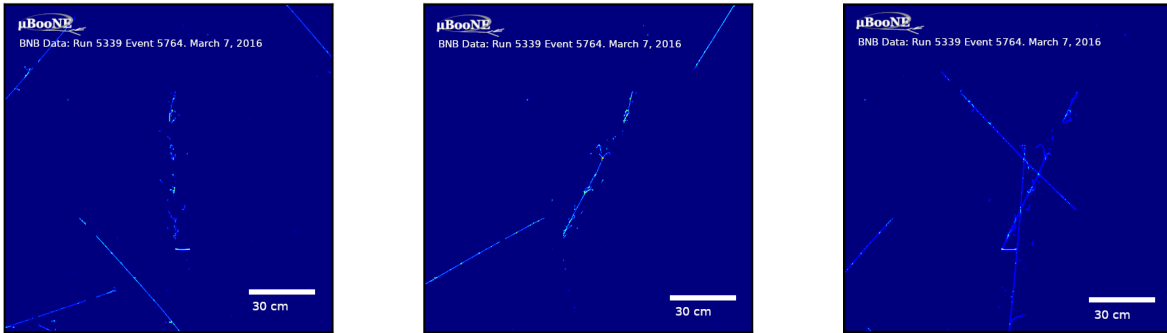
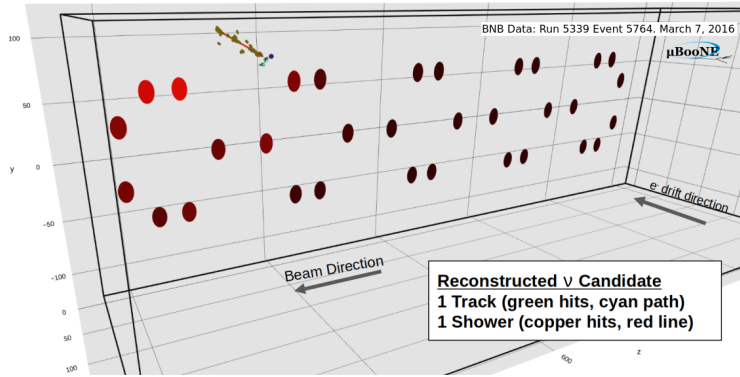


Figure 12: Bottom: zoomed in view of three wire plane images for a probable CC ν_e interaction in a MicroBooNE open dataset. The views are from the U induction plane (left), the V induction plane (center), and the Y collection plane (right). Top: Reconstructed neutrino candidate for the same event with PMT positions recording flashes highlighted (purple: reconstructed neutrino vertex position, copper: 3D space points in reconstructed shower, green: 3D space points in reconstructed track). This event passed our selection even though there is a visible gap in 3D spacepoints between the shower and vertex caused by unresponsive wires in the U and V planes. However, the prong-CNN still designated the shower electron-like likely due to the shower visibly starting from the vertex in the Y plane. This is a candidate example where using the low-level 2D information has helped overcome downstream reconstruction errors.

823 is needed for accurate completeness and purity estimates.

824 The prong and context images passed to the network are processed as follows. To obtain
 825 the prong images, 3D space points in the reconstructed prong are projected back into the 2D
 826 wire-plane images to obtain all associated pixels. To reduce computational requirements,
 827 these images are then cropped to a 512x512 pixel (153.6 x 153.6 cm) window. This window
 828 size is large enough to encompass most charged particles from neutrino interactions in Micro-
 829 BooNE. This crop is performed separately in each wire plane. In a given wire-plane image,
 830 when the full set of prong pixels does fit within this window, the crop is centered around

831 the middle of the prong (the point half-way between the min and max row and column).
832 If the prong pixels do not fit within this window, the crop is centered around the end of
833 the prong for tracks and around the beginning of the prong for showers. This decision was
834 taken as most of the information in distinguishing muon, charged pion, and proton tracks
835 lies at their end (as the particle slows down and potentially decays), whereas the informa-
836 tion needed to distinguish between photon and electron showers lies at the beginning, in
837 the shower trunk. In each wire-plane, the context image is cropped around the same region
838 as the prong image. Before passing these six images (one prong and one context image for
839 all three wire-planes) to the network, pixel values are normalized into the range of roughly
840 -1 to 1 by subtracting the mean and dividing by the standard deviation of all final state
841 particle pixels in a large set of simulated neutrino interactions. An example of the six input
842 images passed to the network for a reconstructed charged pion track from a simulated CC
843 ν_μ interaction is provided in figure 13.

844 2. Network Architecture

845 The LArPID network architecture is illustrated in figure 14. A 34-layer residual network
846 (ResNet34) [24] was chosen for the CNN³. LArPID’s ResNet34 CNN has two input channels
847 for the prong and context image of one wire plane, and it operates separately on each
848 wire plane using shared weights for all three. A 2D adaptive average pooling operation
849 is performed on the output of the final layer, providing 512 learned features for each of
850 the three wire planes. These features are concatenated into a single 1536-length feature
851 vector summarizing information learned about the input prong. This concatenated feature
852 vector is then used as input to four multi-layer perceptrons (MLPs) used to perform the
853 four network tasks. Each MLP has a single hidden layer⁴. The particle classification MLP
854 has a five-neuron output layer, whose logits are passed through a softmax to provide the
855 muon, charged pion, proton, electron and photon scores. The particle production process
856 classification MLP uses a length three output layer and softmax to provide the primary,
857 secondary with charged parent, and secondary with neutral parent scores. The purity and

³ While slightly improved performance might be achieved by using a deeper network, this would have increased the computational complexity and made the network difficult to deploy on cpus as required for large-scale MicroBooNE data processing. An 18 layer ResNet CNN was tested as well, but was found to provide lower performance.

⁴ Increasing the number of hidden layers was found to increase the time it took the model to converge during training without improving performance

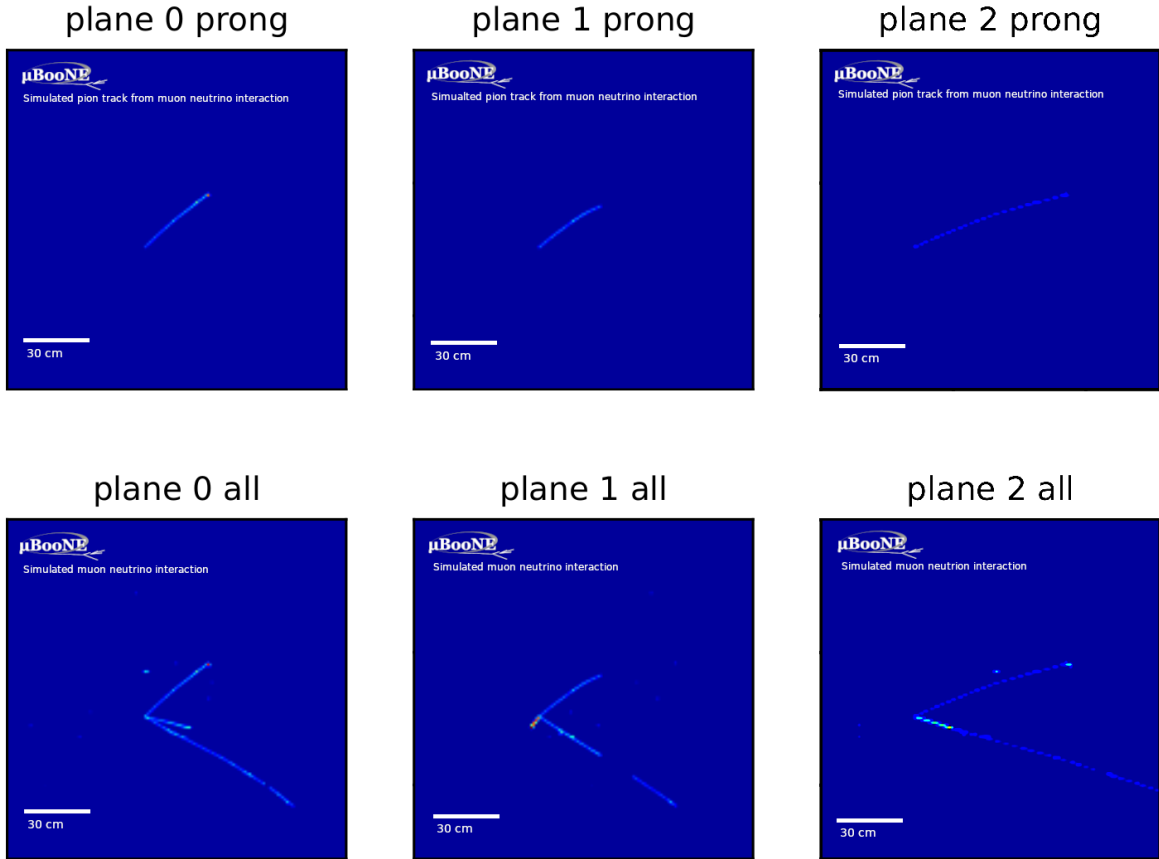


Figure 13: Example LArPID input images for a reconstructed charged pion track from a simulated CC ν_μ interaction. Top row: prong images for all three wire planes. Bottom row: full event context images for all three wire planes

858 completeness regression MLPs use a single-neuron output layer and sigmoid to provide purity
 859 and completeness predictions in the required physical range of 0 to 1.

860 3. Training

861 The LArPID network was trained on a sample of over 652,000 reconstructed prongs from
 862 MicroBooNE neutrino Monte Carlo simulations overlaid over off-beam cosmic-ray back-
 863 ground data [MC citation]. Only prongs attached to reconstructed candidate neutrino in-
 864 teraction vertices were considered. If an event had multiple reconstructed neutrino vertices,
 865 only prongs attached to the vertex with the highest LArMatch neutrino keypoint score were
 866 selected for training. Two additional requirements were imposed on prongs selected for the
 867 training sample:

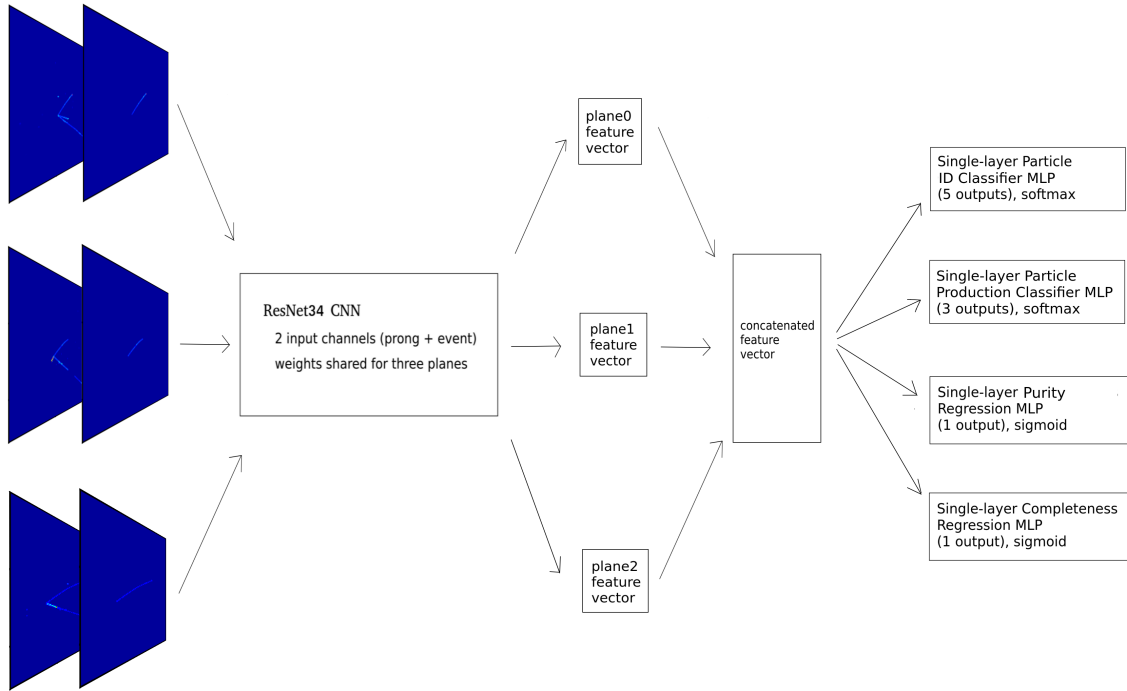


Figure 14: LArPID network architecture with the example inputs from figure 13.

- 868 • Training prongs must have at least 10 above-noise-threshold pixels (which span 3cm
869 in the detector) in all three wire-plane images. Studies were performed to test if
870 increasing this minimum-pixel threshold might improve performance on larger prongs
871 that are primarily considered in neutrino event selections. However, it was found that
872 the network, when trained only on larger (minimum pixel threshold = 90) prongs, did
873 not perform better on a validation set including only such large prongs than when
874 trained on a prong sample including the smallest reconstructed prongs.
- 875 • To allow assignment of truth labels, no more than 20% of charge included in training
876 prongs could come from cosmic-ray contamination.

877 To assign truth labels for training and validation, 3D space points included in recon-
878 structed prongs are projected back into the three wire-plane images to obtain all associated
879 2D pixels. The total amount of charge in all prong pixels that was deposited by each
880 simulated charged particle produced in the neutrino interaction is summed, and the true-
881 particle-type label is assigned as the simulated particle that deposited the most charge. The
882 total charge deposited in the entire detector by this truth-matched simulated particle is also

883 calculated, and the true completeness value is assigned as the fraction of this charge included
 884 in the reconstructed prong. The purity value is assigned as the fraction of all charge in the
 885 reconstructed prong that is contributed by this truth-matched simulated particle. Finally,
 886 the particle production process label is assigned according to how the truth-matched simu-
 887 lated particle was generated. The number of prongs in the training sample truth-matched
 888 to each of the five particle types is shown in table I below.

| muons | charged pions | protons | electrons | photons |
|---------|---------------|---------|-----------|---------|
| 163,987 | 53,871 | 266,653 | 90,940 | 76,915 |

Table I: Number of prongs truth-matched to each of the five particle classes in the LArPID training sample

889 The network was trained over this sample for 20 epochs using a multi-task loss function
 890 with learned weights following the procedure outlined in [33]. A loss must be defined for
 891 each of LArPID’s four tasks (predictions) and combined to form the network’s full loss
 892 function. The relative weight attached to each task-specific loss function can significantly
 893 impact the network’s performance, so the value chosen for these weights is important. The
 894 method employed in [33] treats task weights as learned network parameters that can be
 895 optimized during training. The authors found that this technique can provide superior
 896 performance than even optimal hard-coded weights (e.g. hard-coded values of w_1 and w_2 in
 897 the two-task loss function $\mathcal{L} = w_1\mathcal{L}_1 + w_2\mathcal{L}_2$). We confirmed this in the case of LArPID by
 898 varying hard-coded task weights used in combining task specific loss functions. We found
 899 that the network trained with learned weights outperformed the network trained with any
 900 set of hard-coded weight values. We further found that the network’s particle classification
 901 performance, perhaps the most important network task, was no better when trained only on
 902 that task than when trained on all four tasks using learned task weights. Therefore, using
 903 the technique outlined in [33], the loss function used to train LArPID was defined as:

$$\begin{aligned}
 \mathcal{L} = & e^{-s_{cr}} \mathcal{L}_{MSE}(\hat{y}_{cr}, y_{cr}) + e^{-s_{pr}} \mathcal{L}_{MSE}(\hat{y}_{pr}, y_{pr}) \\
 & + 2e^{-s_{ic}} \mathcal{L}_{CE}(\hat{y}_{ic}, y_{ic}, w_{ic}) + 2e^{-s_{pc}} \mathcal{L}_{CE}(\hat{y}_{pc}, y_{pc}, w_{pc}) \\
 & + s_{cr} + s_{pr} + s_{ic} + s_{pc}
 \end{aligned} \tag{5}$$

904 where \mathcal{L}_{MSE} and \mathcal{L}_{CE} are the mean squared error (for regression tasks) and cross entropy

905 (for classification tasks) loss functions, respectively; y and \hat{y} are the true and predicted
906 network outputs, respectively, for a given input and network task; the s parameters are
907 the learned task-specific loss weights; the subscripts cr , pr , ic , and pc denote quantities
908 for the **completeness regression**, **purity regression**, **particle-identification classification**, and
909 **particle-production-process classification** tasks, respectively; and w_{ic} and w_{pc} are vectors of
910 class weights based on the number of prongs belonging to each particle identification and
911 production process classes, respectively, in the full training sample. These class weights are
912 calculated once upfront and used to weight contributions to the cross entropy loss functions
913 to account for class imbalances. This ensures, for example, that the network doesn't learn
914 to increase the probability of classifying all inputs as protons simply because there are more
915 proton-labelled prongs in the training sample than any other type of particle.

916 Additional training details are as follows:

- 917 • One data augmentation technique was employed to reduce over-fitting: input images
918 were randomly flipped horizontally or vertically, each with a probability of 50%. As
919 demonstrated in figure 15, which shows overall particle classification accuracy for the
920 training sample and an independent validation sample with 50,000 prongs (10,000 per
921 particle type), over-fitting was not a significant issue. Similar few percent differences
922 were observed in the training vs. validation performance of the other network tasks.
923 More details and discussion on network performance in the validation sample are
924 presented in section III 4.
- 925 • The AdamW gradient descent algorithm [34] was used to update network weights.
- 926 • The single-cycle cosine annealing learning rate scheduler shown in figure 16 was used.
927 This type of variable learning rate has been found to reduce the number of training
928 epochs required for convergence [35]. The minimum and maximum learning rate values
929 used in the scheduler were chosen by varying the learning rate in a test training run
930 and determining the range of rate values over which the model continues to converge.
931 A variety of other single-cycle, oscillatory, and stepped learning rate schedulers were
932 tested, but none achieved better performance or faster convergence than the chosen
933 schedule depicted in figure 16.

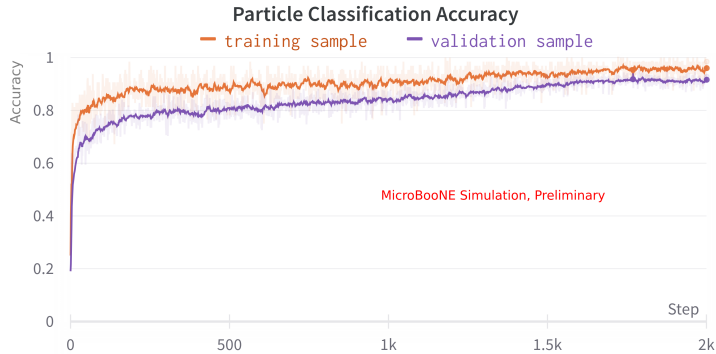


Figure 15: Overall particle classification accuracy for the training sample and an independent validation sample with 50,000 prongs (10,000 per particle type) as a function of training iteration.

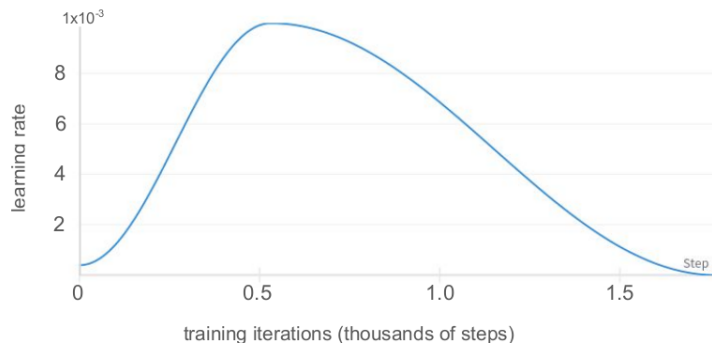


Figure 16: The learning rate scheduler used to train the LArPID network, shown as a function of training iterations. The full schedule lasts for 20 epochs.

934 *4. Network Performance*

935 The performance of the LArPID network was tested on an independent validation sample
 936 of 50,000 reconstructed prongs (10,000 of each particle type: muons, charged pions, protons,
 937 electrons and photons). The same selection criteria detailed in section III 1 used to construct
 938 the training sample were used for this validation sample. For the classification task results,
 939 an additional requirement that at least 60% of the validation prongs' total pixel charge be
 940 contributed by a single simulated particle (true prong purity > 60%) was imposed. This
 941 requirement was placed to ensure sensible truth labels could be assigned.⁵

942 The network achieved an impressive overall validation accuracy of 91.8% on the particle

⁵ A version of the network was also trained with the same true prong purity > 60% requirement, but it was found that this did not improve the network's classification performance on a purity > 60% validation sample. This requirement was therefore not ultimately imposed on the training sample so that the network could be trained to make more accurate purity and completeness predictions in cases where purity < 60%.

943 identification task. A confusion matrix showing the accuracy for each particle type is shown
 944 in table II. The per-particle validation accuracy is very high for all five particle types, and
 945 when the network does mis-classify a prong, it almost always applies the label of a particle
 946 that leaves similar signatures in the detector. For example, mis-classified electrons are almost
 947 always assigned a photon label (and vice versa) and mis-classified charged pions are almost
 948 always assigned a muon label (and vice versa).

| | True e^\pm | True γ | True μ^\pm | True π^\pm | True p |
|----------------------------------|--------------|---------------|----------------|----------------|--------------|
| Fraction classified as e^\pm | 84.5% | 5.2% | 0.1% | 0.5% | 0% |
| Fraction classified as γ | 12.7% | 94.3% | 0.2% | 0.2% | 0.1% |
| Fraction classified as μ^\pm | 0.4% | 0.1% | 93.9% | 11.5% | 0.3% |
| Fraction classified as π^\pm | 2.3% | 0.3% | 5.6% | 86.5% | 1.6% |
| Fraction classified as p | 0.1% | 0.1% | 0.2% | 1.4% | 97.9% |

Table II: A confusion matrix showing LArPID’s particle classification accuracy in the validation sample: the fraction of prongs truth matched to each particle type that LArPID classified as an electron (e^\pm), photon (γ), muon (μ^\pm), charged pion (π^\pm), or proton (p) (columns sum to 100%).

949 The network’s overall validation accuracy on the particle-production-process classification
 950 task was similarly high, at 89.0%. As shown in table III, accuracy is high for all three
 951 production-process classes. Accuracy is highest for identifying secondaries with a neutral
 952 parent, likely as this signature (a prong created with no other tracks or showers originating
 953 at it’s start position) is more unique than the other two classes.

| | True primary | True neutral parent | True charged parent |
|---------------------------------------|--------------|---------------------|---------------------|
| Fraction classified as primary | 87.8% | 3.4% | 6.5% |
| Fraction classified as neutral parent | 2.9% | 93.6% | 6.9% |
| Fraction classified as charged parent | 9.3% | 3.0% | 86.7% |

Table III: A confusion matrix showing LArPID’s particle-production-process classification accuracy in the validation sample: the fraction of prongs with each true production-process class that LArPID classified as a primary neutrino-final-state particle, a secondary with a charged parent, or a secondary with a neutral parent (columns sum to 100%).

954 The validation accuracy of the network’s completeness and purity predictions are illus-
 955 trated in figure 17, which shows 2D histograms of the predicted vs. true reconstruction
 956 quality metrics. For a given range of true completeness or purity values, there is a non-
 957 trivial spread in the predicted values. However, the bulk of the prongs in these heat maps

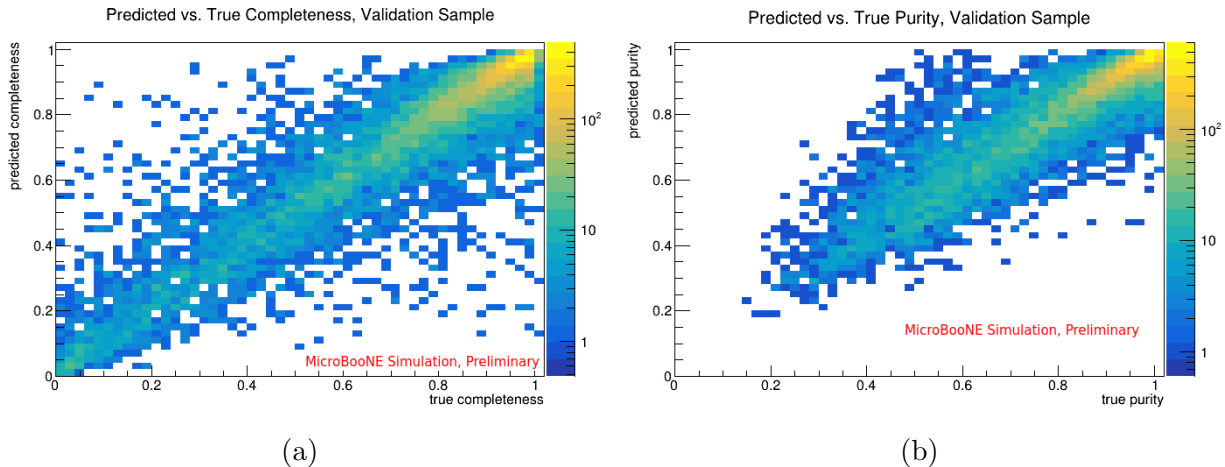


Figure 17: A 2D histogram showing predicted vs. true completeness (a) and purity (b) for prongs in the validation sample.

958 do roughly follow a one-to-one line. So while the exact value of LArPID’s completeness
 959 or purity prediction for a given prong should not be interpreted with extremely high con-
 960 fidence, these predictions are robust in revealing whether the input prong is likely to be a
 961 small fragment of a true particle, a mostly complete reconstruction, or something in between
 962 (completeness) and, similarly, whether it is likely to be reconstructed from a mix of different
 963 particles or mostly from a single particle (purity).

964 5. *Interpreting the Model*

965 Preliminary image manipulation studies were carried out to shed light on what informa-
 966 tion LArPID is using from input images to make its predictions. While clear decision-making
 967 algorithms cannot be extracted from the complex network of neurons in deep learning mod-
 968 els, these interpretability studies can provide valuable insights into how neural networks are
 969 making decisions. The technique employed here involves testing hypotheses on what infor-
 970 mation is being used in the network by providing the model with a set of counter-factual
 971 images. This is done by replacing an input reconstructed prong or a particle from the context
 972 image with another simulated particle and seeing how the network output changes.

973 An example of one such image manipulation study is shown in figure 18. Here, we
 974 checked to see if the network is learning, from examples of π^0 decay photons, that when two
 975 electromagnetic showers’ initial trajectories can be traced back to an intersection (the π^0
 976 decay position) near the interaction vertex, that these showers are likely photons. Figure

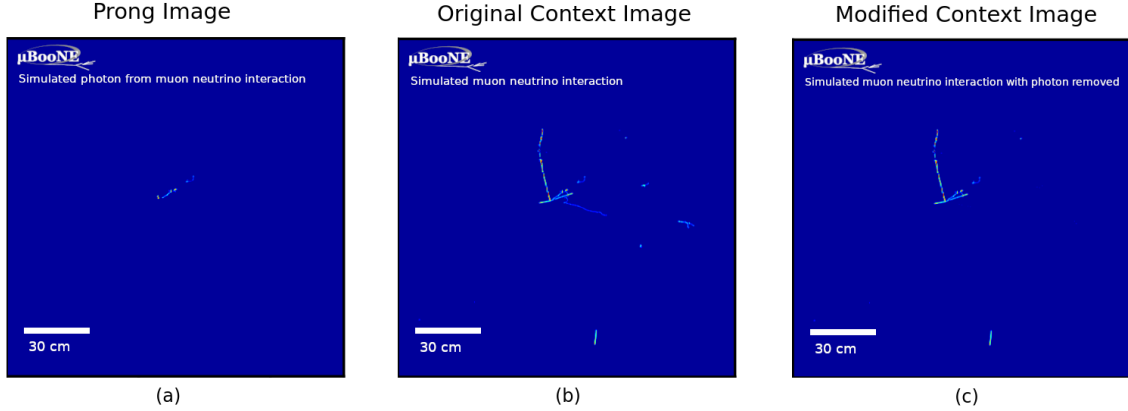


Figure 18: One wire-plane prong image (a) and context image (b) for a reconstructed photon prong produced during a π^0 decay in a simulated CC ν_μ interaction. A modified context image (c) in which the input photon prong’s companion π^0 decay photon is removed. With the original inputs (a and b), LArPID outputs an electron score of 0.027 and photon score of 0.97. With the modified inputs (a and c), LArPID outputs an electron score of 0.21 and photon score of 0.77.

977 18 (a) and (b) show (for one wire-plane) the prong and context images for a reconstructed
 978 photon shower produced during a π^0 decay. The second π^0 decay photon is clearly visible in
 979 the context image. With these inputs, the network confidently and correctly predicted that
 980 the input prong is a photon, with photon and electron scores of 0.97 and 0.027, respectively.
 981 The network was then presented with the same input prong images but modified context
 982 images (figure 18c) that had the second π^0 decay photon removed. With these inputs,
 983 the network’s confidence in its photon prediction decreased significantly, with photon and
 984 electron scores of 0.77 and 0.21, respectively. The same context manipulation had a similar
 985 effect in other examples of input photon prongs from π^0 decays, indicating that the network
 986 has indeed, as expected, learned to increase its photon scores for input showers that are
 987 consistent with π^0 decays.

988 Another set of image manipulations for an example LArPID input is shown in figure 19.
 989 Panels (a) and (b) show (for one wire-plane) input images for a prong (from a simulated CC
 990 ν_μ interaction) that is reconstructed from both a short charged pion track and the electron
 991 shower produced following the pion decay. As the majority of this reconstructed prong
 992 comes from the simulated electron, the network predicts that this prong is an electron, with
 993 electron and charged pion scores of 1 and $2.4 \cdot 10^{-3}$, respectively.

994 We wanted to test how the network’s individual particle scores are impacted when an

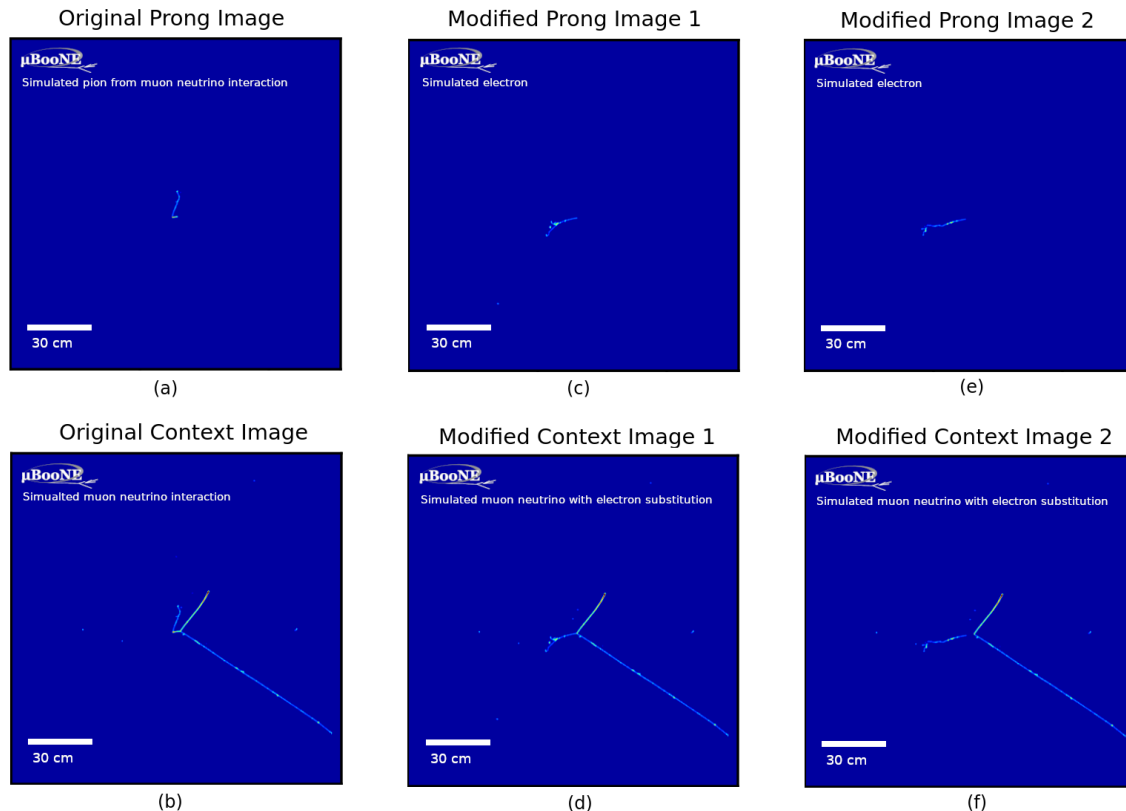


Figure 19: One wire-plane prong image (a) and context image (b) for a prong reconstructed from a charged pion and an electron produced during the pion decay in a simulated CC ν_μ interaction. A modified prong (c) and context image (d) in which the charged pion and its decay electron were replaced by a simulated electron with the same start position and momentum and the original charged pion. A second set of modified prong (e) and context (f) images in which the same substitution was performed with another simulated electron, but the replacement electron was simulated to begin at a short distance from the neutrino interaction position. LArPID’s output electron, photon, and charged pion scores were 1, $8.9 \cdot 10^{-4}$, and $2.4 \cdot 10^{-3}$, respectively, for the original images (a and b); 0.99, $6.5 \cdot 10^{-3}$, and $1.8 \cdot 10^{-4}$, respectively, for the first set of modified images (c and d); and $3.8 \cdot 10^{-4}$, 1, and $2.7 \cdot 10^{-6}$, respectively, for the second set of modified images (e and f).

995 input prong is reconstructed with significant contributions from different particles. In cases
 996 such as these, can information about what combination of particles contribute to a low-purity
 997 prong be gleaned from the individual particle scores? In figure 19 (c) and (d), the input prong
 998 was replaced with a pure simulated electron with the same start position and momentum
 999 as the original charged pion. With these inputs, the network’s pion score decreased to
 1000 $1.8 \cdot 10^{-4}$. A similar set of manipulations on combined charged pion-electron prongs yielded
 1001 similar results, indicating that the charged pion score for classified electron prongs can be
 1002 used to determine if such prongs likely came from a charged pion decay. This feature is

1003 exploited in the CC ν_e selection of section III A to reduce CC ν_μ backgrounds.

1004 An additional set of image manipulations shown in figure 19 verify that the network is
1005 using the context images to learn that showers that start at a distance from an interaction
1006 vertex are more likely to be photons, and those that start at the vertex are more likely to
1007 be electrons. In panels (e) and (f), a similar manipulation is performed in which the input
1008 prong was replaced with a simulated electron, but this time with a start position at a small
1009 distance from the interaction vertex. With these inputs, even though the input is a true
1010 electron, the network confidently classifies it as a photon prong, with photon and electron
1011 scores of 1 and $3.8 \cdot 10^{-4}$, respectively. A similar set of manipulations in which simulated
1012 electrons were placed at a distance from an interaction vertex yielded the same result (a
1013 confident photon prediction), indicating that the network has indeed learned to use this
1014 context information for electron/photon discrimination.

1015 These tests demonstrate the utility of such image manipulation studies in learning how
1016 the network is making decisions. In a future work, these manipulations will be performed
1017 at scale and the results quantified for a more complete set of counterfactuals. This will
1018 improve understanding of the model, increase confidence in its predictions, and inform how
1019 its outputs might more effectively be used in event selections and physics analyses.

1020 III. DEMONSTRATION: SELECTION OF INCLUSIVE ν_e CC AND ν_μ CC INTER- 1021 ACTIONS IN MICROBOONE

1022 A. CC nue inclusive selection cuts

1023 As a demonstration of the effectiveness of these reconstruction tools, we have developed
1024 a set of inclusive CC ν_e selection criteria utilizing the output of the LArMatch and LArPID
1025 networks. As we will show, an effective, high purity and efficiency CC ν_e selection can
1026 be achieved by selecting LArMatch-identified neutrino candidate vertices and filtering out
1027 cosmic and neutrino backgrounds with the Wire-Cell based cosmic tagger discussed in section
1028 II A and cuts on LArPID outputs of attached prongs. For this study, we use off-beam data
1029 to analyze the cosmic-ray background and simulated neutrino interactions overlaid over
1030 cosmic-ray background data for CC ν_e and neutrino background events.

1031 The full set of CC ν_e selection criteria is provided in table IV. We will examine the impact

1032 of adding each selection cut one at a time. With each new cut, we will then discuss the
 1033 motivation for its inclusion, show distributions of the cut variable for signal and background,
 1034 show data/MC comparisons of reconstructed neutrino energy for events passing the new
 1035 selection criteria using a small $4.4 \cdot 10^{19}$ POT MicroBooNE open data sample, and show the
 1036 MC-predicted impact of the new cut on efficiency as a function of true (simulated) neutrino
 1037 energy. A new “cut set” is defined in table IV as a set of selection criteria including a newly
 1038 specified cut along with all previous cuts.

Table IV: Inclusive CC ν_e Selection Cuts

| Cut | Notes |
|---|---|
| LArMatch-identified neutrino candidate vertex found inside the fiducial volume | Added in cut set 1 (included in cut sets 1-6 and final set) |
| 3D space points of prongs attached to neutrino candidate do not all overlap with Wire-Cell-tagged cosmics | Added in cut set 2 (included in cut sets 2-6 and final set) |
| No LArPID-identified muon tracks are attached to neutrino candidate | Added in cut set 3 (included in cut sets 3-6 and final set) |
| At least one LArPID-identified electron shower attached to neutrino candidate | Added in cut set 4 (included in cut sets 4-6 and final set) |
| The largest identified electron was classified by LArPID as a neutrino final state particle | Added in cut set 5 (included in cut sets 5-6 and final set) |
| No tracks attached to neutrino candidate have a high LArPID muon score: $\max \log(\text{muon score}) < -3.7$ | Added in cut set 6 (included in cut set 6 and final set) |
| The largest identified electron was classified by LArPID as an electron with high confidence: $\log(\text{electron score}) - (\log(\text{pion score}) + \log(\text{photon score}))/2 > 7.1$ | Added in final cut set |

1039 The first CC ν_e selection criteria is that a LArMatch-identified neutrino interaction vertex
 1040 was found inside the detector fiducial volume. For our neutrino selections, we define the
 1041 fiducial volume as 3cm from the space-charge corrected TPC boundary as in [17]. Data
 1042 and MC reconstructed neutrino energy distributions with only this requirement are shown
 1043 in figure 20a. The data excess seen here and as additional cuts are applied is not unique
 1044 to our CNN-based reconstruction and selection and has been seen in other frameworks. As
 1045 we will show in section IIID, data and predictions with the full set of selection cuts are
 1046 consistent once accounting for statistical and systematic uncertainties. The MC-predicted
 1047 CC ν_e selection efficiency with just this vertex reconstruction requirement is shown in figure
 1048 20b. Vertex finding has a non-trivial impact on efficiency at low (<500 MeV) neutrino
 1049 energies where electron showers and other prongs are small and more difficult for LArMatch

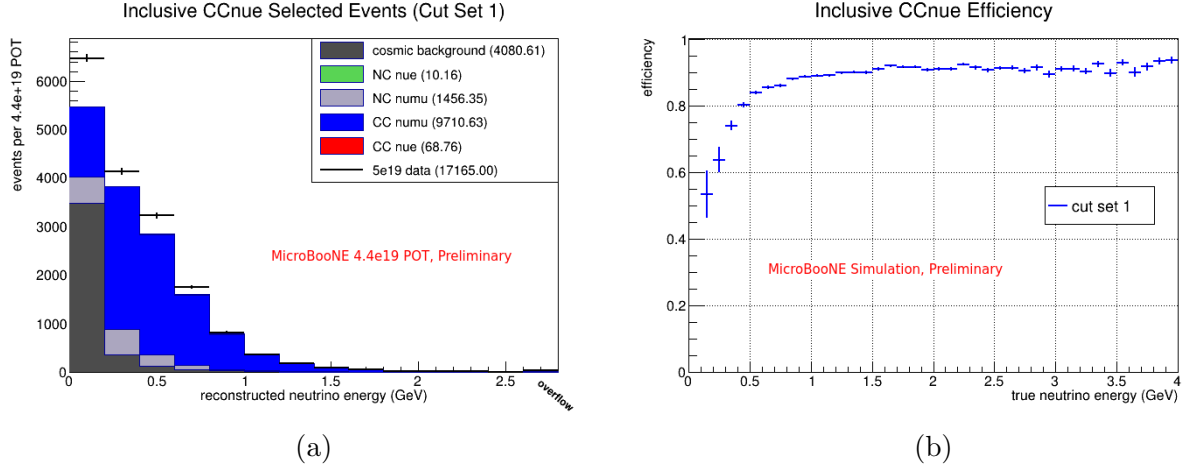


Figure 20: (a): Data/MC reconstructed neutrino energy comparison of events selected by CC ν_e cut set 1 with $4.4 \cdot 10^{19}$ POT of MicroBooNE run1 data. (b): MC-predicted CC ν_e efficiency vs. true neutrino energy with CC ν_e cut set 1. The CC ν_e cut set 1 only contains the requirement that a LArMatch-identified neutrino vertex was reconstructed inside the fiducial volume. Cut sets are defined in table IV.

1050 to identify and separate from cosmic background.

1051 If LArMatch identifies more than one neutrino keypoint cluster in an event, we select the
 1052 one with the highest keypoint score as the candidate neutrino interaction vertex. Further
 1053 selection criteria apply to prongs attached to this candidate interaction vertex.

1054 There is still a significant cosmic-ray background after selecting events with LArMatch-
 1055 identified neutrino candidates. The majority of this background can be removed with the
 1056 Wire-Cell cosmic tagger discussed in section II A. Figure 21a shows neutrino and cosmic
 1057 background distributions for the fraction of 3D points in any cluster attached to the neutrino
 1058 candidate vertex that was tagged as cosmic. Events in the final cosmic-dominated bin with
 1059 100% cosmic overlap (events where all hits in all prongs attached to the vertex have at least
 1060 one constituent pixel that was tagged as cosmic by the Wire-Cell cosmic tagger) are rejected.
 1061 Figure 21b shows the new reconstructed neutrino energy distributions with this requirement
 1062 included (with “cut set 2”). Figure 21c compares the efficiency curve for this “cut set 2”
 1063 to “cut set 1,” which only includes the neutrino vertex reconstruction requirement. This
 1064 cosmic-ray rejection cut does not have a large impact on CC ν_e efficiency.

1065 Further cuts on the LArPID outputs of prongs attached to the candidate neutrino vertex
 1066 can remove almost all of the remaining cosmic and neutrino background. As a first step,
 1067 to remove most of the CC ν_μ background and some of the remaining cosmic background,

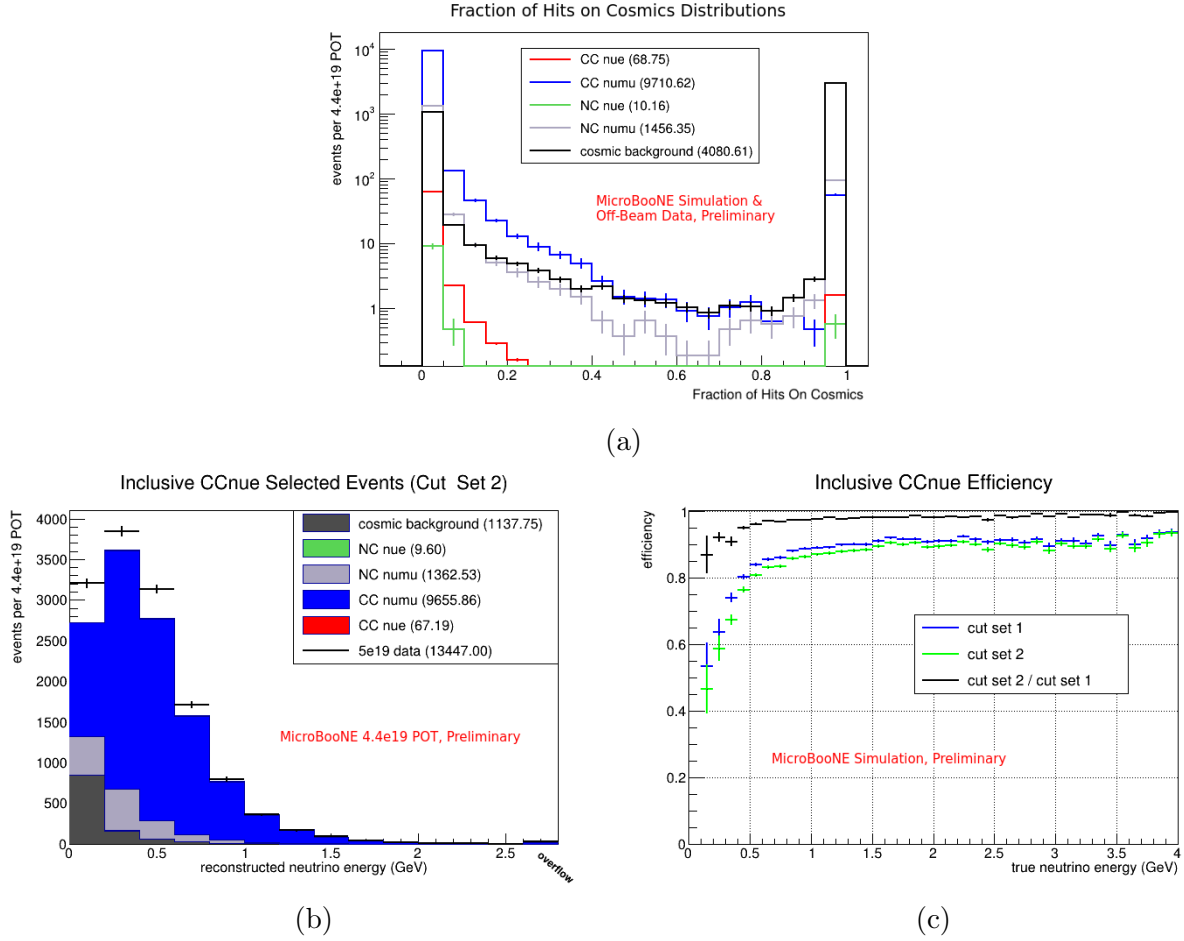
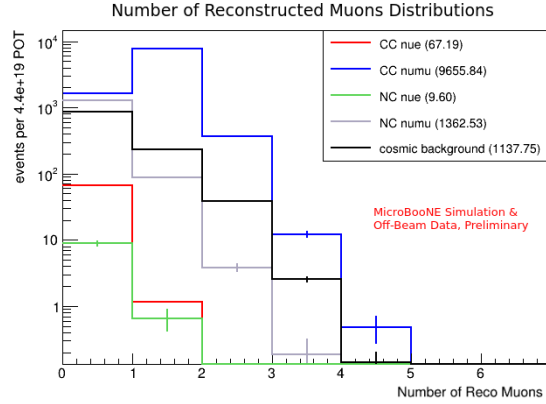


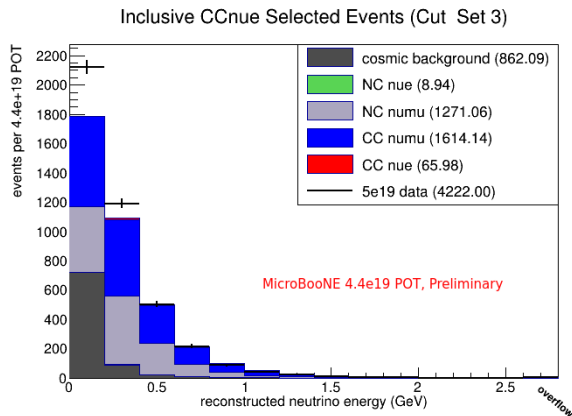
Figure 21: (a): MC and off-beam cosmic background data distributions of the fraction of hits associated with the candidate neutrino vertex that were constructed from pixels tagged as cosmics. Events in the final bin were rejected as the new requirement in CC ν_e cut set 2. (b): Data/MC reconstructed neutrino energy comparison of events selected by CC ν_e cut set 2 with $4.4 \cdot 10^{19}$ POT of MicroBooNE run1 data. (c): MC-predicted CC ν_e efficiency vs. true neutrino energy with CC ν_e cut sets 1 and 2, and the ratio of these two efficiency curves. Cut sets are defined in table IV.

1068 events with identified muons are rejected. Figure 22a compares signal and background
 1069 distributions for the number of reconstructed muons - the number of LArPID identified
 1070 muon tracks attached to the candidate neutrino vertex - in events remaining after applying
 1071 “cut set 2.” The requirement that no reconstructed muons are present in the event was added
 1072 in “cut set 3.” Figure 22 (a) and (b) show the reconstructed neutrino energy distributions
 1073 and efficiency curve comparisons for cut sets 2 and 3. This muon-track rejection cut does
 1074 not have a large impact on efficiency.

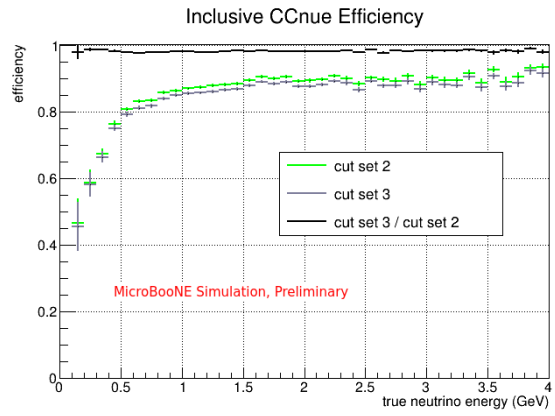
1075 Now that events with identified muons have been removed, we select events with identified



(a)



(b)



(c)

Figure 22: (a): MC and off-beam cosmic background data distributions of the number of LArPID-identified muon tracks (reco muons) attached to the candidate neutrino vertex. The requirement that no reco muons are present was added in CC ν_e cut set 3. (b): Data/MC reconstructed neutrino energy comparison of events selected by CC ν_e cut set 3 with $4.4 \cdot 10^{19}$ POT of MicroBooNE run1 data. (c): MC-predicted CC ν_e efficiency vs. true neutrino energy with CC ν_e cut sets 2 and 3, and the ratio of these two efficiency curves. Cut sets are defined in table IV.

1076 electrons. Figure 23a shows the distribution of the number of LArPID-identified electron
 1077 showers for remaining signal and background events. The requirement that at least one
 1078 electron shower was identified was added in “cut set 4.” This removes the majority of the
 1079 remaining neutrino and cosmic backgrounds, but has a moderate impact on our CC ν_e
 1080 selection efficiency across neutrino energies (see figure 23c). The data/MC reconstructed
 1081 neutrino energy comparison with “cut set 4” is shown in figure 23b.

1082 As can be seen in figure 23a, it is not rare in true CC ν_e events for multiple electron showers
 1083 to be identified. This is generally not due to LArPID incorrectly classifying showers, but

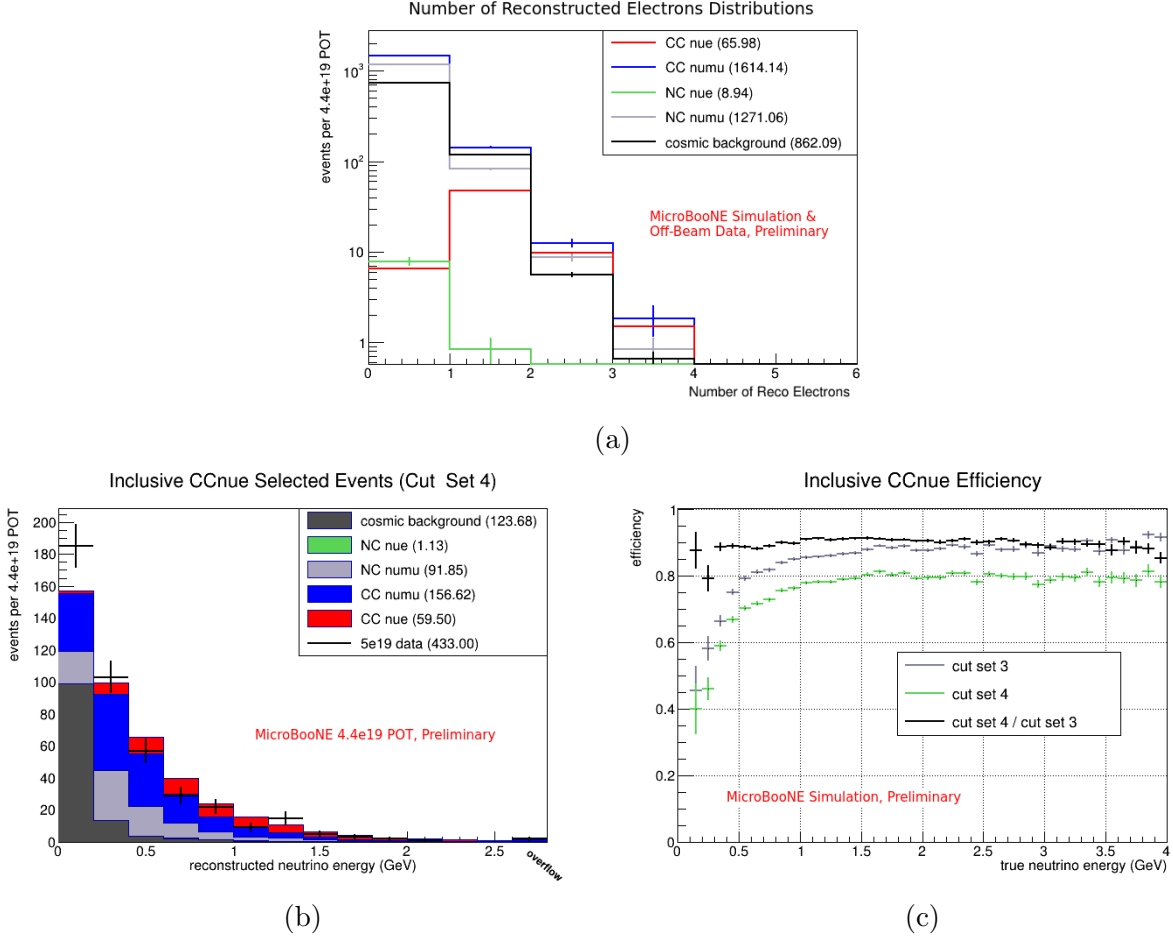


Figure 23: (a): MC and off-beam cosmic background data distributions of the number of LArPID-identified electron showers (reco electrons) attached to the candidate neutrino vertex. The requirement that at least one reco electron is present was added in CC ν_e cut set 4. (b): Data/MC reconstructed neutrino energy comparison of events selected by CC ν_e cut set 4 with $4.4 \cdot 10^{19}$ POT of MicroBooNE run1 data. (c): MC-predicted CC ν_e efficiency vs. true neutrino energy with CC ν_e cut sets 3 and 4, and the ratio of these two efficiency curves. Cut sets are defined in table IV.

1084 clustering errors in which small fragments of the true primary electron are reconstructed as
 1085 a different shower. In these cases, one reconstructed shower tends to carry the majority of
 1086 the true electron's deposited charge. The candidate primary electron is therefore identified
 1087 as the LArMatch-identified electron shower with the most charge.

1088 The majority of the remaining cosmic and neutrino background can be removed by placing
 1089 additional cuts on the LArPID outputs for this candidate primary electron shower. In much
 1090 of the remaining background, a true electron is in fact present, but as a secondary, e.g. a
 1091 Michel electron, delta ray, or an electron produced after a charged pion decay. Figure 24a

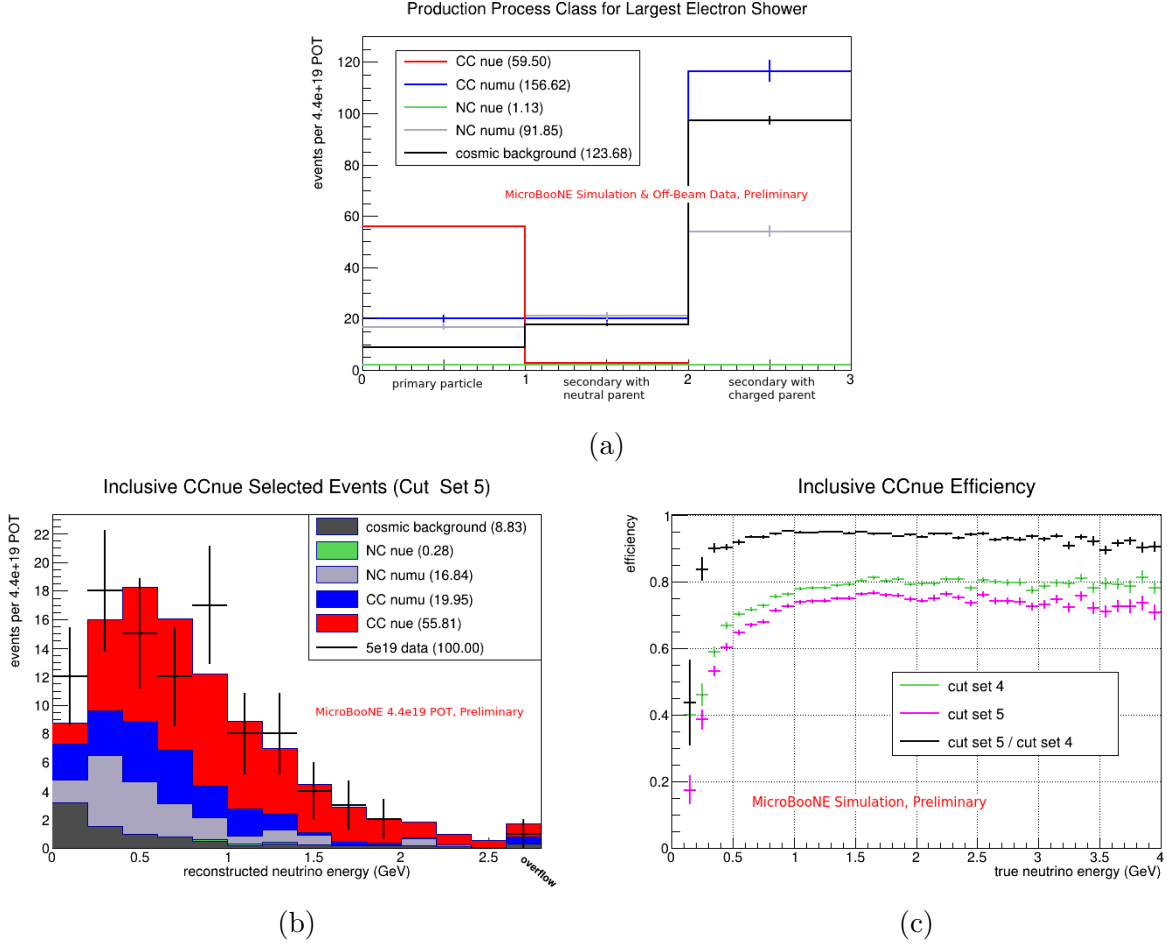


Figure 24: (a): MC and off-beam cosmic background data distributions of the candidate primary electron shower’s LArPID production process class output. The requirement that the candidate primary electron was classified by LArPID as a primary particle was added in CC ν_e cut set 5. (b): Data/MC reconstructed neutrino energy comparison of events selected by CC ν_e cut set 5 with $4.4 \cdot 10^{19}$ POT of MicroBooNE run1 data. (c): MC-predicted CC ν_e efficiency vs. true neutrino energy with CC ν_e cut sets 4 and 5, and the ratio of these two efficiency curves. Cut sets are defined in table IV.

1092 shows the output of the LArPID particle production classifier for the candidate primary
 1093 electron in signal and background events remaining after “cut set 4.” This classifier is able
 1094 to accurately separate out the true primary electron showers from the candidates produced
 1095 in background events, almost all of which are classified as secondaries. The requirement that
 1096 the primary electron candidate was classified by LArPID as a neutrino final state particle
 1097 was therefore added in “cut set 5.” This new requirement has a fairly small impact on CC ν_e
 1098 selection efficiency except at very low (<200 MeV) neutrino energies (see figure 24c). The
 1099 new reconstructed neutrino energy distributions are shown in figure 24b.

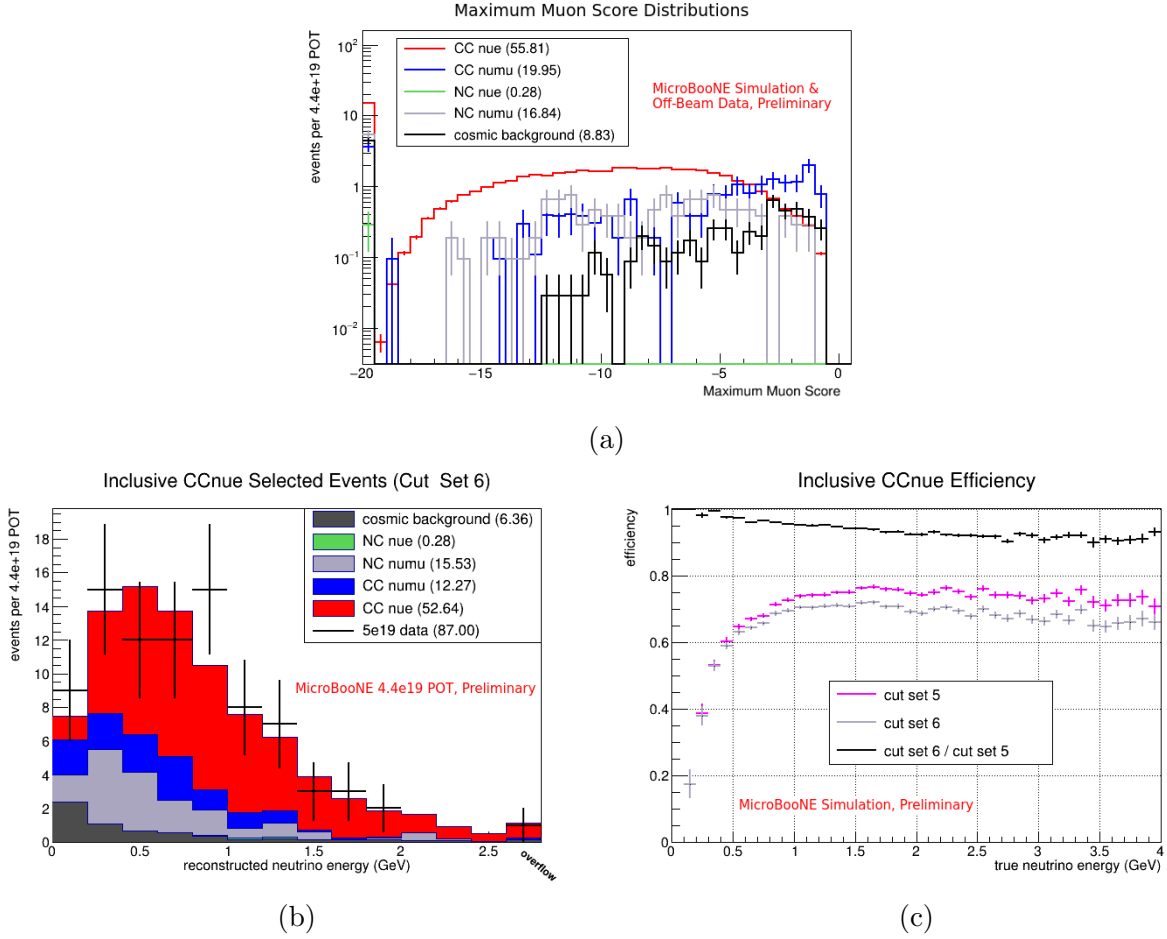


Figure 25: (a): MC and off-beam cosmic background data distributions of the log of the highest LArPID muon score for any track attached to the candidate neutrino vertex. The bin at -20 contains events with no tracks. The requirement that no track have a $\log(\text{muon score})$ above -3.7 was added in CC ν_e cut set 6. (b): Data/MC reconstructed neutrino energy comparison of events selected by CC ν_e cut set 6 with $4.4 \cdot 10^{19}$ POT of MicroBooNE run1 data. (c): MC-predicted CC ν_e efficiency vs. true neutrino energy with CC ν_e cut sets 5 and 6, and the ratio of these two efficiency curves. Cut sets are defined in table IV.

1100 At this stage, much of the remaining background is present due to photons or secondary
 1101 showers being mis-classified as primary electrons or muons being mis-classified as charged
 1102 pions (and therefore not getting rejected by the no reconstructed muons cut). The latter
 1103 issue is addressed first.

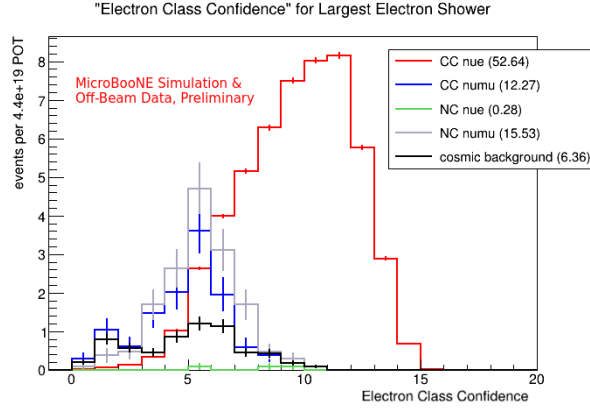
1104 Generally, when muon tracks are mis-classified as charged pions, they still get a fairly
 1105 high LArPID muon score. Events remaining after “cut set 5” with a true muon present can
 1106 therefore be identified by searching for those containing a track with a high muon score (even
 1107 though events with muon-classified tracks have already been removed). Figure 25a shows

1108 the distribution for the log of the maximum LArPID muon score for any track attached
 1109 to the candidate neutrino vertex in remaining events. The cut on this distribution that
 1110 provides the largest CC ν_e selection purity*efficiency product is -3.7. Events with a track
 1111 that has a muon score above this value were therefore removed as the new requirement in
 1112 “cut set 6.” The cut set 6 neutrino energy distributions and efficiency curves are shown in
 1113 figure 25 (b) and (c). This cut does not have a large impact on selection efficiency.

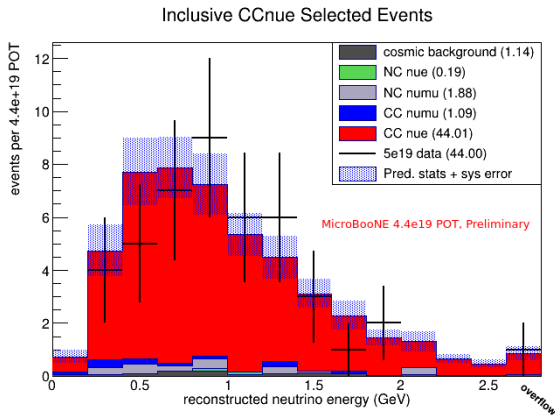
1114 The final cut seeks to remove events where a photon or a mis-reconstructed charged pion
 1115 prong (composed of a charged pion and the electron produced in its decay) was mis-classified
 1116 by LArPID as a primary electron. As with the mis-classified muon tracks, in these cases, the
 1117 network tends to hedge its bets and also give these showers a high photon or charged pion
 1118 score. An electron class confidence metric for the candidate primary electron was therefore
 1119 defined as the difference in its LArPID electron score and the average of its charged pion
 1120 and photon scores: $\log s_e - (\log s_\pi + \log s_\gamma)/2$, where s_e , s_π , and s_γ are the electron, charged
 1121 pion, and photon scores, respectively.⁶ The distribution of the primary electron candidate’s
 1122 class confidence metric for signal and background events remaining after “cut set 6” is shown
 1123 in figure 26a. The signal and background distributions separate out well. The electron class
 1124 confidence cut that maximized the CC ν_e purity*efficiency product, class confidence > 7.1 ,
 1125 was added as the final CC ν_e selection cut. The data and MC reconstructed neutrino energy
 1126 distributions with all selection cuts is shown in figure 26b, which includes a 1σ uncertainty
 1127 band on the predictions including both statistical and systematic (discussed in section III C)
 1128 errors. As we will show in section III D, the data and predictions are consistent within the
 1129 quoted uncertainties. The final selection efficiency is shown in figure 26c along with a
 1130 comparison to “cut set 6.” Adding in the electron class confidence cut does significantly
 1131 impact efficiency, but is necessary to remove remaining backgrounds.

1132 Additional cuts (including utilizing the LArPID completeness, purity, and production
 1133 process score values) were tested, but none outperformed these results. With the cuts
 1134 enumerated in table IV, we are able to achieve a CC ν_e selection with an overall efficiency
 1135 of 56.8% and purity of 91.1%, which is very competitive with PRD 105:112005 [17], the
 1136 highest-efficiency CC ν_e search previously published by MicroBooNE. Additional data/MC
 1137 comparisons (including hand scans of selected data events), performance plots, and a detailed

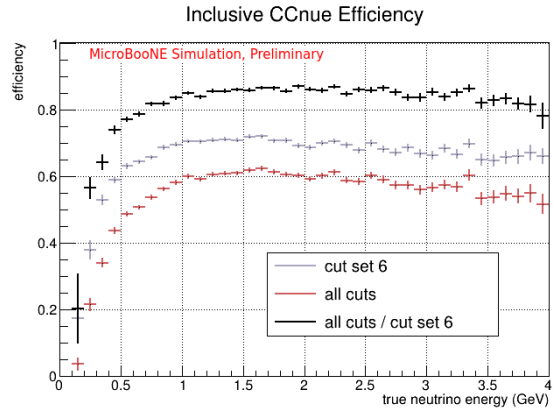
⁶ We also attempted cutting separately on the charged pion and photon scores, but this did not achieve better results.



(a)



(b)



(c)

Figure 26: (a): MC and off-beam cosmic background data distributions of the candidate primary electron shower’s electron class confidence (LArPID electron score minus average of charged pion and photon scores). The requirement that the primary electron candidate have an electron class confidence value above 7.1 was added to the final CC ν_e cut set. (b): Data/MC reconstructed neutrino energy comparison of events selected by the full CC ν_e cut set with $4.4 \cdot 10^{19}$ POT of MicroBooNE run1 data. (c): MC-predicted CC ν_e efficiency vs. true neutrino energy with all CC ν_e cuts and cut set 6, and the ratio of these two efficiency curves. Cut sets are defined in table IV.

1138 comparison of these results with the inclusive CC ν_e selection of PRD 105:112005 are shown
 1139 in section III D.

1140 B. CC numu inclusive selection cuts

1141 Here, we use a similar approach - taking events with LArMatch-identified neutrino vertex
 1142 candidates (selecting the one with the highest score if there are multiple), applying the same
 1143 Wire-Cell cosmic rejection cuts discussed in section III A, and cutting on the LArPID outputs

1144 of attached prongs - to achieve a highly effective inclusive CC ν_μ selection. Figure 22a from
 1145 section III A shows the number of LArPID-identified muon tracks attached to the neutrino
 1146 candidate for MC CC ν_μ events, cosmic, and (in this context) other simulated neutrino
 1147 backgrounds (after applying Wire-Cell cosmic rejection cuts). A CC ν_μ dominated sample
 1148 can be selected by simply requiring that there be at least one identified muon track attached
 1149 to the LArMatch neutrino candidate vertex. (Note that figures 22b and 22c show results
 1150 with the CC ν_e requirement of 0 reconstructed muons, not the ≥ 1 condition discussed
 1151 here for the CC ν_μ selection.) When there are multiple reconstructed muons in true CC ν_μ
 1152 events, this is generally because of clustering errors in which a small section of the track
 1153 is reconstructed as a separate cluster. In these cases, according to MC, the track with the
 1154 highest LArPID muon score is truth-matched to the simulated muon 96.4% of the time, and
 1155 the identified muon track with the most charge is matched to the true muon 95.7% of the
 1156 time.

1157 This simple selection yields a predicted overall CC ν_μ purity of 96.0% and efficiency of
 1158 67.9%. While significant improvements were not achieved by applying further cuts on the
 1159 LArPID outputs of the identified primary muon track or other attached prongs, we found
 1160 that purity can be increased (at the expense of efficiency) by cutting on the neutrino keypoint
 1161 score of the candidate neutrino vertex, the angle of the muon track (to remove downwards
 1162 going cosmic-background muons), and the LArPID production process scores of the muon
 1163 track.

1164 The full set of CC ν_μ selection criteria are enumerated in table V. The predicted selection
 1165 efficiency as a function of true neutrino energy after applying each cut is shown in figure 27b.
 1166 As with the CC ν_e selection, the largest impact on efficiency comes from the neutrino vertex
 1167 reconstruction and the primary lepton identification. Distributions of reconstructed neutrino
 1168 energy for data and MC (including the 1σ uncertainty band calculated in section III C) with
 1169 the full selection are shown in figure 27a. The overall data excess seen here is not unique
 1170 to our CNN-based reconstruction and is consistent with the excess seen in the inclusive
 1171 CC ν_μ selection of MicroBooNE's Wire-Cell reconstruction [17]. Furthermore, as we will
 1172 show in section III D, the data and predictions are consistent within quoted uncertainties.
 1173 Additional data/MC comparisons and a more detailed comparison to the Wire-Cell CC ν_μ
 1174 selection are presented in section III D as well.

Table V: Inclusive CC ν_μ Selection Cuts

| Cut | Notes |
|---|--|
| LArMatch-identified neutrino candidate vertex found inside the fiducial volume | Added in cut set 1 (included in all cut sets) |
| 3D space points of prongs attached to neutrino candidate do not all overlap with Wire-Cell-tagged cosmics | Added in cut set 2 (included in final set as well) |
| At least one track attached to the candidate neutrino vertex was identified by LArPID as a muon | Added in final cut set |

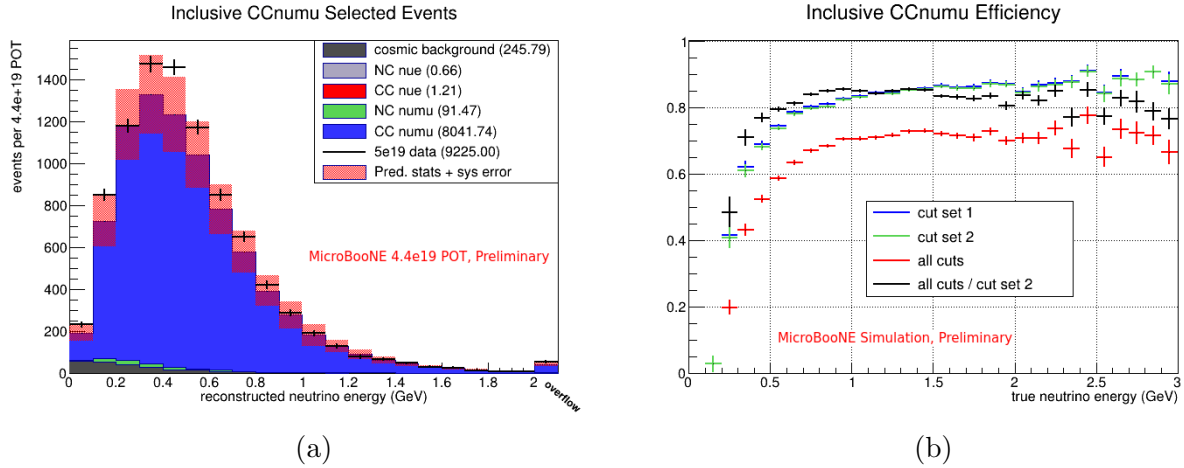


Figure 27: (a): Data/MC reconstructed neutrino energy comparison of events selected by the full CC ν_μ cut set with $4.4 \cdot 10^{19}$ POT of MicroBooNE run1 data. (b): MC-predicted CC ν_μ efficiency vs. true neutrino energy after adding each CC ν_μ cut, along with a ratio of the full cut set and cut set 2 efficiency curves. Cut sets are defined in table V.

1175 C. Systematic uncertainty estimates

1176 Modeling uncertainties that contribute to our systematic errors come from four main
 1177 sources: modeling of the neutrino flux, modeling of the MicroBooNE detector, modeling
 1178 of neutrino-argon cross sections, and modeling of hadron-argon cross sections. To account
 1179 for detector systematics, we modify a variety of detector parameters, re-simulate a neutrino
 1180 sample for each variation, and analyze their impact on our predictions. This is discussed
 1181 in more detail in section III C 1. While these detector variations can change observables
 1182 in any event, variations in the parameters associated with the other sources of systematic
 1183 uncertainty simply alter the rate at which different events occur. These flux and cross section
 1184 uncertainties can therefore be studied by re-weighting individual events without the need to
 1185 re-simulate new neutrino samples. This method and our flux and cross section systematics

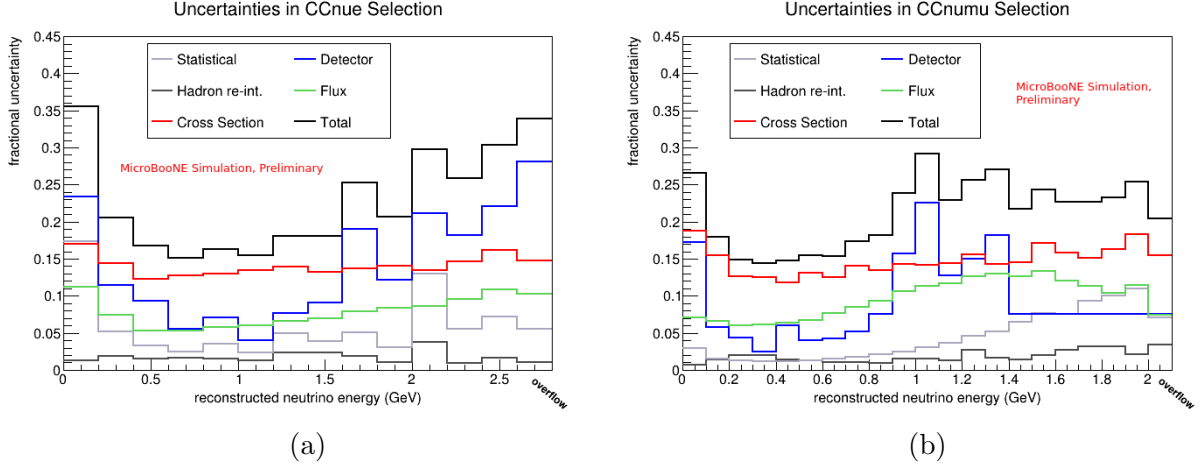


Figure 28: Fractional uncertainties in each reconstructed neutrino energy bin for the inclusive (a) CC ν_e selection and (b) CC ν_μ selection. Statistical uncertainties on the cosmic background + neutrino predictions; systematic uncertainties from our modeling of the detector, flux, neutrino-argon cross sections, and hadron-argon interactions; and the total combined uncertainty is shown. The use of a flat detector systematic uncertainty in the CC ν_μ selection above 1.4 GeV is discussed in section III C 1.

1186 are discussed in more detail in section III C 2.

1187 The results of those studies is summarized in figure 28, which shows uncertainties in our
 1188 predicted event counts in each reconstructed neutrino energy bin used in the inclusive CC ν_e
 1189 and CC ν_μ selections. Our total uncertainty in each bin is shown, along with contributions
 1190 from the four sources of systematic uncertainty discussed above and statistical errors from
 1191 our finite cosmic background and simulated neutrino samples.

1192 1. Detector Systematic Uncertainties

1193 To account for uncertainties in detector modeling, we vary parameters associated with the
 1194 light yield (LY), light attenuation, and Rayleigh scattering length; “wiremod” modifications
 1195 to the amplitudes and widths of wire waveforms as a function of x position, (y, z) position,
 1196 and angles θ_{xx} and θ_{yz} of particle trajectories; a variation in electron-ion recombination
 1197 parameters (“recomb2”); and an alternative electric field inside the TPC from the space
 1198 charge effect (SCE). See e.g. [14] for additional information on these variations.

1199 For each variation, we re-simulate the same sample of Monte Carlo neutrino events and
 1200 calculate a covariance matrix for each kinematic observable to quantify the bin-by-bin shift
 1201 in event counts: $F_{ij}^k = (N_i^k - N_i^{CV})(N_j^k - N_j^{CV}) / (N_i^{CV} N_j^{CV})$, where F^k is the fractional

1202 covariance matrix for the k th variation, N_i^k is the number of events in bin i of the simulation
 1203 with variation k , and N_i^{CV} is the number of events in bin i for the central value simulation
 1204 with default detector parameters. Overall 1σ detector-related fractional uncertainties in
 1205 each bin are then given by $\sigma_i/N_i = \sqrt{\sum_k F_{ii}^k}$.

1206 The computational expense associated with re-simulating neutrino events for each vari-
 1207 ation presents a significant challenge in quantifying these detector systematics. The $O(10^5)$
 1208 event samples used in this analysis provided inadequate statistics to provide a robust esti-
 1209 mate of detector uncertainties in certain regions. For each variation, two simulations were
 1210 combined to predict event counts: one ν_μ dominated sample in which neutrinos are simulated
 1211 in the same proportion estimated to occur in the beam, and one involving only the intrinsic
 1212 CC ν_e component. While the intrinsic ν_e simulation provided adequate statistics for CC ν_e
 1213 predictions, roughly just 10 raw neutral current and ν_μ background events (there are small
 1214 variations between the different simulated samples) from the former beam simulation passed
 1215 our CC ν_e selection. Statistical variations from this background prediction therefore caused
 1216 large artificial fluctuations in our estimated detector systematic uncertainties. In the CC ν_μ
 1217 selection, statistics are also very low in the high energy tails of the reconstructed neutrino
 1218 energy and muon momentum distributions (see figure 29), again causing large fluctuations
 1219 in estimated systematics in those regions.

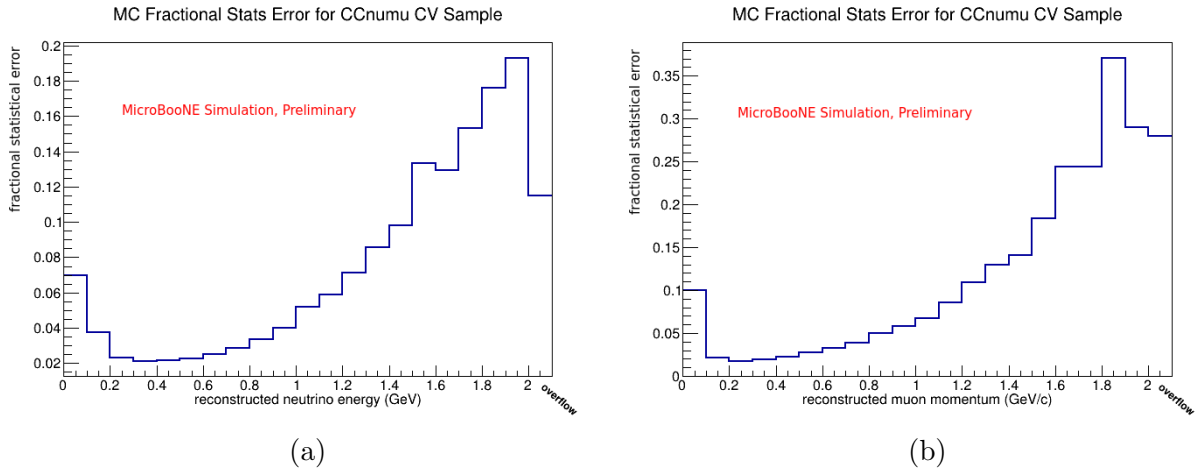


Figure 29: Monte Carlo statistical errors on events passing the CC ν_μ selection for the central value simulation used to estimate detector systematics, binned in reconstructed neutrino energy (a) and muon momentum (b).

1220 We will address these statistical shortcomings prior to publishing these results by re-
 1221 processing one-order-of-magnitude larger samples for these detector variations. As a tem-

1222 porary solution, we place a lower bound on our detector systematics with the following
 1223 corrections. For the CC ν_μ selection, we combine events above 1.4 GeV in reconstructed
 1224 neutrino energy and above 1.2 GeV/c in reconstructed muon momentum into a single bin for
 1225 those respective distributions. When calculating our total uncertainty in bins above those
 1226 thresholds (as in figure 28b), we use the flat high energy/momentum detector systematics
 1227 obtained with this approach. For the CC ν_e selection, we assume that the kinematic de-
 1228 pendence of $N_i^k - N_i^{CV}$, the central value vs. detector variation excess in each bin of all
 1229 kinematic distributions, is the same for the NC and ν_μ backgrounds that pass the selection
 1230 as it is for the CC ν_e signal events that pass the selection. With this assumption, we estimate
 1231 the predicted signal + background event counts by scaling the CC ν_e signal distributions by
 1232 $(N_s + N_b)/N_s$, where N_s and N_b are the total number of signal and background events that
 1233 pass the selection, respectively.

1234 Our total detector systematic uncertainties in each reconstructed neutrino energy bin of
 1235 the inclusive CC ν_e and CC ν_μ selections with and without the low-statistics corrections
 1236 discussed above is shown in figure 30. The uncertainties without the corrections provide a
 1237 lower bound for our estimated detector-related modeling errors, while the larger, statistical-
 1238 fluctuation-driven uncertainties without the corrections provide an upper bound. To avoid
 1239 inflating our detector systematics as a result of low-statistics fluctuations and provide a
 1240 more strict test on data / Monte Carlo consistency in our selection results (discussed in
 1241 section III D), we use the lower-bound detector uncertainties with the statistical corrections
 1242 discussed above. The full fractional covariance matrix (binned in reconstructed neutrino
 1243 energy) for all detector variations with these low-statistics corrections is shown in figure 31.

1244 2. Flux, Cross Section, and Hadron Re-Interaction Uncertainties

1245 To calculate systematic uncertainties arising from flux, neutrino cross section, and hadron
 1246 re-interaction predictions we employ the same method outlined in [14]. Flux uncertainties
 1247 arise from three main sources: the properties of the magnetic focusing horn, hadron produc-
 1248 tion in the target, and secondary hadron interactions. Neutrino cross-section uncertainties
 1249 arise from a large number of parameters associated with each neutrino interaction mode
 1250 and final state interactions that affect all modes. The hadron re-interaction uncertainty
 1251 calculations consider variations in parameters associated with hadron-argon cross sections

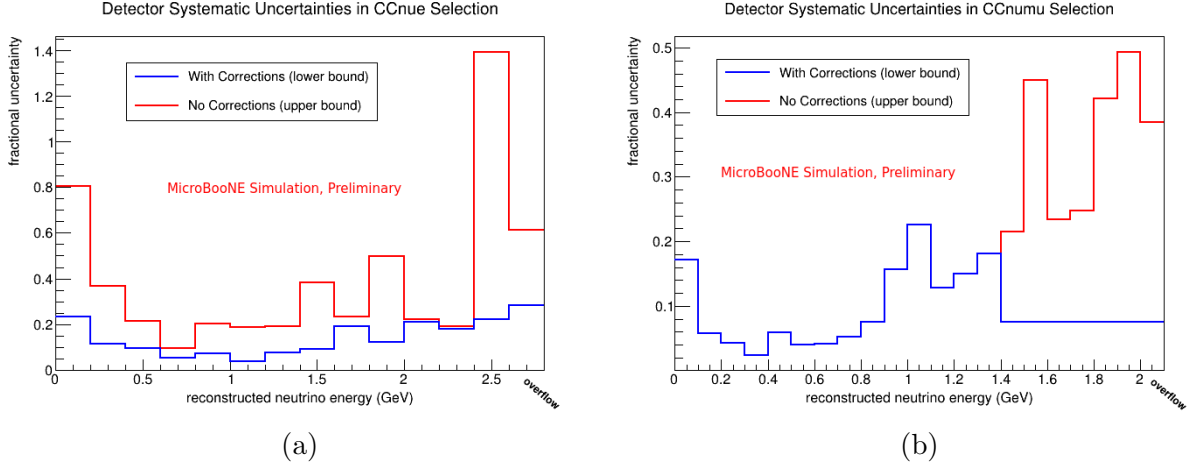


Figure 30: Total detector variation uncertainties in each reconstructed neutrino energy bin of the inclusive (a) CC ν_e and (b) CC ν_μ selections. Results are shown with and without the low-statistics corrections discussed in the text.

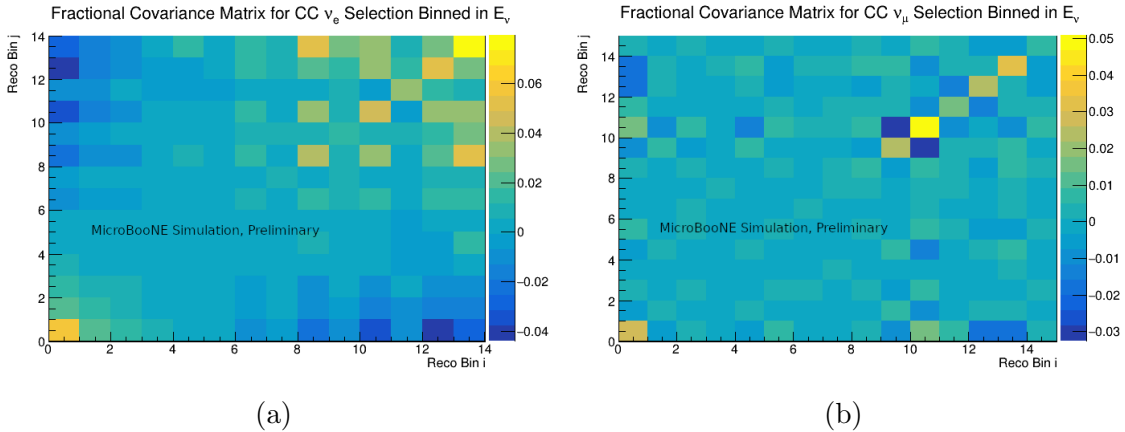


Figure 31: Fractional covariance matrices binned in reconstructed neutrino energy from all detector variations for the inclusive (a) CC ν_e and (b) CC ν_μ selections.

1252 for protons and charged pions. These uncertainties are accounted for by re-weighting events
 1253 with each systematic parameter variation and comparing the modified reconstructed spectra
 1254 with the nominal simulation. Additional details on the variations considered are provided
 1255 in [14].

1256 Given the reconstructed spectra with bin counts N_i for each set of varied parameters, a
 1257 covariance matrix M can be constructed where the variance in bin counts (resulting from
 1258 the parameter variations) is provided in the diagonal entries and the covariance between the
 1259 counts in each pair of bins in the off-diagonal entries. The fractional covariance matrices
 1260 $F_{ij} = M_{ij}/(N_i N_j)$ including all flux, cross section, and hadron re-interaction variations for

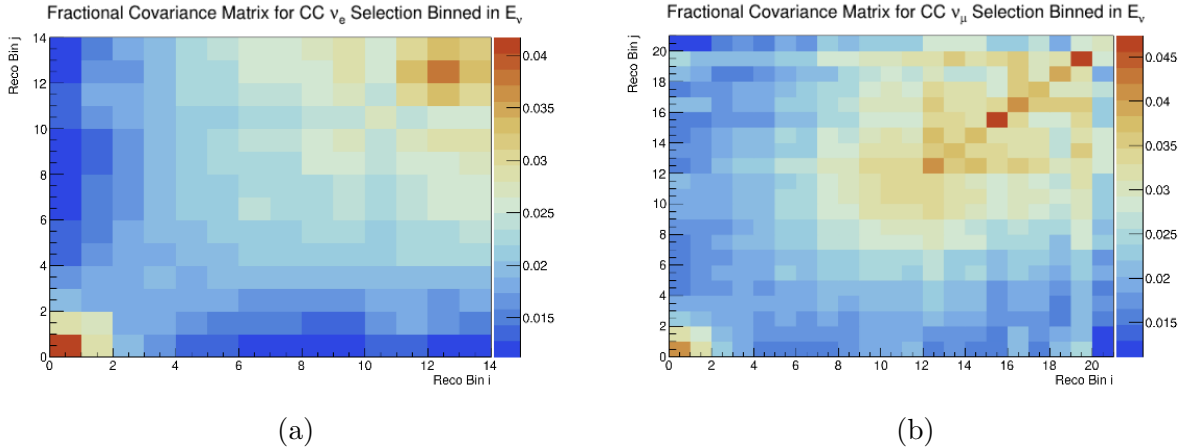


Figure 32: Fractional covariance matrices binned in reconstructed neutrino energy from all flux, cross section, and hadron re-interaction variations for the inclusive (a) CC ν_e and (b) CC ν_μ selections.

1261 the reconstructed neutrino energy spectra in the inclusive CC ν_e and CC ν_μ selections are
 1262 shown in figure 32.

1263 As shown in figure 28, cross section uncertainties provide the largest contribution to our
 1264 model-based systematics. Flux uncertainties are substantial as well; they are roughly half
 1265 the size of cross section uncertainties at lower energies and larger at higher energies. Hadron
 1266 re-interaction systematics contribute very little to our overall uncertainty.

1267 D. Results

1268 The performance of the inclusive CC ν_e and CC ν_μ selections demonstrate the effec-
 1269 tiveness of this new CNN-based reconstruction. Our predicted selection efficiencies and
 1270 purities outperform PRD 105:112005 [17], the highest-efficiency result previously published
 1271 by MicroBooNE. This comparison is shown in table VI.

1272 For the inclusive CC ν_e selection, our deep-learning based reconstruction provides signif-
 1273 icantly higher predicted purities (91% compared to 82%) and efficiencies (57% compared to
 1274 46%). This amounts to a predicted 24% increase in the number of CC ν_e events selected
 1275 with significantly lower background. As shown in figure 33a, an improvement in efficiency is
 1276 achieved across all true neutrino energies (except in the lowest 100-200 MeV bin, in which
 1277 there is no statistically significant difference). For the inclusive CC ν_μ selection, we achieve
 1278 the same overall efficiency as PRD 105:112005 but with a reduced background (purity of

1279 96% compared to 92% from PRD 105:112005). However, as shown in figure 33b, the two
 1280 analyses provide different efficiencies at different neutrino energies, with our reconstruction
 1281 yielding a higher efficiency below 1 GeV and the analysis of PRD 105:112005 providing a
 1282 higher efficiency above 1.5 GeV.

| | DL Reco | PRD 105:112005 |
|-----------------------------------|---------|----------------|
| CC ν_e Selection Efficiency | 57% | 46% |
| CC ν_e Selection Purity | 91% | 82% |
| CC ν_μ Selection Efficiency | 68% | 68% |
| CC ν_μ Selection Purity | 96% | 92% |

Table VI: Inclusive CC ν_e and CC ν_μ selection results for our deep-learning-based reconstruction and PRD 105:112005 [17].

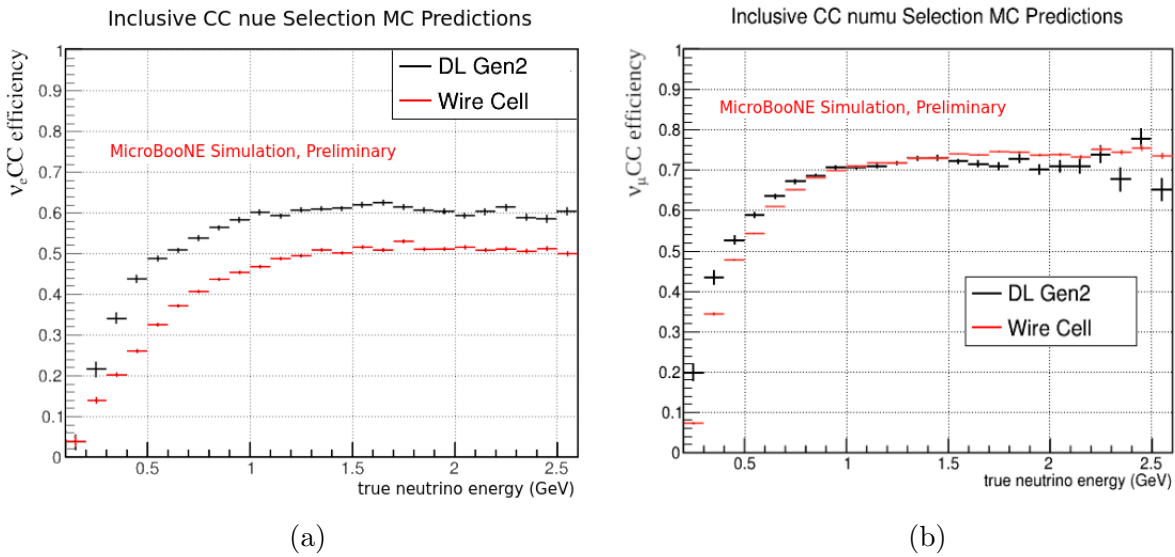


Figure 33: The predicted CC ν_e (a) and CC ν_μ (b) selection efficiency of our reconstruction and selection (DL Gen2) and that of PRD 105:112005 (Wire-Cell) [17] as a function of true neutrino energy.

1283 In sections III A and III B, we showed predicted (using MC neutrino simulations plus
 1284 data cosmic-ray background) and MicroBooNE open data distributions of reconstructed
 1285 neutrino energy for selected inclusive CC ν_e and CC ν_μ events. Figures 34 and 35 show
 1286 the same data/MC comparisons for reconstructed primary lepton momentum and $\cos(\theta_l)$
 1287 (where θ_l is the angle between the primary lepton and the beam). Also included are the
 1288 reconstructed neutrino energy distributions, along with predicted purity and efficiency as
 1289 a function of reconstructed neutrino energies. For both selections, purities are high for all

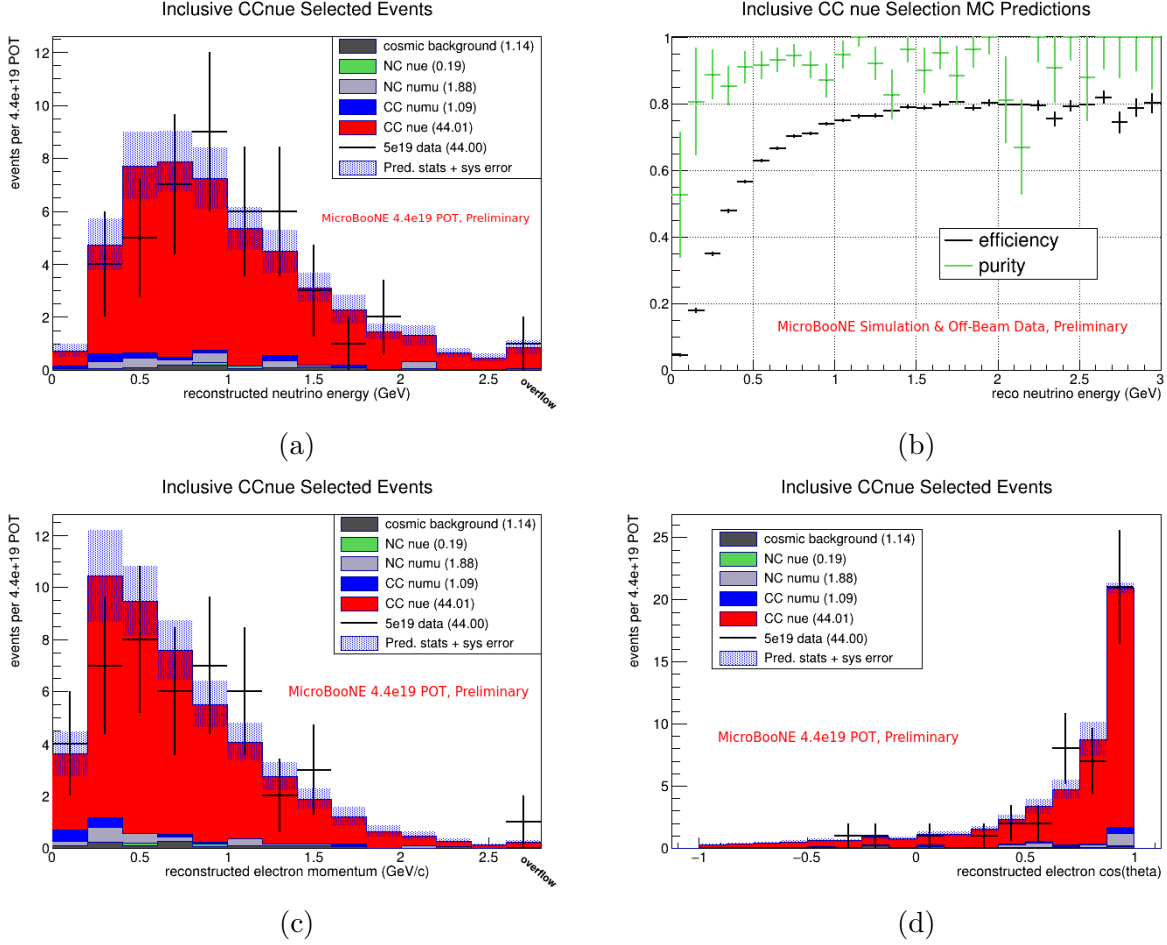


Figure 34: Predicted and MicroBooNE open data distributions of events passing the CC ν_e selection in (a) reconstructed neutrino energy, (c) reconstructed electron momentum, and (d) reconstructed $\cos(\theta_e)$, where θ_e is the angle between the reconstructed electron shower and the beam. (b): The predicted efficiency (from MC) and purity (from MC and off-beam cosmic background data) of the CC ν_e selection as a function of reconstructed neutrino energy.

1290 energies, whereas efficiency drops more dramatically, as expected, at low energies where it
 1291 is more difficult to separate signal from background.

1292 To assess the consistency between the predictions made for these distributions with our
 1293 deep-learning based reconstruction framework and observations from the MicroBooNE open
 1294 data set, we employ a χ^2 goodness-of-fit test using the combined Neyman-Pearson (CNP)
 1295 χ^2 test statistic [36] with the covariance matrix formalism:

$$\chi^2 = (M - \mu)^T \cdot V_{\text{full}}^{-1} \cdot (M - \mu) \quad (6)$$

1296 where M and μ are vectors of the observed and predicted event counts in each bin and V_{full}

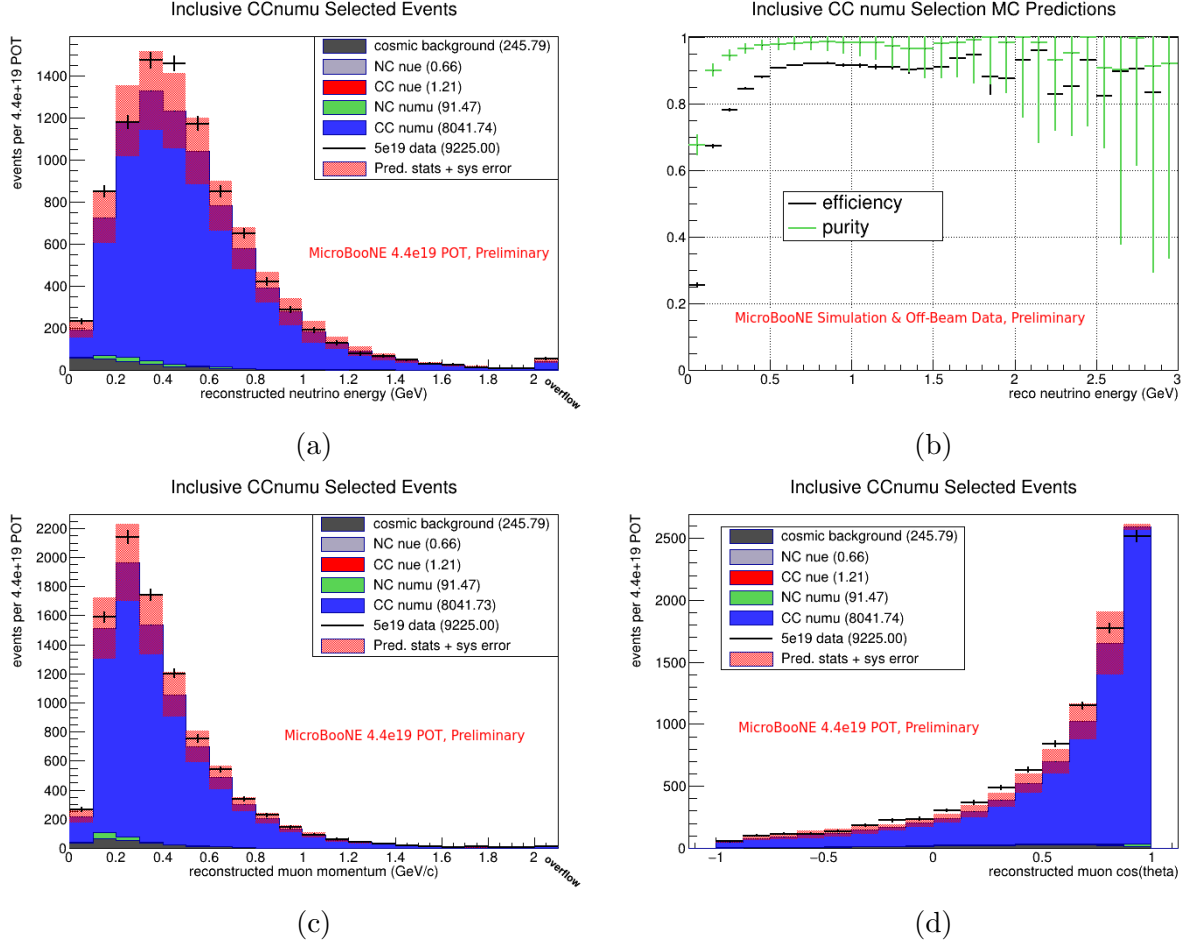


Figure 35: Predicted and MicroBooNE open data distributions of events passing the CC ν_μ selection in (a) reconstructed neutrino energy, (c) reconstructed muon momentum, and (d) reconstructed $\cos(\theta_\mu)$, where θ_μ is the angle between the reconstructed muon track and the beam. (b): The predicted efficiency (from MC) and purity (from MC and off-beam cosmic background data) of the CC ν_μ selection as a function of reconstructed neutrino energy.

1297 is the full covariance matrix in the CNP method:

$$V_{\text{full}} = V_{\text{CNP}}^{\text{stat}} + V_{\text{pred}}^{\text{stat}} + V_{\text{flux}}^{\text{sys}} + V_{\text{xsec}}^{\text{sys}} + V_{\text{det}}^{\text{sys}} \quad (7)$$

1298 This covariance matrix is constructed from the flux and neutrino-argon and hadron-argon
 1299 cross section covariance matrices ($V_{\text{flux}}^{\text{sys}}$ and $V_{\text{xsec}}^{\text{sys}}$) discussed in section III C 2, the detector
 1300 systematics covariance matrix ($V_{\text{det}}^{\text{sys}}$) from section III C 1, a diagonal matrix containing the
 1301 variance in each bin from uncertainties arising from the finite statistics used to make predic-
 1302 tions ($V_{\text{pred}}^{\text{stat}}$), and a diagonal matrix containing the CNP terms: $(V_{\text{CNP}}^{\text{stat}})_{ii} = 3/(1/M_i + 2/\mu_i)$.
 1303 As discussed in section III C 1, we altered the binning used to calculate $V_{\text{det}}^{\text{sys}}$ (and therefore

1304 changed its dimensions) for the reconstructed neutrino energy and muon momentum dis-
 1305 tributions of the CC ν_μ selection by combining high energy/momentum bins. Here, when
 1306 constructing $V_{\text{det}}^{\text{sys}}$ in Eq. 7 for those distributions, we estimate the covariance between in-
 1307 dividual bins in the overflow region and bin i as the covariance between the overflow bin
 1308 and bin i . This maintains the approach of section III C 1 to (temporarily, pending process-
 1309 ing of higher statistics detector variation samples) address low statistics with lower-bound
 1310 estimates that provide a stricter test for data/MC consistency tests.

1311 By comparing the χ^2 from Eq. 6 with the distribution of a χ^2 with N degrees of freedom
 1312 (where N is the number of bins), we can calculate a p-value for our observations (the prob-
 1313 ability of seeing the observed or a more extreme fluctuation) and assess data / Monte Carlo
 1314 consistency. However, the Gaussian assumptions used in the covariance matrix formalism
 1315 followed here break down at low statistics, where much of the Gaussian probability distri-
 1316 butions fall into the un-physical region of negative bin counts. While this is not an issue for
 1317 the CC ν_μ selection where predicted bin counts are sufficiently high across all bins of each
 1318 distribution, in the CC ν_e selection, predicted bin counts are almost all below 10 and fall
 1319 below 1 in the tails. To make the CC ν_e statistics closer to the Gaussian assumption, we
 1320 combine all bins with a predicted event count below 2 for these goodness-of-fit tests. The re-
 1321 binned CC ν_e distributions and the full covariance matrices (equation 7) for all distributions
 1322 in both selections can be found in appendix A.

1323 The χ^2 and associated p-values calculated with this method for the reconstructed neutrino
 1324 energy, lepton momentum, and lepton $\cos(\theta)$ distributions for both selections is shown in
 1325 table VII. All p-values are high: close to or above 90% for most tests and no lower than
 1326 24.4%. This indicates that the open data observations are consistent with our predictions
 1327 and is evidence, for the kinematic variables considered, of a lack of any concerning data /
 1328 Monte Carlo domain shift introduced by our deep-learning based reconstruction algorithms.

| | CC ν_e Selection, E_ν Binning | CC ν_e Selection, p_e - Binning | CC ν_e Selection, $\cos(\theta)$ Binning | CC ν_μ Selection, E_ν Binning | CC ν_μ Selection, p_μ Binning | CC ν_μ Selection, $\cos(\theta)$ Binning |
|---------------------|---|---|--|---|---|--|
| χ^2/DOF | 3.80/9 | 3.06/8 | 5.18/6 | 25.08/21 | 11.91/21 | 9.73/16 |
| p value | 0.924 | 0.931 | 0.521 | 0.244 | 0.942 | 0.880 |

Table VII: Goodness of fit test results: χ^2 / degrees of freedom and associated p values for the reconstructed neutrino energy, lepton momentum, and lepton $\cos(\theta)$ distributions in the inclusive CC ν_e and CC ν_μ selections.

E. Results of Data and MC comparison using Open Data Sample

To further test our predicted inclusive CC ν_e selection results and comparison to PRD 105:112005 [17], we manually hand scanned all MicroBooNE run1 open data events selected by our analysis and that of PRD 105:112005, classifying each as either CC ν_e or background. This open data set contains $4.4 \cdot 10^{19}$ POT of run 1 data.

In the analysis of PRD 105:112005, 40 events were selected, of which (according to our hand scans) 37 or 38 were true CC ν_e interactions. In our analysis, 44 events were selected, of which 42 or 43 were true CC ν_e interactions (there is some uncertainty in the hand scan classifications). These results, along with comparisons to predictions made in the previous section, are summarized in table VIII.

| | DL Reco Data Hand Scan Estimate | DL Reco MC Prediction | PRD 105:112005 Data Hand Scan Estimate | PRD 105:112005 MC Prediction |
|------------------|---------------------------------|-----------------------|--|------------------------------|
| Total Events | 44 | 48.3 | 40 | 41.2 |
| Signal Count | 42 - 43 | 44.0 | 37 - 38 | 33.8 |
| Background Count | 1 - 2 | 4.3 | 2 - 3 | 7.3 |
| Purity | 95% - 98% | 91% | 93% - 95% | 82% |

Table VIII: Hand scan results of inclusive CC ν_e events selected from the open data sample by our deep-learning-based reconstruction and PRD 105:112005 [17].

These results are generally consistent with our expectations, given the large statistical uncertainties with these small numbers of events. With 4 - 6 more probable signal events selected by our framework, these results support our prediction of an increase (compared to PRD 105:112005) in inclusive CC ν_e selection efficiency. Additionally, while the *total* number of selected probable signal events was higher by 4 - 6, there were 11 probable signal events selected by our framework that were not present in the analysis of PRD 105:112005 and 6 probable signal events found in PRD 105:112005 that did not appear in our selection. This indicates that combining the events selected by our framework and PRD 105:112005 (which utilizes the Wire-Cell reconstruction [17–19]) could yield an even more substantial improvement in efficiency, a promising avenue for future work.

The three hand-scan-classified CC ν_e events lowest in reconstructed neutrino energy are shown in figures 36 - 38.

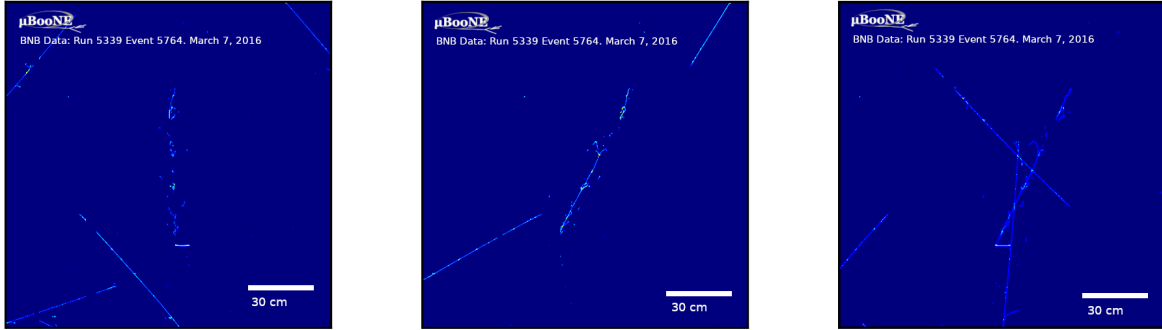


Figure 36: Wire plane images of a probable CC ν_e event selected by our analysis from the MicroBooNE open data set.

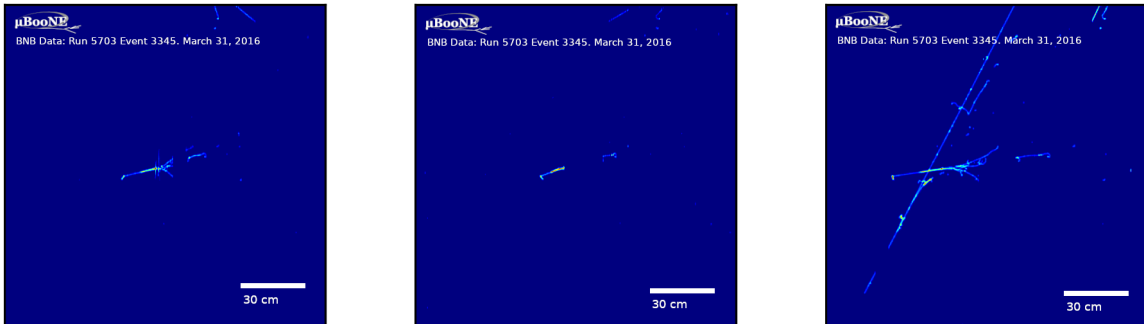


Figure 37: Wire plane images of a probable CC ν_e event selected by our analysis from the MicroBooNE open data set.

1351 IV. DISCUSSION

1352 A new reconstruction workflow has been developed that utilizes three convolutional neural
 1353 networks to perform pattern recognition relatively early in the reconstruction workflow. This
 1354 leverages the powerful ability of CNNs to recognize features in low-level data, specifically,
 1355 the image-like data produced by the LArTPC wire planes. The many outputs and the ability
 1356 to partition the spacepoints into topological classes greatly simplified the reconstruction of
 1357 3D spacepoints. Though this is also in part due to the energy range of interactions for

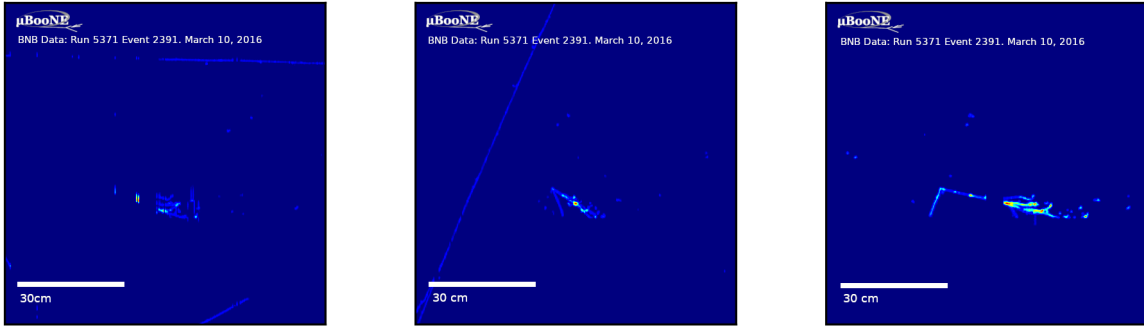


Figure 38: Wire plane images of a probable CC ν_e event selected by our analysis from the MicroBooNE open data set.

1358 MicroBooNE. With median energies below 1 GeV, the final state particles emerging from
 1359 neutrino interactions often do not overlap. Final state particles more often than not emerge
 1360 from the vertex at well-separated angles – which adds to the advantage working in 3D space
 1361 has for clustering. However, we believe the utility of feature recognition by 2D CNNs are on
 1362 display given the modest complexity of the non-DL algorithms implemented in this work.
 1363 Furthermore, the particular use of the LArPID CNN mitigates the impact of mistakes made
 1364 in the 3D reconstruction. This comes from the use of information about both the particle
 1365 under consideration and the entire image of the interaction. We believe one lesson that
 1366 should carry over to analyses being built for future LArTPCs like SBND and DUNE, is that
 1367 access to the 2D image information will have much utility.

1368 The quality of the reconstruction and the utility of the CNN outputs were tested through
 1369 the exercise of selecting inclusive charged-current ν_μ and ν_e interactions. We looked for
 1370 potentially large, show-stopping domain shift effects by testing the selection on the Micro-
 1371 BooNE open dataset. The cuts employed are deceptively simple in that they are flat cuts on
 1372 particle ID scores or on the numbers of certain particles. They are deceptively simple, be-
 1373 cause in other MicroBooNE selections BDTs, using a collection of kinematic observables and
 1374 spatial patterns, was often required to reach the best efficiency and/or purity. However, the
 1375 CNNs used in this work, we conjecture, likely utilizes the same kinematic correlations ex-
 1376 tracted directly from the 2D images and contributes to the improvement in ν_e -CC efficiency
 1377 across a large range of true neutrino energies.

1378 Interestingly, this improvement in the ν_e -CC selection contrasts with the roughly equal
1379 performance between this work and the inclusive ν_μ -CC selection of PRD 105:112005 [17]
1380 utilizing the Wire-Cell reconstruction. In the CC ν_e selection, we leverage the LArPID
1381 scores to further reduce backgrounds by vetoing events with an identified muon or cutting
1382 events with sufficient evidence that the primary shower either derived from charged pions
1383 or is a photon. For the inclusive CC ν_μ event selection, there was not a set of single particles
1384 associated strongly with potential background interactions. Instead, improvement in the
1385 signal acceptance or rejection of background will likely need to come through the use of
1386 correlations between particle kinematics or tuning of cuts in different regions of kinematic
1387 phase space. We leave explorations to improve the selections using the reconstructed particle
1388 kinematics to future work. For now, our conjecture is that the inclusive CC ν_μ selection is
1389 primarily defined by the upstream Wire-Cell cosmic tagging algorithms. The fact that our
1390 efficiency and purity are similar possibly reflects a similar ability to identify the muon within
1391 the in-time charge cluster.

1392 Further conjecture is based in part on the last two cuts applied in the ν_e -CC selection.
1393 These cuts can be interpreted as examples of how CNNs utilize fine image details to great
1394 effect. The last two cuts both target the separation of primary electrons from secondary
1395 electrons coming from the decay of a low-energy muon or charged pion. In these cases, the
1396 information to complete the tasks is located in small regions of the image: the beginning of
1397 showers and around the vertex. The utilization of this information is what we hypothesize
1398 to be the source of the efficiency and purity gains. For example, there can be difficult edges
1399 cases when estimating dE/dx for particle ID. One such case are the potential presence of
1400 additional particles near the vertex. These particles can be of a low enough energy such
1401 that they are missed by the reconstruction, but high enough in energy to impact estimates
1402 like the dE/dx for identified trajectories. Specific scenarios include a short co-linear proton
1403 or a localized region of high energy deposition from a Brem photon emitted early in the
1404 trunk of the shower. Both can push a dE/dx estimate to mis-identify an electron shower
1405 as photon. We conjecture that the LArPID network is able to learn a set of image features
1406 that can detect these edge cases and influence the electron PID. Demonstrating this is one
1407 area for future study. But one piece of circumstantial evidence is the lack of dependence
1408 on the energy scale of the neutrino interaction. In this hypothesis, the occurrence of such
1409 scenarios are broadly distributed across the range of neutrino energies. The possible lack of

1410 comparable scenarios for identifying muons would then explain why improvements are not
1411 observed for the ν_μ selection.

1412 Inspecting the distributions of the LArPID score for the ν_e selection in figure 26, the most
1413 similar distribution to the CCnumu events that remain are the NCnumu events. Cosmic
1414 interactions also peak in a similar region. As discussed above, the electron confidence score
1415 was developed to ID interactions with evidence that the candidate electron shower is actually
1416 a secondary electron from a decay muon or charged pion. For NC events with true neutrino
1417 energies near the peak of 800 MeV, the final state momentum for the charged pions is
1418 likely small. Alternatively, a charged pion with an early decay in flight leads to what
1419 is now easily misinterpretable as an event with a primary muon in the final state. But
1420 in addition to such visual evidence, the LArPID CNN likely has learned to use particle
1421 kinematics better separate CC ν_e events from the various backgrounds. Such kinematic
1422 information is also the kind of information that would be effectively exploited by a BDT-
1423 based selection – as was used in the 2022 inclusive search of PRD 105:112005 [17]. At the
1424 high-level observable distributions studied, we do not find evidence that the CNN-based
1425 reconstruction and selection are more sensitive to argon-interaction modeling uncertainties
1426 when compared to past analyses. But future work will focus on how to dig deeper into this
1427 potential bias.

1428 However, as with all machine learning methods, we must vet the CNNs presumed ability
1429 to correlate latent physical quantities or scenarios to distributions over possible images.
1430 The goal of this work is to report on the completed workflow, and provide evidence of its
1431 competitiveness to past analyses. But more work is ongoing to evaluate the robustness of
1432 this analysis centered on CNNs. The model learning to recognize the features discussed
1433 above derives from training on our simulation data. This data is produced using models
1434 of the MicroBooNE detector and physics like the ionization produced by charged particles.
1435 Though not perfect, one might hypothesize that the level of detector mis-modeling here is
1436 at a manageable level. This is supported by the level of change in the number of selected
1437 events. Even with the higher bound estimates, which we believe are likely due to low MC
1438 statistics, the uncertainties from detector-related effects are similar to the analysis of PRD
1439 105:112005 [17]. Future work can also be done to directly address certain aspects of this
1440 type of domain shift such as adversarial training.

1441 While the gains in the ν_e might come from what has been discussed, the context im-

1442 ages also allow the use of correlations between particle frequency and particle kinematics.
1443 The underlying correlations in the training data, in this case, come from neutrino-argon
1444 interaction modeling, which has uncertainties larger relative to the physics discussed before.
1445 Future work will aim at understanding the degradation of performance of the LArPID net-
1446 work when confronted with images that contain particles with kinematic correlations some
1447 distance outside of the support of the training data. This means that wildly out-of-domain
1448 examples could simply be ignored by the models. Developments in anomaly detection are
1449 one of several directions to research how to improve model robustness or detect issues re-
1450 lated to exotic final states or unusual particle kinematics. There is also the area of domain
1451 adaption which aims to find ways to improve robustness.

1452 CNN models, such as the LArMatch keypoint model, will also be impacted by the use
1453 of training images simulating a LArTPC at the surface. In such a detector, there will be a
1454 high rate of cosmic interactions in each image. For MicroBooNE, this was approximately
1455 10-15 interactions. Generally, our cosmic simulations left more interactions per image than
1456 was seen in the data. Mismodeling cosmic interaction rates are important for several back-
1457 grounds, in particular to interactions with low-energy showers. Such backgrounds include
1458 stopping muons entering near the cathode and leaving a short track and Michel electron,
1459 entering photons, and those produced from hadronic interactions, e.g. from the decay of
1460 neutral pions. As a potential impact, the neutrino vertex finder scores in this context could
1461 be sensitive to the relative rate of neutrino-induced and cosmogenic single-shower events.

1462 Another topic of discussion is what the potential impact this work might have in the
1463 future for both DL and non-DL reconstruction in LArTPCs. For one, the LArPID strategy
1464 of using contextual information around a defined cluster is readily adaptable to existing
1465 MicroBooNE Pandora and Wire-Cell analyses. One might speculate that the differences in
1466 what amounts to the LArPID image pre-processing step for the particle cluster image will
1467 have a limited impact on the LArPID behavior. Future work includes plans to investigate
1468 LArPID integration into these existing workflows.

1469 Many of the hand-engineered algorithms in this work are very simple in their core ap-
1470 proaches, but might require heuristics to tune their behaviors and/or handle edge cases.
1471 This leads to several parameters per algorithm and an overall large number of parameters
1472 affecting the behavior of the reconstruction. Such parameters for each algorithm were tuned
1473 during development on a relatively small MC sample size, $O(100)$ events, in order to iter-

1474 ate and tune these parameters on a day-length time-scale. In contrast, for the DL-based
1475 reconstruction framework in Ref. [11] (referred to as “mlreco3d”), these algorithms have
1476 ML-based counterparts which one might expect to perform better just due to the simple
1477 fact that the algorithms are learned by optimizing them over the entire available training
1478 data. The mlreco3d framework centers around a 3D voxel representation of the LArTPC
1479 data, similar to the use of spacepoints in this work. In particular, the task of forming
1480 subclusters and then collecting them into particle candidates is addressed through the use
1481 of graph neural networks (GNNs). GNNs are likely much more accurate than our shower
1482 reconstruction, which is merely a simple cone-based aggregator. Indeed, the purity versus
1483 completion plots for the electron clusters are the least accurate for our workflow. Similarly,
1484 in mlreco3d associations of particle candidates to potential neutrino interactions are also
1485 done with graphs. Furthermore, mlreco3d’s determination of keypoints and voxel-wise par-
1486 ticle labels make use of the 3D structure in a more direct way than in LArMatch, which
1487 relies only on 2D image features correlated across the wire planes.

1488 In contrast to the 3D spacepoint algorithms, the CNN components in our work would
1489 be the component that would best integrate with a fully ML framework such as mlreco3d.
1490 Indeed, the LArMatch real/ghost classifier was developed to provide a CNN-based pre-
1491 processing step leading into the mlreco3d pipeline. One direction is to investigate if im-
1492 provements could be made by injecting the spacepoint feature vectors into key parts of the
1493 mlreco3d framework. Because the pipeline fully leaves behind the 2D low-level data, one
1494 might believe that LArMatch’s image feature vector can be used to preserve useful details
1495 otherwise lost when moving the representation of the data from 2D images into 3D voxels.
1496 Furthermore, one would also expect that individual particle clustering will not be perfect.
1497 And, therefore, a LArPID-like stage will be useful in similar ways to the reconstruction and
1498 selection described in this work.

1499 V. CONCLUSIONS

1500 This work represents a milestone in the development of ML tools for LArTPC analysis.
1501 We demonstrate – for the first time on real LArTPC data – a deep-learning based generic
1502 neutrino interaction reconstruction framework that is competitive with the current state-
1503 of-the-art: The inclusive CC ν_e and CC ν_μ selections obtained with the outputs of our

1504 reconstruction compare favorably to the highest-efficiency results previously published by
1505 MicroBooNE [17], with reduced backgrounds and a predicted 24% increase in the number
1506 of selected CC ν_e events. Hand scans of selected CC ν_e events from a small MicroBooNE
1507 open data set are consistent with these predictions. These results demonstrate the power
1508 of CNNs to leverage the full set of information provided in LArTPC wire-plane images
1509 at multiple stages of the framework: in low-level reconstruction of vertices and 3D space
1510 points (LArMatch), tagging pixels as track or shower like to aid in downstream clustering
1511 algorithms (SSNet), and analyzing reconstructed 3D prongs with the aid of full wire-plane
1512 images to fold in-context information that may have been lost by inaccuracies in upstream
1513 algorithms (LArPID).

1514 A possible downside of our approach stems from the black-box nature of these deep
1515 networks and their potential to introduce biases from the use of supervised learning on sim-
1516 ulated data. While a more thorough investigation of network-based systematic uncertainties
1517 and model interpretation studies will be the subject of future work, we have demonstrated
1518 that simulated MC distributions of high-level reconstructed kinematic variables for selected
1519 charged-current neutrino interactions are consistent with data. This provides evidence of
1520 the robustness of our framework and a lack of highly significant data/MC domain shifts
1521 introduced by the use of CNNs trained on simulated data.

1522 These results show promise for the deep-learning based reconstruction tools developed
1523 here to improve the sensitivity of LArTPC physics analyses. Future studies will employ this
1524 reconstruction framework in cross-section measurements and new physics searches. In the
1525 near term, individual tools within the framework could be quickly integrated into alternative
1526 reconstruction packages. The LArPID network, for example, could easily be run over 3D
1527 tracks and showers reconstructed by Wire-Cell or other frameworks. As the use of such tools
1528 in high energy physics analyses proliferates, this work contributes towards understanding the
1529 power and robustness of computer vision techniques when applied to LArTPC neutrino data.
1530 It also points towards the improvements these methods can make on the physics that will
1531 come out of future LArTPC experiments, specifically from the short-baseline experiments
1532 over the next few years.

-
- 1533 [1] R Acciarri et al. (MicroBooNE Collaboration). Design and construction of the microboone
1534 detector. *Journal of Instrumentation*, 12(02):P02017, 2017. URL [https://dx.doi.org/10.](https://dx.doi.org/10.1088/1748-0221/12/02/P02017)
1535 [1088/1748-0221/12/02/P02017](https://dx.doi.org/10.1088/1748-0221/12/02/P02017).
- 1536 [2] R Acciarri et al. (ICARUS-WA104, LAr1-ND, and MicroBooNE Collaborations). A proposal
1537 for a three detector short-baseline neutrino oscillation program in the fermilab booster neutrino
1538 beam. *arXiv:1503.01520*, 2015. URL <https://doi.org/10.48550/arXiv.1503.01520>.
- 1539 [3] S Amerio et al. (ICARUS Collaboration). Design, construction and tests of the icarus t600
1540 detector. *Nuclear Instruments and Methods in Physics Research Section A: Accelerators,*
1541 *Spectrometers, Detectors and Associated Equipment*, 527(3):329–410, 2004. URL [https://](https://doi.org/10.1016/j.nima.2004.02.044)
1542 doi.org/10.1016/j.nima.2004.02.044.
- 1543 [4] B Abi et al. (DUNE Collaboration). Volume i. introduction to dune. *Journal of Instrumenta-*
1544 *tion*, 15(08):T08008, 2020. URL <https://dx.doi.org/10.1088/1748-0221/15/08/T08008>.
- 1545 [5] B Abi et al. (DUNE Collaboration). The single-phase protodune technical design report.
1546 *arXiv:1706.07081*, 2017. URL <https://doi.org/10.48550/arXiv.1706.07081>.
- 1547 [6] D A Dwyer, M Garcia-Sciveres, D Gnani, C Grace, S Kohn, M Kramer, A Krieger, C J Lin,
1548 K B Luk, P Madigan, C Marshall, H Steiner, and T Stezelberger. Larpix: Demonstration of
1549 low-power 3d pixelated charge readout for liquid argon time projection chambers. *Journal of*
1550 *Instrumentation*, 13(10):P10007, 2018. URL [https://dx.doi.org/10.1088/1748-0221/13/](https://dx.doi.org/10.1088/1748-0221/13/10/P10007)
1551 [10/P10007](https://dx.doi.org/10.1088/1748-0221/13/10/P10007).
- 1552 [7] R Acciarri et al. (MicroBooNE Collaboration). Convolutional neural networks applied to
1553 neutrino events in a liquid argon time projection chamber. *Journal of instrumentation*, 12
1554 (03):P03011, 2017. URL <https://dx.doi.org/10.1088/1748-0221/12/03/P03011>.
- 1555 [8] B Abi et al. (DUNE Collaboration). Neutrino interaction classification with a convolutional
1556 neural network in the dune far detector. *Physical Review D*, 102(9):092003, 2020. URL
1557 <https://doi.org/10.1103/PhysRevD.102.092003>.
- 1558 [9] Kiara Carloni, Nicholas W Kamp, Austin Schneider, and Janet M Conrad. Convolutional
1559 neural networks for shower energy prediction in liquid argon time projection chambers. *Journal*
1560 *of Instrumentation*, 17(02):P02022, 2022. URL [https://dx.doi.org/10.1088/1748-0221/](https://dx.doi.org/10.1088/1748-0221/17/02/P02022)
1561 [17/02/P02022](https://dx.doi.org/10.1088/1748-0221/17/02/P02022).

- 1562 [10] Pierre Baldi, Jianming Bian, Lars Hertel, and Lingge Li. Improved energy reconstruction in
1563 nova with regression convolutional neural networks. *Physical Review D*, 99(1):012011, 2019.
1564 URL <https://doi.org/10.1103/PhysRevD.99.012011>.
- 1565 [11] François Drielsma, Kazuhiro Terao, Laura Dominé, and Dae Heun Koh. Scalable,
1566 end-to-end, deep-learning-based data reconstruction chain for particle imaging detectors.
1567 *arXiv:2102.01033*, 2021. URL <https://doi.org/10.48550/arXiv.2102.01033>.
- 1568 [12] C Adams et al. (MicroBooNE Collaboration). Deep neural network for pixel-level electromag-
1569 netic particle identification in the microboone liquid argon time projection chamber. *Physical*
1570 *Review D*, 99(9):092001, 2019. URL <https://doi.org/10.1103/PhysRevD.99.092001>.
- 1571 [13] P Abratenko et al. (MicroBooNE Collaboration). Semantic segmentation with a sparse con-
1572 volutional neural network for event reconstruction in microboone. *Physical Review D*, 103(5):
1573 052012, 2021. URL <https://doi.org/10.1103/PhysRevD.103.052012>.
- 1574 [14] P Abratenko et al. (MicroBooNE Collaboration). Search for an anomalous excess of charged-
1575 current quasielastic ν_e interactions with the microboone experiment using deep-learning-based
1576 reconstruction. *Physical Review D*, 105(11):112003, 2022. URL [https://doi.org/10.1103/](https://doi.org/10.1103/PhysRevD.105.112003)
1577 [PhysRevD.105.112003](https://doi.org/10.1103/PhysRevD.105.112003).
- 1578 [15] P Abratenko et al. (MicroBooNE Collaboration). Search for an excess of electron neutrino
1579 interactions in microboone using multiple final-state topologies. *Physical review letters*, 128
1580 (24):241801, 2022. URL <https://doi.org/10.1103/PhysRevLett.128.241801>.
- 1581 [16] A A Aguilar-Arevalo et al. (MiniBooNE Collaboration). Updated miniboone neutrino oscil-
1582 lation results with increased data and new background studies. *Physical Review D*, 103(5):
1583 052002, 2021. URL <https://doi.org/10.1103/PhysRevD.103.052002>.
- 1584 [17] P Abratenko et al. (MicroBooNE Collaboration). Search for an anomalous excess of inclu-
1585 sive charged-current ν_e interactions in the microboone experiment using wire-cell reconstruc-
1586 tion. *Phys. Rev. D*, 105:112005, Jun 2022. URL [https://doi.org/10.1103/PhysRevD.105.](https://doi.org/10.1103/PhysRevD.105.112005)
1587 [112005](https://doi.org/10.1103/PhysRevD.105.112005).
- 1588 [18] P Abratenko et al. (MicroBooNE Collaboration). Wire-cell 3d pattern recognition techniques
1589 for neutrino event reconstruction in large lartpcs: algorithm description and quantitative
1590 evaluation with microboone simulation. *Journal of instrumentation*, 17(01):P01037, 2022.
1591 URL <https://dx.doi.org/10.1088/1748-0221/17/01/P01037>.
- 1592 [19] P Abratenko et al. (MicroBooNE Collaboration). Cosmic ray background rejection with wire-

- 1593 cell lartpc event reconstruction in the microboone detector. *Physical Review Applied*, 15:
1594 064071, 2021. URL <https://doi.org/10.1103/PhysRevApplied.15.064071>.
- 1595 [20] R Acciarri et al. (MicroBooNE Collaboration). Noise characterization and filtering in the
1596 microboone liquid argon tpc. *Journal of Instrumentation*, 12(08):P08003, 2017. URL <https://dx.doi.org/10.1088/1748-0221/12/08/P08003>.
- 1597
- 1598 [21] C Adams et al. (MicroBooNE Collaboration). Ionization electron signal processing in single
1599 phase lartpcs. part i. algorithm description and quantitative evaluation with microboone sim-
1600 ulation. *Journal of Instrumentation*, 13(07):P07006, 2018. URL [https://dx.doi.org/10.](https://dx.doi.org/10.1088/1748-0221/13/07/P07006)
1601 [1088/1748-0221/13/07/P07006](https://dx.doi.org/10.1088/1748-0221/13/07/P07006).
- 1602 [22] C Adams et al. (MicroBooNE Collaboration). Ionization electron signal processing in single
1603 phase lartpcs. part ii. data/simulation comparison and performance in microboone. *Journal*
1604 *of Instrumentation*, 13(07):P07007, 2018. URL [https://dx.doi.org/10.1088/1748-0221/](https://dx.doi.org/10.1088/1748-0221/13/07/P07007)
1605 [13/07/P07007](https://dx.doi.org/10.1088/1748-0221/13/07/P07007).
- 1606 [23] Olaf Ronneberger, Philipp Fischer, and Thomas Brox. U-net: Convolutional networks
1607 for biomedical image segmentation. In *Medical Image Computing and Computer-Assisted*
1608 *Intervention–MICCAI 2015: 18th International Conference, Munich, Germany, October 5-9,*
1609 *2015, Proceedings, Part III 18*, pages 234–241. Springer, 2015. URL [https://link.springer.](https://link.springer.com/chapter/10.1007/978-3-319-24574-4_28)
1610 [com/chapter/10.1007/978-3-319-24574-4_28](https://link.springer.com/chapter/10.1007/978-3-319-24574-4_28).
- 1611 [24] K He, X Zhang, S Ren, and J Sun. Deep residual learning for image recognition.
1612 *arXiv:1512.03385*, 2015. URL <https://doi.org/10.48550/arXiv.1512.03385>.
- 1613 [25] Dmitry Ulyanov, Andrea Vedaldi, and Victor Lempitsky. Instance normalization: The missing
1614 ingredient for fast stylization. *arXiv:1607.08022*, 2016. URL [https://doi.org/10.48550/](https://doi.org/10.48550/arXiv.1607.08022)
1615 [arXiv.1607.08022](https://doi.org/10.48550/arXiv.1607.08022).
- 1616 [26] Benjamin Graham and Laurens Van der Maaten. Submanifold sparse convolutional networks.
1617 *arXiv:1706.01307*, 2017. URL <https://doi.org/10.48550/arXiv.1706.01307>.
- 1618 [27] JunYoung Gwak, Christopher B Choy, and Silvio Savarese. Generative sparse detection net-
1619 works for 3d single-shot object detection. *arXiv:2006.12356*, 2020. URL [https://doi.org/](https://doi.org/10.48550/arXiv.2006.12356)
1620 [10.48550/arXiv.2006.12356](https://doi.org/10.48550/arXiv.2006.12356).
- 1621 [28] Tsung-Yi Lin, Priya Goyal, Ross Girshick, Kaiming He, and Piotr Dollár. Focal loss for
1622 dense object detection. In *Proceedings of the IEEE international conference on computer vi-*
1623 *sion*, pages 2980–2988, 2017. URL <https://doi.ieeecomputersociety.org/10.1109/ICCV>.

- 1624 2017.324.
- 1625 [29] P Abratenko et al. (MicroBooNE Collaboration). Vertex-finding and reconstruction of con-
1626 tained two-track neutrino events in the microboone detector. *Journal of instrumentation*, 16
1627 (02):P02017, 2021. URL <https://dx.doi.org/10.1088/1748-0221/16/02/P02017>.
- 1628 [30] R L Workman et al. Review of Particle Physics. *PTEP*, 2022:083C01, 2022. doi:
1629 10.1093/ptep/ptac097.
- 1630 [31] P Abratenko et al. (MicroBooNE Collaboration). Electromagnetic shower reconstruction and
1631 energy validation with michel electrons and π^0 samples for the deep-learning-based analyses in
1632 microboone. *Journal of Instrumentation*, 16(12):T12017, 2021. URL [https://dx.doi.org/](https://dx.doi.org/10.1088/1748-0221/16/12/T12017)
1633 [10.1088/1748-0221/16/12/T12017](https://dx.doi.org/10.1088/1748-0221/16/12/T12017).
- 1634 [32] F Psihas, E Niner, M Groh, R Murphy, A Aurisano, A Himmel, K Lang, M D Messier,
1635 A Radovic, and A Sousa. Context-enriched identification of particles with a convolutional
1636 network for neutrino events. *Physical Review D*, 100:073005, 2019. URL [https://doi.org/](https://doi.org/10.1103/PhysRevD.100.073005)
1637 [10.1103/PhysRevD.100.073005](https://doi.org/10.1103/PhysRevD.100.073005).
- 1638 [33] A Kendall, Y Gal, and R Cipolla. Multitask learning using uncertainty to weigh losses for
1639 scene geometry and semantics. *arXiv:1705.07115*, 2018. URL [https://doi.org/10.48550/](https://doi.org/10.48550/arXiv.1705.07115)
1640 [arXiv.1705.07115](https://doi.org/10.48550/arXiv.1705.07115).
- 1641 [34] I Loshchilov and F Hutter. Decoupled weight decay regularization. *arXiv:1711.05101*, 2019.
1642 URL <https://doi.org/10.48550/arXiv.1711.05101>.
- 1643 [35] L N Smith and N Topin. Super-convergence: Very fast training of neural networks using
1644 large learning rates. *arXiv:1708.07120*, 2018. URL [https://doi.org/10.48550/arXiv.](https://doi.org/10.48550/arXiv.1708.07120)
1645 [1708.07120](https://doi.org/10.48550/arXiv.1708.07120).
- 1646 [36] Xiangpan Ji, Wenqiang Gu, Xin Qian, Hanyu Wei, and Chao Zhang. Combined ney-
1647 man-pearson chi-square: An improved approximation to the poisson-likelihood chi-square.
1648 *Nuclear Instruments and Methods in Physics Research Section A*, 961:163677, 2020. URL
1649 <https://doi.org/10.1016/j.nima.2020.163677>.

Appendix A: Additional distributions for data vs expectation comparisons

In this appendix, we show the re-binned kinematic variable distributions for the CC ν_e selection (figure 39) and the full covariance matrices (figure 40) used for the χ^2 goodness of fit tests discussed in section III D.

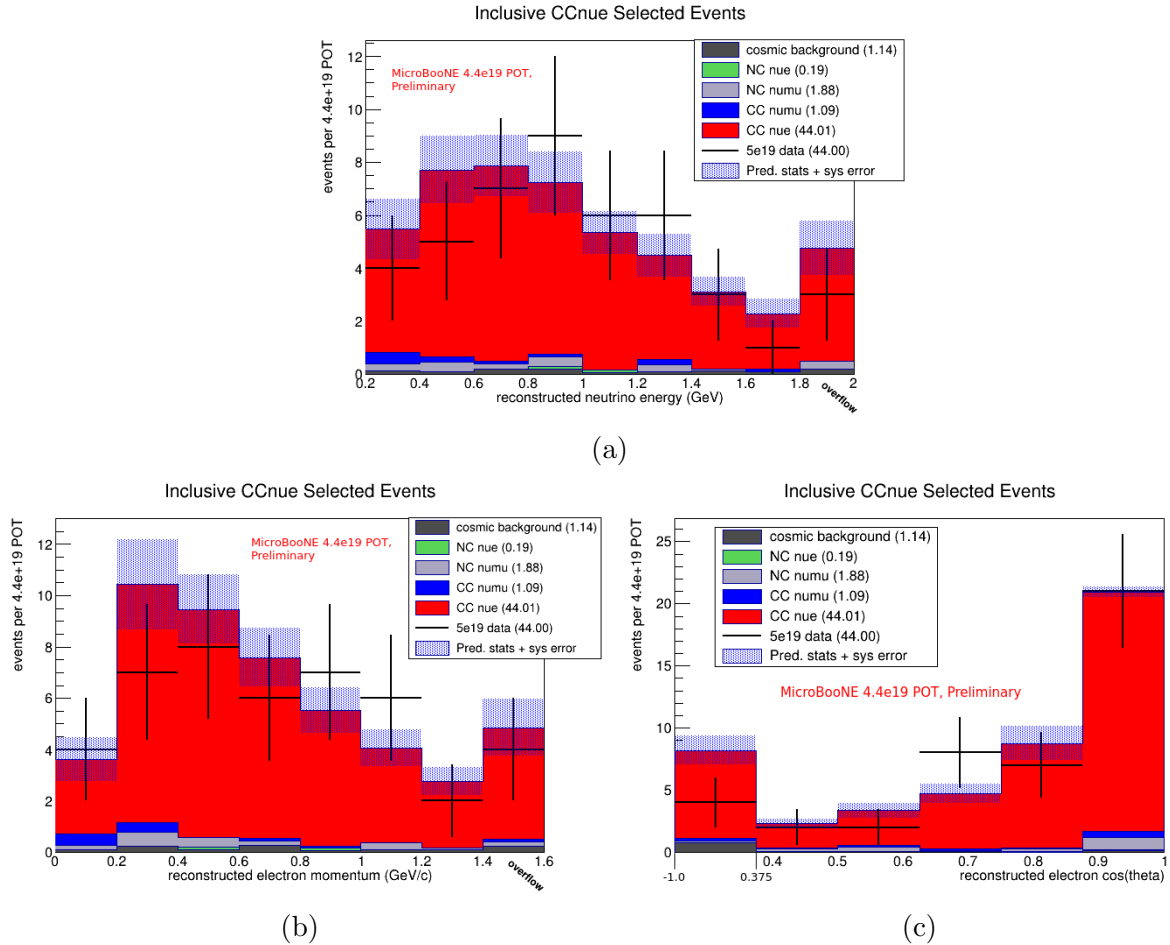
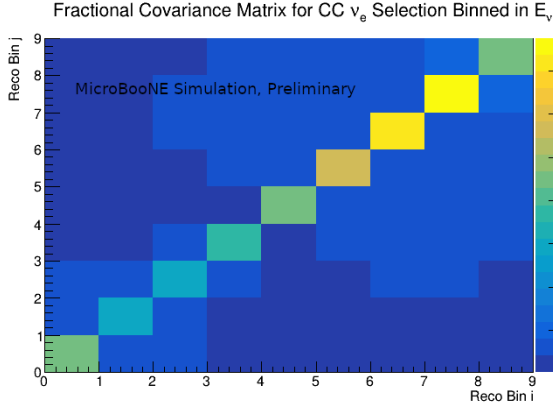
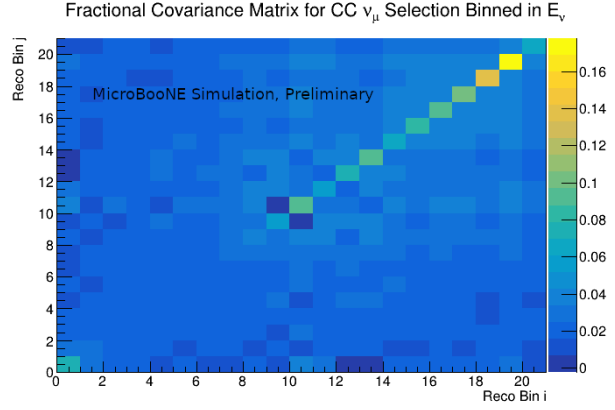


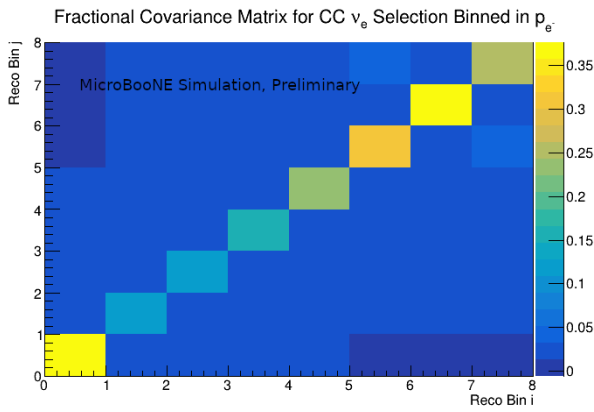
Figure 39: Predicted and MicroBooNE open data distributions, with the binning used in the χ^2 goodness of fit tests of section III D, of events passing the CC ν_e selection binned in (a) reconstructed neutrino energy, (b) reconstructed electron momentum, and (c) reconstructed $\cos(\theta_e)$, where θ_e is the angle between the reconstructed electron shower and the beam.



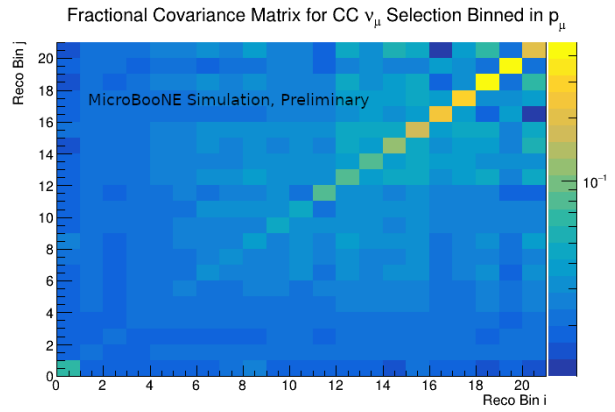
(a)



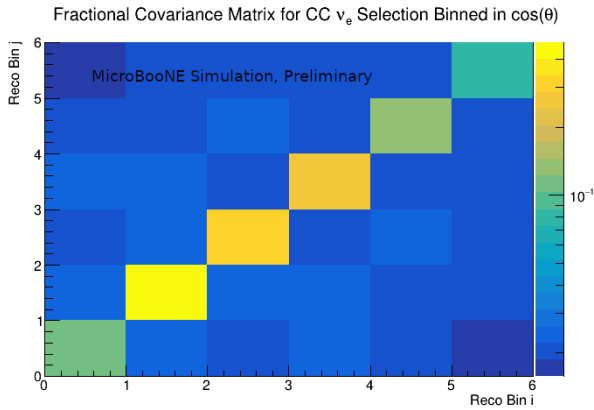
(b)



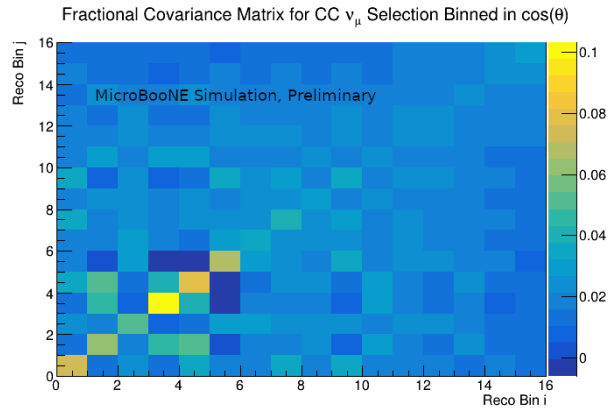
(c)



(d)



(e)



(f)

Figure 40: The full fractional covariance matrices used in the χ^2 goodness of fit tests from section III D.